UNIVERSITY OF CALIFORNIA
Los Angeles

Earth's radiation belts:
From machine learning to physical understanding

A dissertation submitted in partial satisfaction
of the requirements for the degree
Doctor of Philosophy in Atmospheric and Oceanic Sciences

by

Donglai Ma

2023

ABSTRACT OF THE DISSERTATION

Earth's radiation belts:
From machine learning to physical understanding

by

Donglai Ma
Doctor of Philosophy in Atmospheric and Oceanic Sciences
University of California, Los Angeles, 2023
Professor Jacob Bortnik, Chair

This dissertation explores how machine learning can be used to study the Earth's radiation belts and the physical conclusions we derive from machine learning. To be concrete, the Earth's radiation belts contain many high-energy electrons, with their energies ranging from kilo-electron volts (keV) to several Mega-electron volts (MeV). This radiation environment, exhibiting rich dynamical variations, is known to be particularly hazardous to spacecraft and is difficult to predict, particularly because of the delicate balance between acceleration, transport, and loss, combined with the many different physical processes that produce these effects. With high-quality data from the Van Allen Probes mission, we present a set of machine-learning-based models of electron fluxes ranging from 50 keV to several MeV using a neural network approach in the Earth's outer radiation belt. The Outer RadIation belt Electron Neural neT model (ORIENT) uses only a few days of the history of solar wind conditions and geomagnetic indices as input. The models show great performance ($R^2 \sim 0.7 - 0.9$) on the out-of-sample dataset and are able to capture electron dynamics such as intensifications, decays, dropouts, and the Magnetic Local Time dependence of the lower

energy ($\sim<$ 100 keV) electron fluxes during storms. Motivated by the great performance of the machine learning model, we realize that the trained model contain the information of the repeated magnetospheric dynamics driven by solar activity. Thus, we utilize a state-of-the-art feature attribution method called DeepSHAP, which was based on Shapley values in game theory, to explain the behavior of the ORIENT model at a representative electron energy of $\sim$ 1 MeV during a storm time event and a non-storm time event. The results show that the feature importance calculated from the purely data-driven ORIENT model identifies physically meaningful behaviors such as magnetopause shadowing, substorm-driven acceleration, and Dst effect. We then combine this method with superposed epoch analysis to identify the long-debated question: What causes the radiation belt electrons to have two different responses, namely 'enhancement' and 'depletion' to storms? Our feature attribution results indicate that the depletion events can be thought of essentially as "non-acceleration" events that occur when substorm activity following the pressure maximum is not sufficient to accelerate the fluxes above its pre-storm level. The results show that average AL over storm-time period and recovery phase has a significant correlation with the resulting flux levels suggesting that it is important to incorporate the AL index history more directly into the radiation belt modeling. We then turn back to physics and build the statistical model of waves and density related to the AL index to create a Fokker-Planck simulation driven by time-varying geomagnetic activity. The result reproduces the enhancement of electrons at the ultra-relativistic range very well. The observations and simulations of 186 events illustrate a clear threshold on integral AL increasing with energy and demonstrate this is due to the influence of substorm activity on wave intensity and the density of background electrons. We demonstrate that the continuously elevated substorm activity is the determining feature needed for ultra-relativistic electron acceleration.

The dissertation of Donglai Ma is approved.

Hao Cao

Roger Varney

Vassilis Angelopoulos

Jacob Bortnik, Committee Chair

University of California, Los Angeles

2023

To my family ...

and all my friends

TABLE OF CONTENTS

LIST OF FIGURES

LIST OF TABLES

ACKNOWLEDGMENTS

During my four years at UCLA, I have been fortunate to learn from and work alongside the world's best researchers. I am also incredibly lucky to have the support of my family and many friends as I navigated through this period. These few lines cannot fully express my gratitude to all of them but only sketch a few moments.

I would like to thank my advisor, Professor Jacob Bortnik, for every week's great and patient discussion and countless encouraging emails. He not only brought me into space physics but more importantly, showed me how to be a real researcher and a better person. I still remember the comment from him after my first homework: Being good is not enough, you need to be great. I dedicate this work to him because as I reflect on these past years, I realize that I have not only completed a PhD but more importantly, under his influence, I have become a better person in many different ways.

I would like to thank Professor Vassilis Angelopoulos for teaching me plasma physics and data analysis and giving me valuable suggestions during each presentation. I received a lot of support from him and his group in the last four years. His passion and dedication to scientific research have been a great inspiration to me.

I would like to thank my other thesis committee members, Professor Roger Varney, for teaching me space physics related to the ionosphere, and Professor Hao Cao, for giving me valuable tips and guidance on my career path. I would also like to thank Professor Paulo Alves for teaching me plasma physics and for a lot of suggestions and help on our project.

I had a wonderful time working with my colleagues at the Atmospheric and Oceanic Sciences Department at UCLA over the past few years. Dr. Qianli Ma was an amazing collaborator who provided me with a lot of help in both my research and personal life. Dr. Xiangning Chu offered me valuable advice in our research during the initial years, and I will always cherish our discussions and ideas during the pandemic. Collaborating with Dr. Man Hua on various projects was a fortunate experience, and I was honored to witness her

wedding. Dr. Sheng Tian and Dr. Frances Staples shared their ideas and delicious food with me, and I am grateful for that. I received a lot of guidance from Dr. Jinxing Li, Dr. Adam Kellerman, and Dr. Seth Claudepierre on different projects. My fellow graduate students Ning Kang and Nique Stumbaugh helped me prepare for countless group meetings and seminars. Outside of the space physics group, there are a lot of amazing friends in AOS. I would like to thank Dr. Jiaqi Shen, Dr. Yidongfang Si, Dr. Weiming Ma and Dr. Yue Huang for all their support and friendship over these years. I would like to thank Calvin Howes, Xiuyuan Ding, Todd Emmenegger and Olivia Salaben for being great colleagues in the office and friends in my life. All of them are amazing friends and I can't be me today without them.

I really appreciate the big space science group at UCLA. They are great mentors and friends who support me all the way along. I would like to thank Dr. Xin An, who guided me through a lot of my work, taught me how to conduct PIC simulations, and has been a great mentor and friend in my life. I would like to thank Dr. Chen Shi, Dr. Kun Zhang, Dr. Yi Qi, and Xiaofei Shi for serving as best friends in my life. I can't imagine the world at UCLA without them. I would like to thank Dr. Anton Artemyev for all the great physics lessons and all the fruitful discussions. I would like to thank Ethan Tsai for all the help and the amazing tour of the CubeSat lab. We hope our dream will come true.

I am grateful to my roommate and good friend, Jingxi Li, for sticking with me through the pandemic. I would also like to express my appreciation to my friends from high school, Shijie Ge, Bo Li, Zhenhan Zhou, Jinni Jiang and Wanying Zhang, and my undergraduate friends: Yitian Li, Yuqiao Li, Tianshu Pang and Zijie Chen for their daily chats and concern. Due to space limitations, I cannot include everyone. They are sunshine in my life and I also dedicate this work to them.

Finally, I would like to thank my girlfriend Jiaxuan Li for accompanying me for the past few years and for encouraging me to get through those difficult times in life. I would like to thank my grandparents, Deyou Ma and Xuerong Ge, my aunts Hongxia Ma and Xiaoli

Ma, My father Yuan Ma, and my sister Hanyu Bai for their unwavering love and support. I dedicated this work to my family.

Donglai Ma

Feb 10, 2024

Chapter 3 is adapted from "Ma, D., Chu, X., Bortnik, J., Claudepierre, S. G., Tobiska, W. K., Cruz, A., et al. (2022). Modeling the dynamic variability of sub-relativistic outer radiation belt electron fluxes using machine learning. Space Weather, 20, e2022SW003079. https://doi.org/10.1029/2022SW003079".

Chapter 4 is adapted from "Ma, D., Bortnik, J., Chu, X., Claudepierre, S. G., Ma, Q., Kellerman, A. (2023). Opening the black box of the radiation belt machine learning model. Space Weather, 21, e2022SW003339. https://doi.org/10.1029/2022SW003339".

Chapter 5 is adapted from "Ma, D., Bortnik, J., Ma, Q., Hua, M., Chu, X. (2023). Machine learning interpretability of outer radiation belt enhancement and depletion events. Geophysical Research Letters, 50, e2023GL106049. https://doi. org/10.1029/2023GL106049".

Chapter 6 is adapted from "Ma, D., Bortnik, J., Ma, Q., Hua, M., Chu, X. (submitted to Geophysical Research Letters). Simulating the Earth's Outer Radiation Belt Electron Fluxes and Their Upper Limit: A Unified Physics-Based Model Driven by the AL Index".

I gratefully acknowledge Jacob Bortnik as the PI for each work. I gratefully acknowledge Qianli Ma, Xiangning Chu, Seth Claudepierre, and Man Hua for their support in shaping and revising the papers.

I gratefully acknowledge the NASA SWO2R Award 80NSSC19K0239, CCMC award 80NSSC23K0324, and subgrant 1559841 to the University of California, Los Angeles, from the University of Colorado Boulder under NASA Prime Grant agreement 80NSSC20K1580. I gratefully acknowledge the UCLA dissertation year fellowship. I gratefully acknowledge the MagEIS team and Van Allen Probe mission (rbspgway.jhuapl.edu).

VITA

2014–2018 B. S. in Space Physics, University of Science and Technology of China, Hefei, China.

2017–2019 B. S. in Computer Science, University of Science and Technology of China, Hefei, China.

2019–2021 M. S. in Atmospheric and Oceanic Sciences, University of California, Los Angeles, USA.

2019–2023 Graduate Student Researcher, Department of Atmospheric and Oceanic Sciences, University of California, Los Angeles, USA.

2020–2021 Teaching Assistant, Department of Atmospheric and Oceanic Sciences, University of California, Los Angeles, USA.

2023– Ph. D. candidate, Atmospheric and Oceanic Sciences, University of California, Los Angeles, USA.

PUBLICATIONS

1. **Ma, D.**, Bortnik, J., Ma, Q., Hua, M., Chu, X. (submitted to Geophysical Research Letters) Simulating the Earth's Outer Radiation Belt Electron Fluxes and Their Upper Limit: A Unified Physics-Based Model Driven by the AL Index.

2. **Ma, D.**, Bortnik, J., Ma, Q., Hua, M. and Chu, X. (2023). Machine Learning Interpretability of Outer Radiation Belt Enhancement & Depletion Events. Geophysical Research Letters. 10.1029/2023GL106049

3. **Ma, D.**, Bortnik, J., Chu, X., Claudepierre, S. G., Ma, Q. and Kellerman, A. (2023). Opening the Black Box of the Radiation Belt Machine Learning Model. Space Weather, 21(4). https://doi.org/10.1029/2022sw003339

4. **Ma, D.**, Chu, X., Bortnik, J., Claudepierre, G. S., Tobiska, W. K., Cruz, A., Bouwer, S. D., J.F.Fennell and J.B.Blake. (2022). Modeling the dynamic variability of sub-relativistic outer radiation belt electron fluxes using machine learning. Space Weather. https://doi.org/10.1029/2022sw003079

5. **Ma, D.**, An, X., Artemyev, A., Bortnik, J., Angelopoulos, V. and Zhang, X.-J. (2024). Nonlinear Landau resonant interaction between whistler waves and electrons: Excitation of electron acoustic waves. Phys. Plasmas 1 February 2024; 31 (2): 022304. https://doi.org/10.1063/5.0171227

6. **Ma, D.**, An, X., Artemyev, A., Bortnik, J., Angelopoulos, V., Ma, Q, Tian, S and Zhang, X.-J. (in press) Coupling from oblique upper-band whistler waves to electron cyclotron harmonic waves in the Earth's magnetosphere.

7. Chu, X., **Ma, D.**, Bortnik, J., Tobiska, W. K., Cruz, A., Bouwer, S. D., Zhao, H., Ma, Q., Zhang, K., Baker, D. N., Li, X., Spence, H. and Reeves, G. (2021). Relativistic Electron Model in the Outer Radiation Belt Using a Neural Network Approach. Space Weather, 19(12). https://doi.org/10.1029/2021sw002808

CHAPTER 1

Introduction

With the advancement of human technological capabilities, people have started to pay attention to the impact of space physics on human activity and daily life [e.g., *Baker*, 1998]. Space physics is principally concerned with the interaction between charged particles and the electric and magnetic fields in space. In the vicinity of the Earth, the particles can be accelerated to very high energies (multi-MeVs) and form the radiation belts, which is a hazard to satellites and astronauts [e.g., *Thorne et al.*, 2013; *Schwenn*, 2006; *Summers et al.*, 1998; *Horne and Thorne*, 1998]. Although these charged particles derive their energy ultimately from the interaction of the solar wind with the earth's magnetosphere or from the sun, the physical processes in these phenomena are complicated, and the dynamics of those particles are not fully understood [*Li and Hudson*, 2019]. In the last few decades, the rapid development of satellite missions and in situ data have resulted in explosive growth in our understanding of these processes [e.g., *Angelopoulos*, 2009; *Mauk et al.*, 2014]. We briefly review these processes in this chapter and try to depict a basic physical background of what we will discuss in the following chapters.

1.1 The structure of the Earth's magnetosphere and Space Weather

The Earth's magnetosphere is a region in space where the planet's intrinsic magnetic field primarily controls the motion of charged particles. Extending from a few hundred kilometers above the Earth's surface to approximately ten Earth radii ($1R_e \sim 6370$ km) at the subsolar point on the dayside, it acts as a natural barrier protecting Earth from the direct impacts

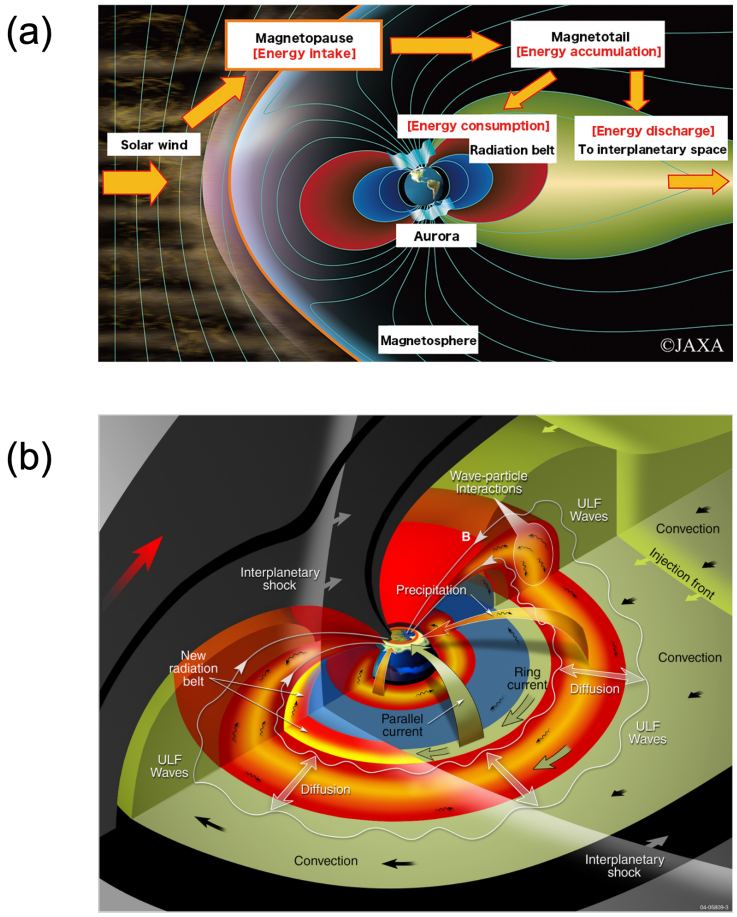

Figure 1.1: Illustration of Earth's magnetosphere. (a) The flow of plasma energy around Earth's magnetosphere. Solar energy absorbed through the magnetopause circulates in the magnetosphere and becomes energy that generates the radiation belt and auroras.[*Kitamura*, 2018] (b) Schematic of 3-D magnetosphere showing regions of convection and diffusion, location of Van Allen Belts, and the arrival of interplanetary shock with new radiation belt produced by rapid inward radial transport along with enhanced ultralow frequency waves [*Mauk et al.*, 2014].

of the solar wind [*Kivelson and Russell*, 1995; *Hargreaves*, 1992].

The solar wind is a continual stream of protons and electrons emanating from the sun's corona (upper atmosphere of the sun) that flows towards the interplanetary region [*Parker*, 1965]. When it reaches the earth, the flow compresses the Earth's magnetic field and stretches it into a long magnetotail on the nightside [*Dungey*, 1961]. A sketch of the Earth's distorted magnetosphere is shown in Figure 1.1. The boundary between the solar wind and Earth's magnetic field is called the magnetopause, typically located at an equatorial geocentric distance ~ 10 Re. The magnetopause is the portion of the magnetospheric surface upon which the solar wind impinges after passing through the bow shock and is constantly in motion as Earth is buffeted by the ever-changing solar wind [*Spreiter et al.*, 1966]. The region between the bow shock and the magnetopause is known as the magnetosheath and is characterized as a region of heated plasma. The solar wind flowing through the polar magnetosphere induces a large-scale electric field directed from dawn to dusk, and particles in the Earth's plasma sheet can be transported to the inner magnetosphere from the tail by such an electric field [*Brice*, 1967].

The inner magnetosphere is composed of three primary particle domains, namely the cold and relatively dense plasmasphere, the more energetic ring current, and the high-energy radiation belts. The plasmasphere is the innermost part of the magnetosphere. It consists of cold ($\sim$ 1eV) and dense ($\gtrsim 10^3$ cm^{-3}) plasma of ionospheric origin [*Chappell et al.*, 1971]. The plasmasphere was discovered by *Gringauz* [1963] using Lunik observation and ground-based whistler wave observation [*Carpenter*, 1963]. The plasmasphere has a clear outer edge, the plasmapause, where the proton density drops by two orders of magnitude. The location of the plasmapause is determined by the interplay between the sunward convection of particles from the plasma sheet and the plasmaspheric plasma corotating with the Earth [*Chappell et al.*, 1971]. This dynamic mechanism leads to the erosion of the plasmasphere and the formation of a plasmaspheric plume near the dusk side [e.g., *Goldstein et al.*, 2004]. The plasmasphere erodes due to a strengthening convection electric field during geomag-

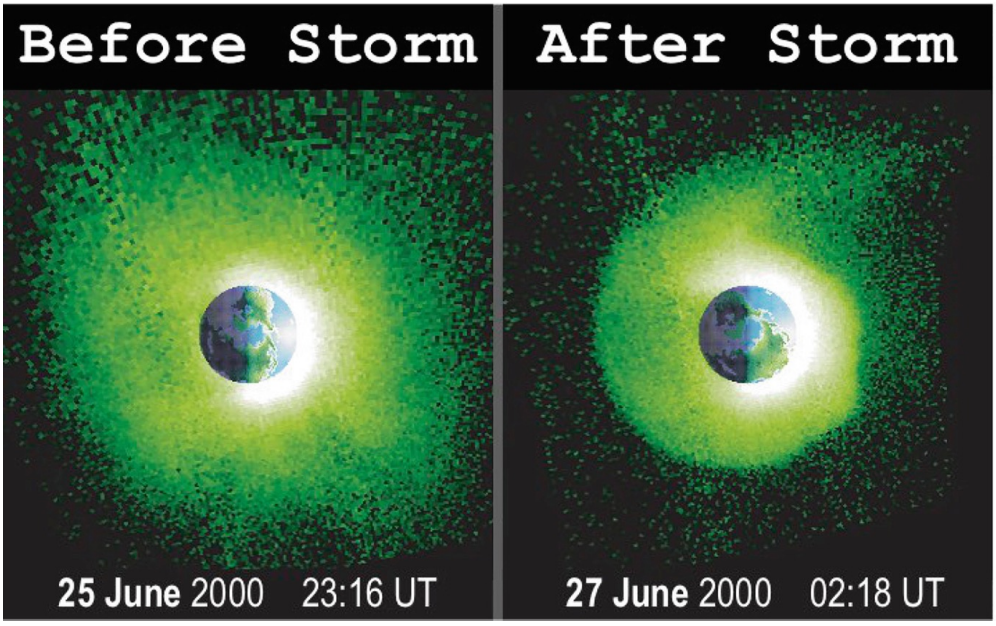

Figure 1.2: Plasmapheric plume and plasmaspheric erosion as observed by the IMAGE EUV instrument. The picture is taken from above the northern hemisphere and the Sun is to the right[*Koskinen et al.*, 2022a].

netic active times. As a consequence, the plasma inside the pre-storm separatrix but outside the separatrix in active times erodes away. Figure 1.2 shows the Imager for Magnetopause-to-Aurora Global Exploration (IMAGE) Extreme UltraViolet (EUV) images [*Burch*, 2000] before and after a moderate geomagnetic storm in June 2000. After the storm, the plasmasphere undergoes significant erosion, leaving a plume that stretches from dusk toward the dayside magnetopause.

The ring current is an electric current flowing toroidally around the earth centered at the equatorial plane. It consists of energetic electrons and ions with energies of 10 to 100s keV trapped by the geomagnetic field. The first measurements of the trapped protons carrying the ring current were limited to energies $>$ 100 keV and over an L range from 3 to 8 by Explorer 12 [*Akasofu et al.*, 1962]. Due to the gradient and curvature of the geomagnetic field lines, electrons drift eastward while ions drift westward, producing a westward current and a southward magnetic field. The magnitude of this component is opposite to the Earth's dipole field at the origin and is proportional to the total energy content of the ring current particles, which is mainly contributed by the 10 keV-100 keV protons [e.g., *Dessler and Parker*, 1959]. During the main phase of a storm, the ring current particles are convected inward by the enhanced electric field and gain energy in this process. The Dst index (or SYM-H index), which is a summation of the perturbation in the horizontal component of the magnetic field of $>$ 10 near-equatorial magnetometers, shows a significant reduction in the storm main phase [*Gonzalez et al.*, 1994]. Figure 1.3a and b show the Dst index and the proton measurements at 54.7 keV from the RBSPICE onboard Van Allen Probes [*Mitchell et al.*, 2014]. It clearly indicates that the minimum of the Dst index is well correlated with the increase of the energy content of low-energy protons.

The Earth's radiation belts were discovered by Geiger counters on Explorer 1 [*Van Allen et al.*, 1958]. They consist of electron and proton populations trapped in the Earth's magnetic field. The electrons in the radiation belts have energies from 100s keV up to 10 MeV [e.g., *Li et al.*, 2001]. Those relativistic electrons ($>$ 500 keV) in the Van Allen radiation belts are

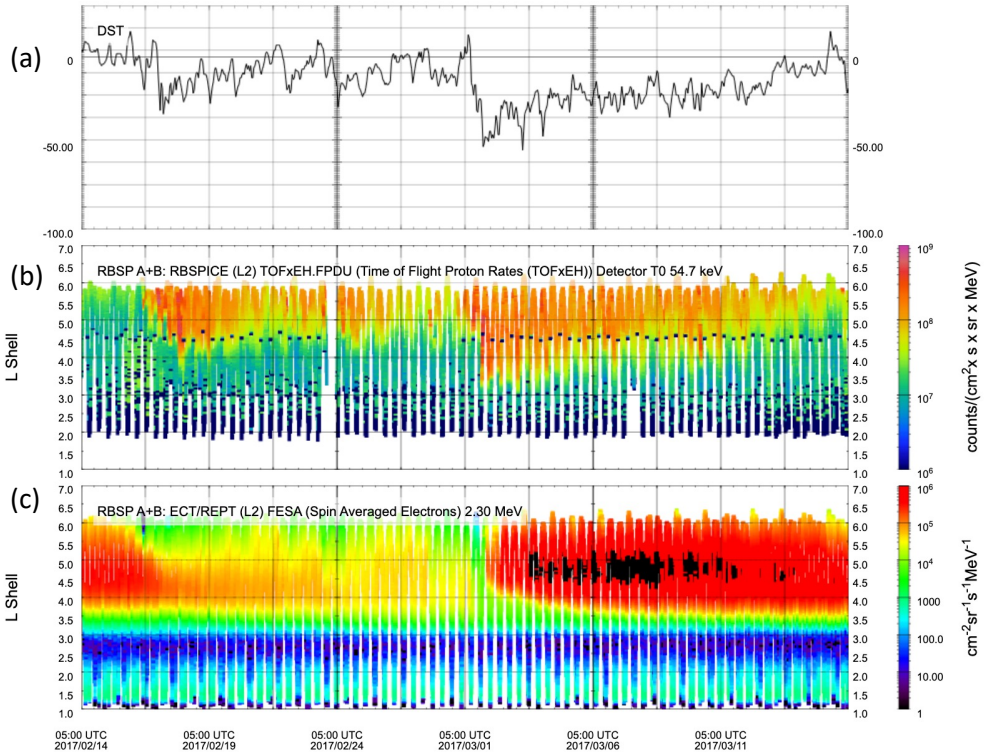

Figure 1.3: Van Allen Probe observations of ring current particles and radiation belt particles from 2017/02/14 to 2017/03/14. (a) DST index. (b) Protons observation at 54 keV. (c) Electrons observation at 2.3 MeV.

called "killer" electrons since their radiation can cause satellite anomalies in space through dielectric charging [e.g., *Baker*, 2001]. They are found in two distinct regions (Figure 1.3c): a stable inner zone ($< 2.5Re$) and a more dynamic outer zone ($> 3Re$) [*Van Allen*, 1997]. The electron slot region between the two belts during quiet times is an equilibrium structure due to inward radial diffusion and pitch angle scattering by plasmaspheric hiss wave [*Lyons and Thorne*, 1973]. The electron flux in the outer radiation belt is constantly subject to dramatic changes, which result from the competition between source and loss processes (see Section 1.4). These processes are primarily due to wave-particle interaction [e.g., *Bortnik et al.*, 2008; *Thorne*, 2010; *Thorne et al.*, 2021] in such collisionless plasma environment, and depend on the geomagnetic conditions since various waves can get enhanced during storms.

Geomagnetic storms are major disturbances of Earth's magnetosphere that occur when there is an efficient exchange of energy from the solar wind into the magnetosphere [*Gonzalez et al.*, 1994]. These storms are the result of variations in the solar wind that produce significant changes in the currents, plasmas, and fields in Earth's magnetosphere. The effective solar wind conditions in triggering geomagnetic storms are sustained periods of high-speed solar wind that last for several to many hours, and most importantly, a southward-directed solar wind magnetic field (opposite to Earth's Bfield) at the dayside of the magnetosphere [e.g., *Gonzalez and Tsurutani*, 1987].

When energy is deposited in the Earth's magnetotail, it can be released through a process called magnetic reconnection [e.g., *Dungey*, 1961; *Øieroset et al.*, 2001]. This causes the magnetic field to snap back towards a dipolar configuration, creating dipolarization fronts (DF) or bursty bulk flows [e.g., *Angelopoulos et al.*, 2013]. The electrons and ions are then injected from the nightside plasma sheet and drift around in the inner magnetosphere as shown in Figure 1.1b. The electrons can be accelerated by different kinds of plasma waves and subsequently trapped by the Earth's magnetic field and form the radiation belts. Some energetic particles can precipitate into the Earth's atmosphere and form aurora. Such transient processes initiated on the nightside of the earth in which a significant amount of

energy derived from the solar wind-magnetosphere interaction is deposited in the auroral ionosphere and in the magnetosphere is called magnetospheric substorm [*Rostoker et al.*, 1980] and can be measured by auroral electrojet indices.

Just like the weather we experience daily on Earth, these various changes in the space environment can also be referred to as "space weather" [*Baker*, 1998]. The term space weather refers to conditions on the sun and in the solar wind, magnetosphere, ionosphere, and thermosphere that can influence the performance and reliability of space-borne and ground-based technological systems and that can affect human life and health [*Schwenn*, 2006]. For instance, the radiation belts within the magnetosphere can interfere with satellite operations [e.g., *Choi et al.*, 2011], while particles and currents from the magnetosphere can heat up the upper atmosphere, resulting in satellite drag that affects the orbits of low-altitude Earth orbiting satellites [e.g., *Cook*, 1965]. The recent most widely known incident is the event on 4 February 2022, where 38 Starlink satellites were destroyed by the geomagnetic storm [e.g., *Dang et al.*, 2022]. Furthermore, the magnetosphere's impact on the ionosphere can also affect communication and navigation systems [e.g., *Klobuchar*, 1987]. Thus, it is very important for us to understand the different mechanisms that affect space weather [*Baker and Lanzerotti*, 2016].

1.2 Particle motion in the radiation belts

The equation of motion for a charged particle is well-known as

$$\frac{d\mathbf{p}}{dt} = q(\mathbf{E} + \mathbf{v} \times \mathbf{B}), \tag{1.1}$$

where $\mathbf{p} = \gamma m_0 \mathbf{v}$ is the particle momentum, q is the particle charge, $\mathbf{E}$ is the electric field and $\mathbf{B_0}$ is the magnetic field. This motion can be difficult to conceptualize in a complex electric field and magnetic field configuration, and the result has to be obtained by numerical integration [e.g., *Tao et al.*, 2012]. However, the solution can be approximated by guiding center approach and subsequent development of adiabatic invariant concepts [*Alfven*, 1950].

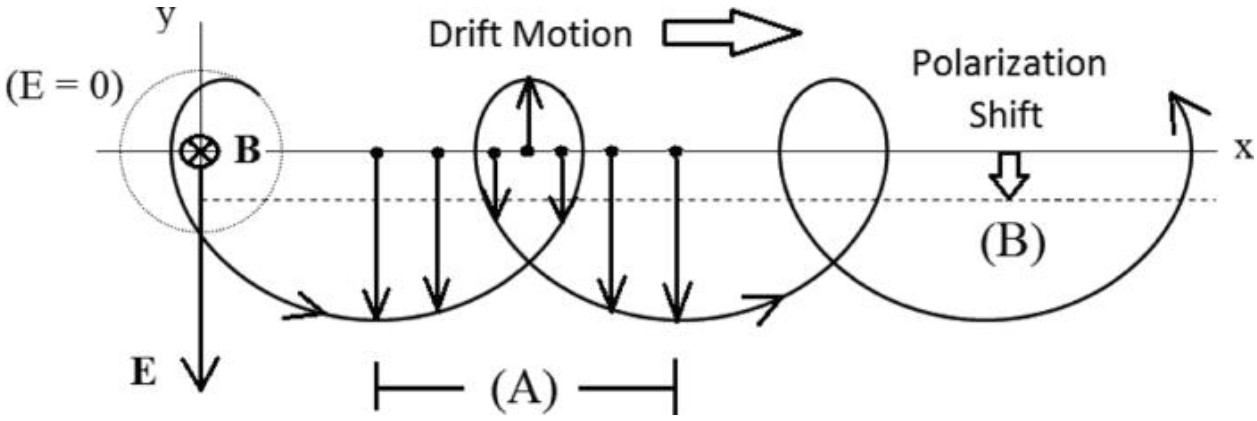

Figure 1.4: Particle motion in an electromagnetic field. [*Brizard*, 2013]

1.2.1 Guiding center and drift

Let's imagine a particle in the constant background magnetic field **B**. The velocity **v** can be decomposed as $v_{\parallel}$ and $v_{\perp}$. The former leads to a constant velocity motion following the magnetic field line and the latter is the gyration motion. The gyroradius or Larmor radius can be expressed as $R_L = \frac{mv_{\perp}}{qB}$, and the gyrofrequency or cyclotron frequency can be expressed as $\Omega = \frac{qB}{m}$. Now assume another uniform electric field **E** that is introduced orthogonal to **B**. Take z along the **B** direction and y along the **E** direction (Figure 1.4), then the particle motion can be expressed as

$$\begin{cases} \ddot{y} = \frac{q}{m}\left(E - \dot{x}B\right) = \frac{q}{m}E - \Omega\dot{x}, \\ \ddot{x} = \frac{q}{m}\dot{y}B = \Omega\dot{y}. \end{cases} \tag{1.2}$$

An easy way to solve Equation 1.2 is to use $\zeta \equiv x + \mathrm{i}y$. It can then be expressed as:

$$\frac{\ddot{\zeta}}{\dot{\zeta} - \frac{E}{B}} = -\mathrm{i}\Omega, \tag{1.3}$$

Integrated t, we get:

$$\dot{\zeta}(t) = \left[\dot{\zeta}(0) - \frac{E}{B}\right]\mathrm{e}^{-\mathrm{i}\Omega t} + \frac{E}{B}. \tag{1.4}$$

Let $\frac{E}{B} \equiv u_E$, $\quad \dot{\zeta}(0) - u_E \equiv v_0\mathrm{e}^{-\mathrm{i}\varphi}$, then we get:

$$\dot{\zeta}(t) = v_0 \mathrm{e}^{-\mathrm{i}(\Omega t+\varphi)} + u_E. \tag{1.5}$$

The first term of the right hand side describes the Larmor gyration of the particle. The center of the gyration circle is the guiding center. It is easy to notice that the average movement of this guiding center is the last term u_E moving along the x direction (see Figure 1.4), which is called the drift and can be written in vector notation as

$$\boldsymbol{u}_E = \frac{\boldsymbol{E} \times \boldsymbol{B}}{B^2}, \tag{1.6}$$

and it is worth noting that one can change the electric field to other forces, for example, gravity fields, obtaining

$$\boldsymbol{u}_E = \frac{m\boldsymbol{g} \times \boldsymbol{B}}{B^2}. \tag{1.7}$$

1.2.2 Adiabatic Invariance

In the guiding center approximation, the motion of a particle can be decomposed into three components: gyration around the field line, bouncing back and forth along a field line between mirror points, and a slow longitudinal drift around the earth as shown in Figure 1.5 [*Roederer and Zhang*, 2016]. These quasi-periodic motions (associated with μ, J, ϕ below) are adiabatic invariants [*Landau and Lifshitz*, 2013] which in the framework of Hamiltonian mechanics: if q and p are the canonical coordinate and momentum of the system, and the system is nearly periodic and parameterized by a slowly varying variable λ (not changing much in a period T), then the integral $I = \oint p \, \mathrm{d}q$ is approximately conserved. Such I is the adiabatic invariant.

The first adiabatic invariant describes the gyro motion. Assume the particles are moving in the magnetic field with a slow variation: $|\dot{\boldsymbol{B}}|/|\boldsymbol{B}| \ll |\Omega|$. The perpendicular energy changed as follows:

$$\Delta W_\perp = \Delta\left(\frac{1}{2}mv_\perp^2\right) = q\oint \boldsymbol{E}\cdot \mathrm{d}\boldsymbol{r}_\perp = -q\iint(\boldsymbol{\nabla}\times\boldsymbol{E})\cdot\mathrm{d}\boldsymbol{S} = q\iint\frac{\partial \boldsymbol{B}}{\partial t}\cdot\mathrm{d}\boldsymbol{S} = qS\dot{B}. \quad (1.8)$$

Because the variation is small in one period, the S does not change:

$$S = \pi R_\mathrm{L}^2 = \pi\left(\frac{mv_\perp}{qB}\right)^2$$

and the

$$\dot{B} = \frac{\Delta B}{T_\mathrm{L}} = \frac{qB}{2\pi m}\Delta B,$$

Put into Equation 1.8, we can get

$$\Delta W_\perp = \frac{mv_\perp^2\Delta B}{2B} = W_\perp\frac{\Delta B}{B}, \quad (1.9)$$

which tells us the magnetic moment $\mu = \frac{W_\perp}{B}$ is an adiabatic invariant.

The second adiabatic invariant describes the bounce motion. Since the magnetic field magnitude increases with latitude, the kinetic energy in the perpendicular motion $W_\perp$ must increase and because the kinetic energy of the particle is conserved in the magnetic field, the $W_\parallel$ can reach zero and the particle would bounce back. Such a configuration of the magnetic field is called a magnetic bottle or magnetic mirror. If the parallel velocity is large enough, the particle can escape from the mirror within a cone defined by

$$\frac{\sin^2\theta_0}{B_\mathrm{min}} = \frac{\sin^2 90^\circ}{B_\mathrm{max}}, \quad \theta_0 = \arcsin\sqrt{\frac{B_\mathrm{min}}{B_\mathrm{max}}}. \quad (1.10)$$

The trapped particles can then bounce in the mirror and possess the second adiabatic invariant

$$J = 2\int_{s_1}^{s_2} v_\parallel \mathrm{d}s \quad (1.11)$$

where the integral is performed between the two reflection points.

The particles can also perform drift motion perpendicular to the magnetic field. We already discussed the $E\times B$ drift (Equation 1.7), and the non-uniform background magnetic

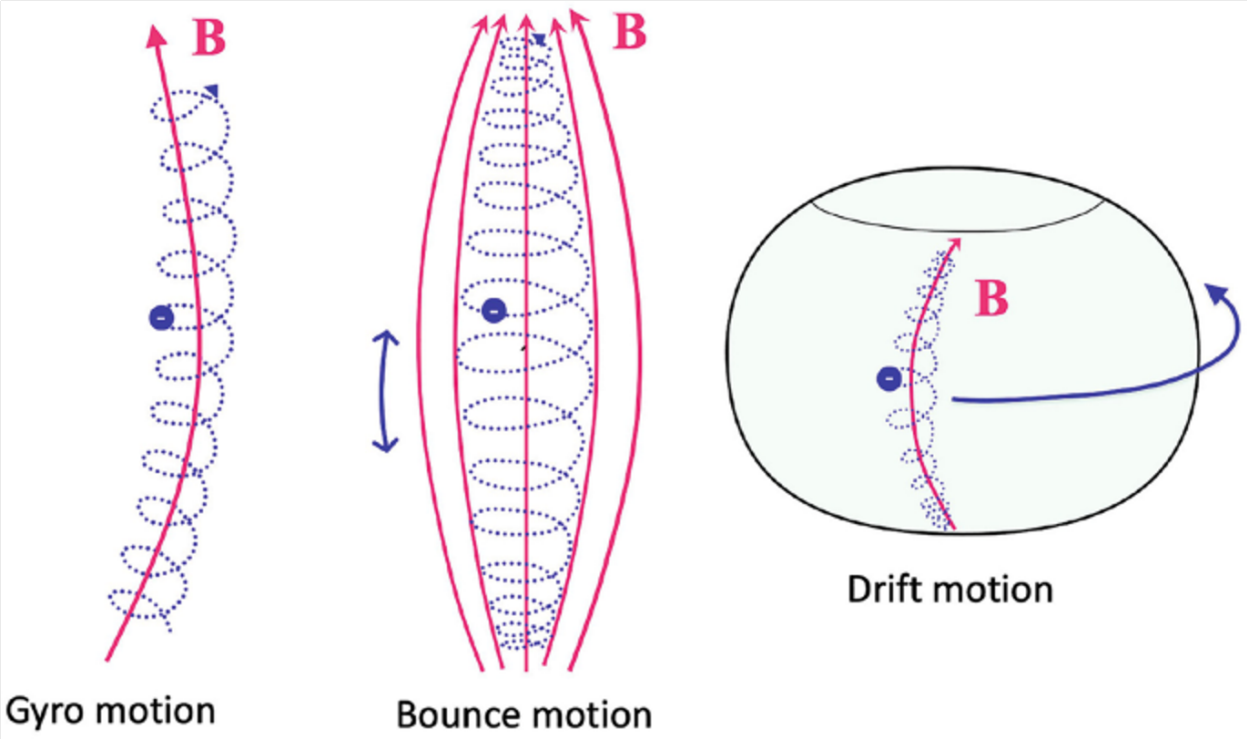

Figure 1.5: The motion of a charged particle trapped in the earth's magnetic field [*Koskinen et al.*, 2022b]

field would also cause drift motion. We briefly show the two equations below. The magnetic gradient drift velocity is

$$\boldsymbol{u}_{gradB} = \frac{mv_{\perp}^2}{2qB^3}(\boldsymbol{B} \times \nabla)B \tag{1.12}$$

and the curvature drift velocity is:

$$\boldsymbol{u}_{curvB} = \frac{mv_{\parallel}^2}{qB^2}\boldsymbol{K} \times \boldsymbol{B}, \tag{1.13}$$

where $\boldsymbol{K}$ is the curvature vector of the magnetic field: $\boldsymbol{K} = -(\boldsymbol{b}\cdot\nabla)\boldsymbol{b}$ and $\boldsymbol{b} = \frac{\boldsymbol{B}}{B}$. It is worth noting that the curvature and gradient drift velocity depend on the charge of the particles, which means such drift can contribute to the electric current in the plasma. In the Earth's magnetosphere, the electrons drift eastward, and the ions with high energy drift westward. Thus, the drift motion corresponds to another quasi-periodic motion and can be described as

$$\Phi = \int \mathbf{B} \cdot d\mathbf{S} \tag{1.14}$$

The time scales of the different invariants differ significantly. In the radiation belts, the time scale of the perodic motion associated with μ_m, J and Φ are 10^{-4} s, 10^{-1} s and hours. When there are comparable time scales of dynamics, such as plasma waves, they may cause violations of the three adiabatic invariants, making the dynamic of particles more complex.

1.3 Plasma waves in magnetosphere and wave-particle interaction

A plasma is a gas in which particles show collective behavior [*Chen*, 2012]. A wide variety of wave phenomena can occur in plasmas [*Stix*, 1992]. The Earth's magnetosphere creates a magnetized environment with no collisions, where the variability in the energetic particle populations is primarily governed by interactions with magnetospheric waves [*Thorne et al.*, 2021]. It is crucial to understand the presence of plasma waves and their properties to comprehend the non-adiabatic dynamics of particles, simulate the evolution of particle populations, and predict changes in space weather due to solar activity. This section gives a very

brief introduction to some waves especially whistler-mode chorus waves and wave-particle interactions in the Earth's magnetosphere.

1.3.1 Whistler-mode chorus waves

Whistler-mode waves are one of the most important types of waves in the magnetosphere [e.g., *Horne et al.*, 2005]. The dispersion of such waves resulted in higher group velocity for high-frequency waves so that the high-frequency component would arrive first, which makes them sound like a whistle [*Helliwell*, 2014]. There are two important types of whistler-mode waves: chorus and hiss. Figure 1.6 shows the chorus waves are outside the plasmasphere, and hiss waves inside the plasmasphere, named plasmaspheric hiss. The names of hiss and chorus come from the appearance of their frequency-time relation. Figure 1.7 shows a typical example of hiss and whistler mode chorus waves observed on the THEMIS mission [*Angelopoulos*, 2009].

Chorus waves are coherent electromagnetic emissions that are the major source of the local heating of energetic electrons [e.g., *Thorne et al.*, 2013]. When the plasma sheet electrons are injected from the tail, the anisotropy of particle distribution provides the free energy source for the wave excitation [e.g., *Kennel and Petschek*, 1966]. Chorus waves typically occur in the frequency range from 0.1 to 0.8 f_{ce} over a broad spatial region from the night side to the dawn side and then the day side. The amplitude of the chorus wave is found to be correlated to geomagnetic activity [e.g., *Li et al.*, 2011; *Malaspina et al.*, 2016]. Another interesting property is that the chorus waves are commonly observed as the two-band structure separated by $0.5f_{ce}$ (see Figure 1.7 b). Such behavior can be explained as the Landau resonance modifying the electron distribution at medium energy which leads to separating energy range for whistler wave excitation [*Burtis and Helliwell*, 1969; *Li et al.*, 2019].

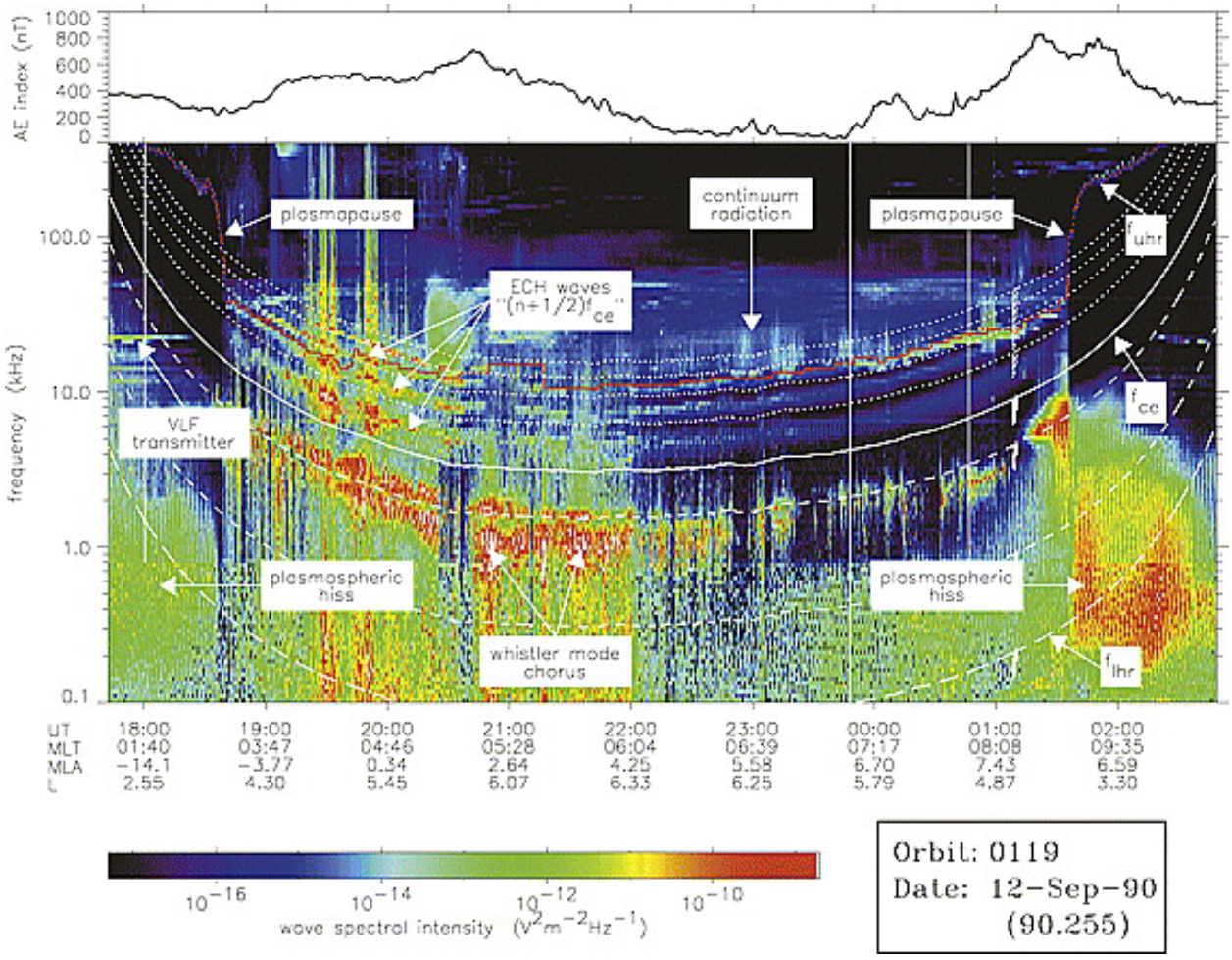

Figure 1.6: Survey plot of the wave spectral intensity observed on CRRES during orbit 119 together with a trace of the AE index (top). Plasmaspheric hiss is the unstructured emission observed below a few kHz, which is primarily confined to the plasmasphere. The solid white line represents the local electron gyrofrequency f_{ce}. Dashed lines from bottom to top represent the local lower hybrid resonance frequency f_{LHR}, $0.1f_{ce}$, and $0.5\mathrm{f}f_{ce}$. The first four harmonics of f_{ce} are represented by the dotted lines and the local upper hybrid resonance frequency f_{UHR} is shown in red [*Meredith et al.*, 2004].

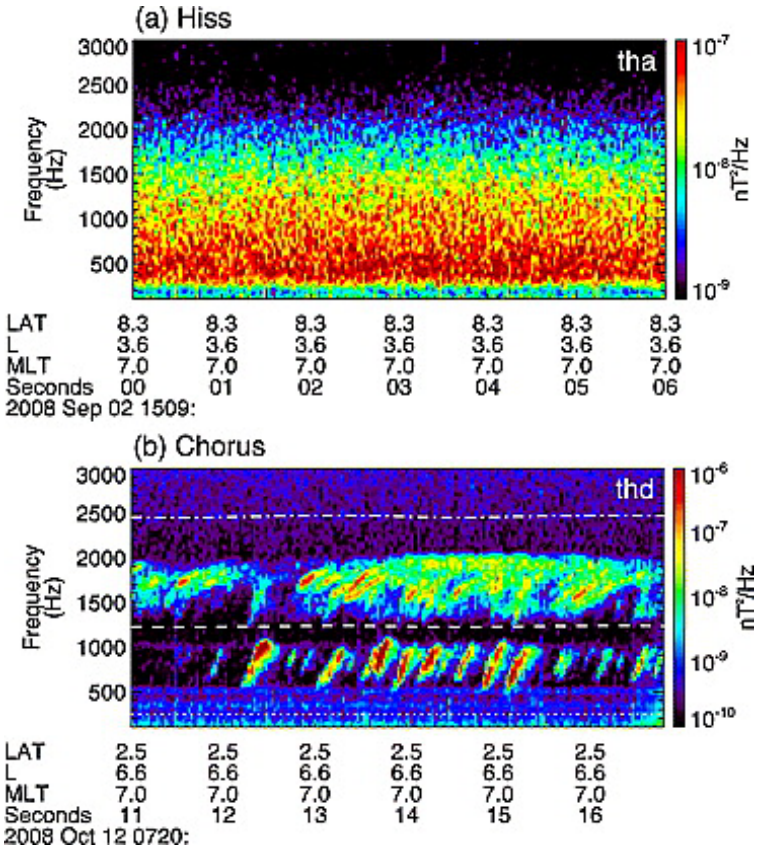

Figure 1.7: A typical example of (a) plasmaspheric hiss and (b) whistler mode chorus waves observed on the THEMIS spacecraft, inside and outside the plasmasphere, respectively. Both examples are shown on the same time scale (6 s total) and frequency range (0.1–3 kHz) at MLT = 7. The three white lines in Figure 1b represent 1 (dash-dotted), 0.5 (dashed), and 0.1 (dotted) f_{ce}. The individual chorus elements are a factor of 10 more intense than the hiss. Figure reproduced from *Bortnik et al.* [2011]

1.3.2 Wave particle interactions

Consider a plane wave where the components of the wave field vary as $e^{i(\boldsymbol{kx}-\omega t)}$. If we observe this wave from the guiding-center frame of a particle with parallel velocity $v_\parallel$ (see Section 1.2.1), the frequency will be Doppler shifted to $\omega - k_\parallel v_\parallel$. In general, the wave effect on the particle will be different in each cycle and will average to zero over many gyroperiods. However, if the frequency of rotation of the particle or one of the harmonics matches the doppler shifted frequency of the wave, then the particle will see a field with an approximately constant wave phase and result in strong resonance effects. Such resonance conditions can be written as:

$$\omega - k_\parallel v_\parallel = n\Omega_e \tag{1.15}$$

where $k_\parallel$ is the wave vector parallel to the ambient magnetic field, and n is the resonant harmonic number. When $n = 0$, it is called Landau resonance, and others are called cyclotron resonance. The left part of Figure 1.8 illustrates a wave-particle interaction in the radiation belt at $L = 5$. The waves are generated near the equatorial plane and propagate roughly along the field line. The equation of the particle motion can be modified from Equation 1.1 to:

$$\frac{d\boldsymbol{p}}{dt} = q\left(\boldsymbol{E}_\mathrm{w} + \frac{\boldsymbol{p}}{m_e\gamma} \times [\boldsymbol{B}_0(\lambda) + \boldsymbol{B}_\mathrm{w}]\right) \tag{1.16}$$

The wave phase and the gyrophase info are illustrated at the left bottom of Figure 1.8 and for parallel propagating wave, the evolution of the particle motion can be further written as:

$$\begin{aligned}
\frac{dv_\parallel}{dt} &= \left(\frac{qB_w}{m}\right) v_\perp \sin\eta - \frac{v_\perp^2}{2B}\frac{\partial B}{\partial z} \\
\frac{dv_\perp}{dt} &= -\left(\frac{qB_w}{m}\right)\left(v_\parallel + \frac{\omega}{k}\right) v_\perp \sin\eta + \frac{v_\perp v_\parallel}{2B}\frac{\partial B}{\partial z} \\
\frac{d\eta}{dt} &= \Omega - \omega - kv_\parallel
\end{aligned} \tag{1.17}$$

and it is clear to see that when there is resonance, the particle dynamics will be greatly changed. The right part of Figure 1.8 shows the test particle dynamics under different wave conditions. When wave amplitude is small, the particle energy will slightly change,

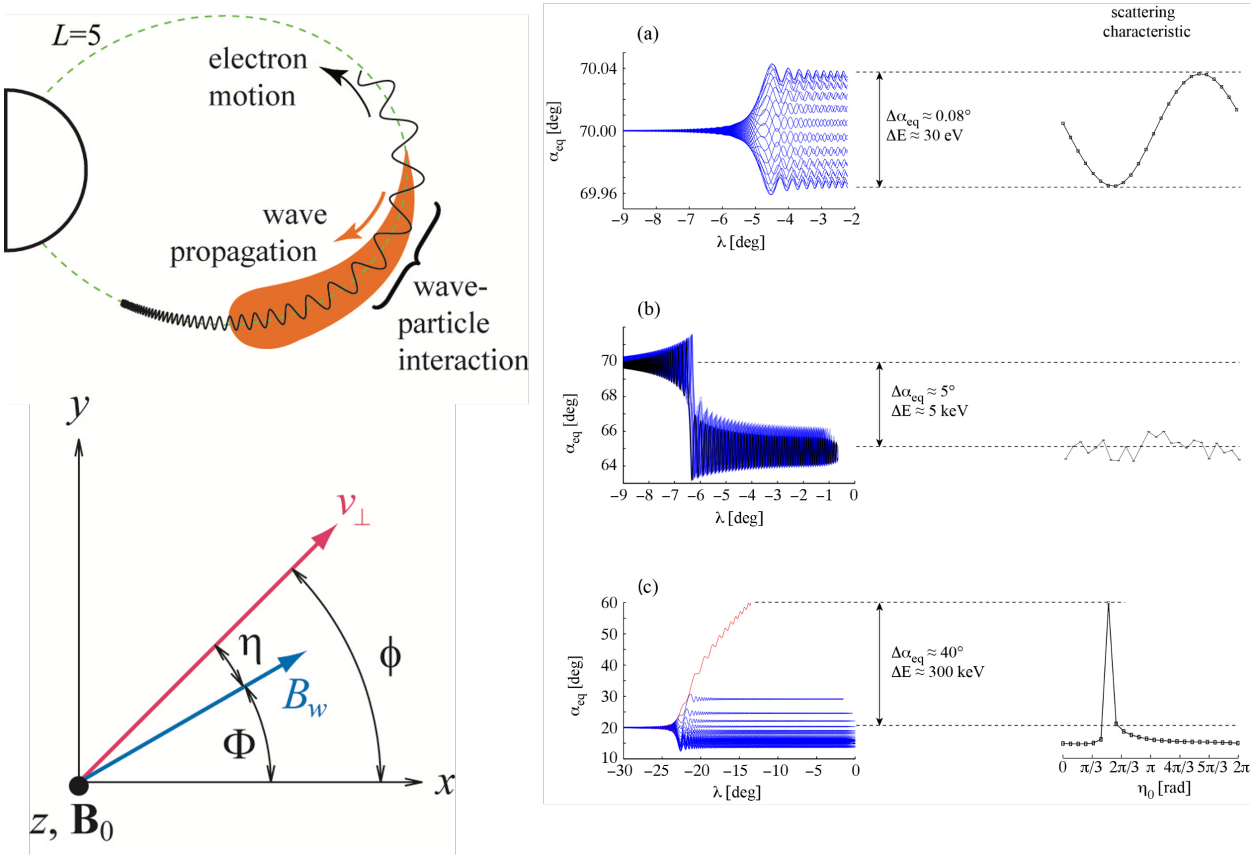

Figure 1.8: An illustration of a single wave-particle interaction in the radiation belt and the test particle interaction examples. Case A, small-amplitude waves at low latitude; Case B, large-amplitude waves at low latitude; Case C, large-amplitude, oblique waves in low-density plasma, at high latitudes [*Bortnik et al.*, 2008]

.

corresponding to a diffusive process, and when wave amplitude is large enough, the particle energy will significantly change through nonlinear phase bunching and phase trapping [e.g., *Albert*, 1993; *Bortnik et al.*, 2008]. Thus, the properties of waves are critical for quantifying the large-scale dynamics of the radiation belts.

1.4 Acceleration, loss, and transport of radiation belt electrons

The Earth's radiation belts consist of energetic charged particles trapped by the geomagnetic field and are seperated into two regions, a relatively stable inner zone, and a more dynamic outer zone [*Van Allen*, 1997]. Significant advances have been made in understanding and modeling the physical processes that control Earth's radiation belt electron dynamics over the Van Allen Probe observations [e.g., *Li and Hudson*, 2019]. Figure 1.9 shows an illustration that summarizes the acceleration and loss process of outer radiation belt electrons. Seed electron populations ($\sim$ 100s keV) can be accelerated to MeV energies through local acceleration, and they are provided by electron injections caused by substorms or enhanced convection, inward radial diffusion, and time domain structures [*Malaspina et al.*, 2018]. The transport of seed electron population from the tail may be highly structured azimuthally in bursty bulk flows, as demonstrated in MHD-test particle simulations [e.g., *Merkin et al.*, 2019].

The most effective local heating process in the core of the outer radiation belt is due to whistler mode chorus waves, which facilitate electron phase space density peaks through either diffusive or nondiffusive scattering mechanisms [e.g., *Summers et al.*, 1998; *Thorne et al.*, 2013; *Horne and Thorne*, 1998]. This process is always followed by a radial diffusion process [e.g., *Ozeke et al.*, 2019; *Ma et al.*, 2015], primarily driven by ULF waves, which redistributes electrons in L-shell and results in further acceleration or deceleration based on whether the transport is radially inward or outward.

When the solar wind dynamic pressure increases, it compresses the magnetopause loca-

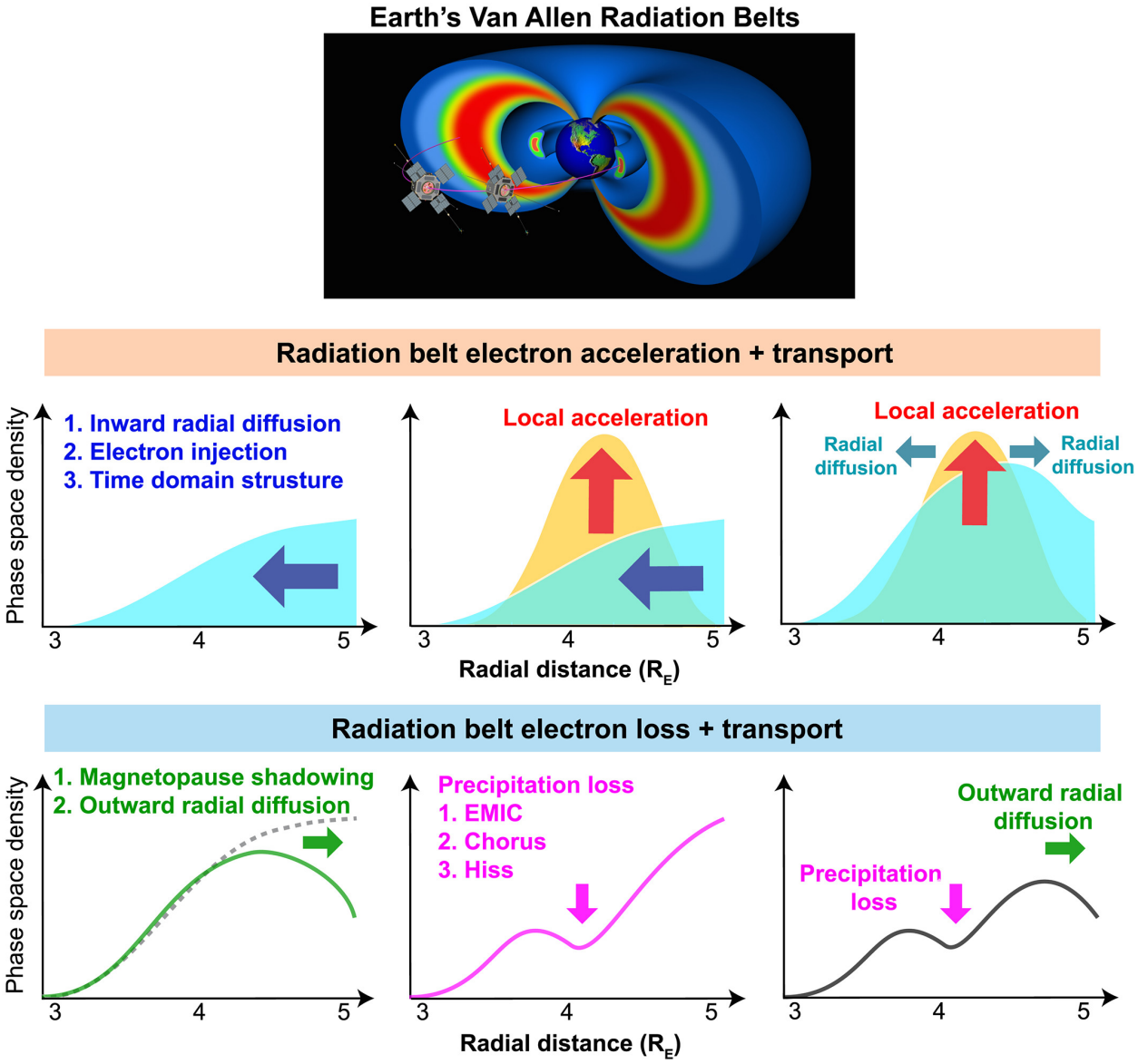

Figure 1.9: A schematic illustration summarizing the acceleration and loss processes of outer radiation belt electrons. (top) 3-D structure of the Van Allen radiation belts and the twin Van Allen Probes. (middle) Physical processes leading to radiation belt electron acceleration and transport. (bottom) Physical mechanisms driving radiation belt electron loss and transport. EMIC = Electromagnetic Ion Cyclotron [*Li and Hudson*, 2019].

tion, bringing it closer to the Earth, leading to the loss of trapped radiation belt electrons to the magnetopause, which is called the magnetopause shadowing effect [e.g., *Staples et al.*, 2022]. This creates a negative radial gradient in electron phase space density. The radiation belt electrons can also be further depleted by outward radial diffusion caused by ULF waves [*Loto'Aniu et al.*, 2010]. Various magnetospheric waves, such as EMIC waves, chorus, hiss, etc., scatter electrons through pitch angle scattering, leading to local precipitation loss into the upper atmosphere [e.g., *Zhang et al.*, 2022; *Miyoshi et al.*, 2008; *Inan et al.*, 2003]. The combination of magnetopause shadowing and precipitation loss efficiently drops out radiation belt electrons, resulting in multiple localized peaks in electron phase space density as shown in the lower right panel of Figure 1.9.

These different physical mechanisms combine to make the simulation and prediction of the dynamics of the radiation belts a very challenging task. In the meantime, the radiation belts are a known hazard to satellites and can cause deep dielectric charging, spurious signals, and total-dose-related degradation [e.g., *Lanzerotti et al.*, 1998; *Choi et al.*, 2011; *Lanzerotti*, 2001; *Fennell et al.*, 2001]. Thus, developing a useful model to describe the trapped electron flux has long been an important task for space physics research.

1.5 Outline and objectives of the thesis

This dissertation is organized into three parts. The first part is given in Chapter 3, which describes the machine-learning (ML) model of the Earth's radiation belt electron flux. The second part consists of chapters 4-5, which use explainable machine learning methods to understand the model we built and connect the conclusion with physical processes. The third part is Chapter 6, which discusses the results obtained from the ML model and how we combine them with traditional physical simulations of the radiation belt dynamics and our new findings from such simulations. To start with, Chapter 2 provides the theoretical background of the Fokker-Planck simulation and ML methods and also presents the basic

interpretable ML method we are going to use. Chapter 3 illustrates a set of ML models that covers different energy ranges of charged electrons in the radiation belts. We built for the first time an accurate ML model of the electron flux, and it also encourages a series of ML studies on different magnetospheric physics shown in the last chapter. Chapter 4 is the key of this dissertation, which illustrates that we can not only build an accurate ML model of radiation belt dynamics but also be able to explain them and connect them with physics. It is usually very hard to do this since the ML model is always highly nonlinear and with many parameters, considered as a 'Black Box' model. Chapter 5 presents a new method born from our interpretable ML method and tries to answer a long-lived question concerning how geomagnetic storms can result in either an increase or a decrease of the fluxes of relativistic electrons in the outer radiation belt. We implement a feature attribution method combined with traditional superposed epoch analysis and directly identify that the substorm is the controlling process. Chapter 6 is where we go back to physics and combine the previous understanding from ML studies. We first simulate all the electron enhancement events from 2012 to 2019 with Fokker-Planck simulation driven only by geomagnetic indices. In Chapter 7, we discuss those models born from our study and suggest future works.

CHAPTER 2

Theoretical and simulation background

This chapter primarily introduces the theoretical background and methods that will be employed in the subsequent chapters. To begin with, we discuss the Fokker-Planck equation, which is widely used in the simulation of radiation belts. The underlying physical mechanisms represented in the Fokker-Planck simulation are straightforward and often yield satisfactory results. We will utilize it in Chapter 6 to present specific effects we have found using machine learning in our studies. Subsequently, we will introduce one of the most common models in machine learning: neural networks, which we will also utilize in subsequent chapters. It is not only our model but many large language models that are changing our lives today, and fundamentally rely on neural networks. Hence, we will briefly explain the concept of neural networks and how such a model is trained. Lastly, we will touch upon the Shapley value, a cooperative game theory concept pertaining to contribution allocation. Its introduction is because we will employ this method to interpret our neural network model in Chapters 4-5.

2.1 The quasi-linear diffusion process

The basis of a complete quasi-linear theory is that, as a result of the action of waves, the zero-order distribution function of particles changes with time. Importantly, the time scale on which this happens is long compared with the period of the wave. The wave field and the perturbation of the distribution function are computed linearly and the nonlinear part of the quasilinear theory is the long-term effect of many waves on the background distribution [*Kennel and Engelmann*, 1966].

2.1.1 Resonant particle trajectories in velocity space

In a uniform plasma with a uniform background magnetic field, a charged particle travels with constant $v_\perp$ and $v_\parallel$ and, therefore, stays at the same point in velocity space. However, when the particle is in resonance with the wave, it's gyrophase remains in phase with the wave field, and then both $v_\perp$ and $v_\parallel$ may be permenantly changed. Consider a wave rest frame that moves parallel to the background magnetic field with phase speed $\omega/k_\parallel$. In this frame, the component of particle velocity that is parallel to the magnetic field is $v'_\parallel = v_\parallel - \omega/k_\parallel$. The distance it moves during one gyroperiod is $2\pi v'_\parallel/\Omega$. The resonance condition occurs when this distance is an integral number of wavelengths, and is described in Chapter 1 as: $\omega - k_\parallel v_\parallel - l\Omega = 0$. The electric field in the wave frame is electrostatic (not time varying) and the particle remains in phase with the wave fields. This means that there is no net transfer of energy to the particle in this frame of reference [*Walker*, 2013]. The conservation of kinetic energy thus can be written as:

$$v'^2_\parallel + v'^2_\perp = V_0^2 \tag{2.1}$$

where V_0 is constant. The effect of the wave on the particle is to change the pitch angle instead of the kinetic energy in this frame. In the plasma frame, this becomes

$$\left(v_\parallel - \frac{\omega}{k_\parallel}\right)^2 + v_\perp^2 = V_0^2. \tag{2.2}$$

This equation defines surfaces in velocity space, referred to as 'single-wave characteristics', on which particles are constrained to move during their interaction with small amplitude waves.

For frames moving with a relative velocity V_P, the formation of the particle velocity is

$$\begin{aligned} v'_\parallel &= \frac{v_\parallel - V_P}{1 - v_\parallel V_P/c^2} \\ v'_\perp &= \frac{\sqrt{1 - \left(v_\parallel^2 + v_\perp^2\right)/c^2}}{1 - v_\parallel V_P/c^2} v_\perp \end{aligned} \tag{2.3}$$

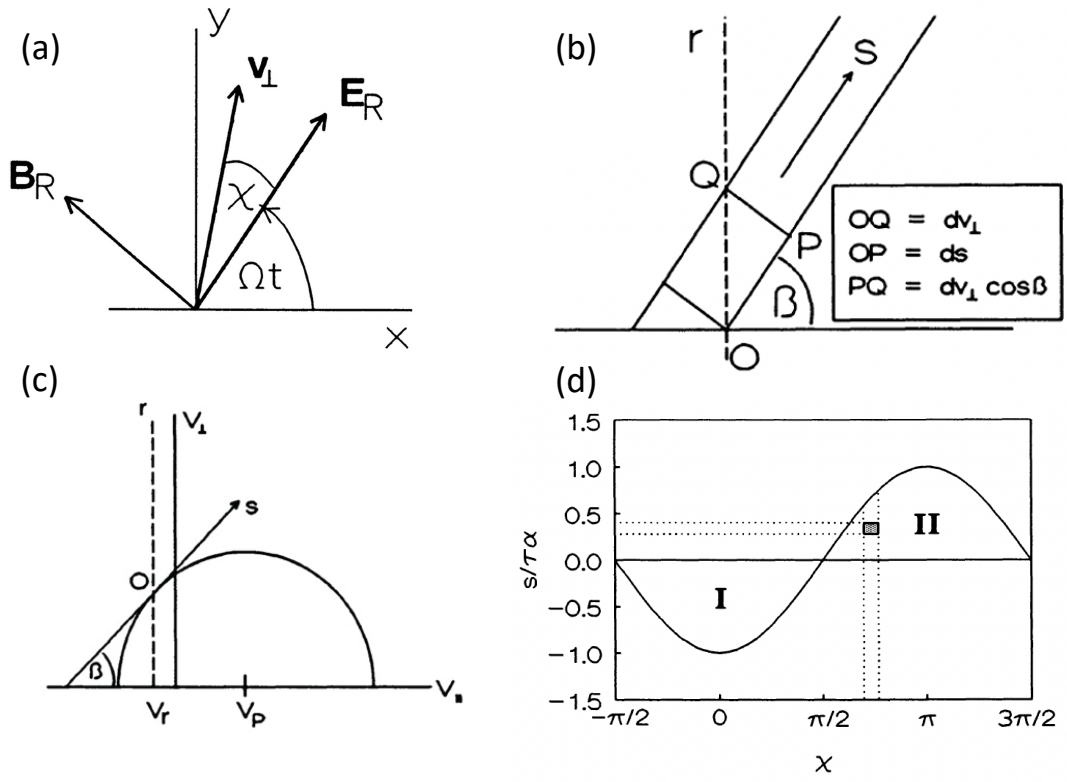

Figure 2.1: Diffusion in velocity space. For explanation see text. The figure is adapted from *Walker* [2013, chap. 8].

The kinetic energy is still conserved in the rest frame thus we can get the following:

$$v_\parallel^2 \left(1 - \frac{V_0^2 V_P^2}{c^4}\right) - 2V_\parallel V_P \left(1 - \frac{V_0^2}{c^2}\right) + v_\perp^2 \left(1 - \frac{V_P^2}{c^2}\right) = V_0^2 - V_P^2. \tag{2.4}$$

the resonance curve is now an ellipse rather than a circle in velocity space.

2.1.2 Diffusion in velocity space

At each point in the $(v_\perp, v_\parallel)$-plane for which resonance occurs with a wave of ω and $k_\parallel$, particles are equally likely to move in either direction along these single-wave characteristics. The rate and sense of the motion depend on the phase difference between particle and wave shown in Figure 2.1a for a right-hand polarized wave. The question is how to understand

the collective behavior with a specific particle distribution.

Figure 2.1c shows an example of non-relativistic resonance curve, and the resonance is located at $v_\parallel = V_R \equiv (\omega - \Omega)/k_\parallel$. The single wave characteristic is for a wave with phase speed $V_P = \omega/k_\parallel$ which is a circle centered on V_P. Figure 2.1b shows details of the region near the resonance location O. The s is the distance measured along the resonance curve. So near the resonance, the particle moves along the single wave characteristic at a rate:

$$\frac{ds}{dt} = \frac{1}{m\cos\beta}\left\langle \frac{dp_\parallel}{dt} \right\rangle = \Theta_l \cos\chi \tag{2.5}$$

Where the Θ_l has the dimensions of acceleration. The change in the average parallel component of momentum is calculated as $\left\langle \frac{dp_\parallel}{dt} \right\rangle = \hat{\mathbf{b}}.q\langle[\mathbf{E}+\mathbf{v}\times\mathbf{B}]\rangle$ (The perpendicular momentum always averages to zero because of the background magnetic field) and the averages are taken over many gyroperiods. The result is proportional to $\cos\chi$ (which is related to $\mathbf{v}\times\mathbf{B}$) and the detailed derivation can be found in *Walker* [2013, chap. 8].

Figure 2.1d then shows the curve of $s = \Theta_l \tau \cos\chi$. The particles in the region I are moving in the $+s$ direction and all those in the region II are moving in the $-s$ direction. In the neighborhood of the resonance, the distribution function can be approximately described as:

$$f_0(s, v_\perp) \simeq f_0(0, v_\perp) + s\left.\frac{\partial f_0}{\partial s}\right|_{s=0} \tag{2.6}$$

As the behavior of the wave-particle interaction is different for different phase χ (see Equation 1.17), the phase intergrated version of the distribution must integrate with the volume element $v_\perp d\chi dv_\perp dv_\parallel = v_\perp \cos\beta d\chi ds dv_\perp$. The positive flux is thus

$$\begin{aligned} &\frac{v_\perp \cos\beta \delta v_\perp}{\pi\tau v_\perp \delta v_\perp} \int_{-\pi/2}^{\pi/2}\int_{-\tau\Theta_l\cos\chi}^{0} \left\{ f_0 + s\frac{\partial f_0}{\partial s} \right\} d\chi ds \\ &\quad = \frac{\cos\beta}{\pi\tau}\int_{-\pi/2}^{\pi/2} \tau\Theta_l\cos\chi \left[f_0 - \frac{1}{2}\tau\Theta_l\cos\chi\frac{\partial f_0}{\partial s}\right] d\chi \end{aligned} \tag{2.7}$$

In the same way, the negative flux is

$$\begin{aligned}\frac{v_\perp \cos\beta \delta v_\perp}{\pi\tau v_\perp \delta v_\perp} \int_{\pi/2}^{3\pi/2} \int_0^{-\tau\Theta_l \cos\chi} \left\{ f_0 + s\frac{\partial f_0}{\partial s} \right\} d\chi ds \\ = \frac{\cos\beta}{\pi\tau} \int_{\pi/2}^{3\pi/2} \tau\Theta_l \cos\chi \left[-f_0 + \frac{1}{2}\tau\Theta_l \cos\chi \frac{\partial f_0}{\partial s} \right] d\chi\end{aligned} \tag{2.8}$$

So the net flux is the difference between these

$$\Pi = \frac{\Theta_l \cos\beta}{\pi} \int_{-\pi/2}^{3\pi/2} \left[f_0 \cos\chi - \frac{1}{2}\tau\Theta_l \cos^2\chi \frac{\partial f_0}{\partial s} \right] d\chi = -\frac{1}{2}\tau\Theta_l^2 \cos\beta \frac{\partial f_0}{\partial s} \tag{2.9}$$

Conservation of particles requires that f_0 obeys a conservation equation in velocity space of the form $\frac{\partial f_0}{\partial t} + \nabla_v \cdot \Pi = 0$. and the flux is along the single wave characteristics. Thus this leads to

$$\frac{\partial f_0}{\partial t} = \frac{1}{\cos\beta} \frac{\partial}{\partial s} \left(\frac{1}{2}\tau\Theta_l^2 \cos\beta \frac{\partial f_0}{\partial s} \right) \tag{2.10}$$

which can recognized as a diffusion equation $\frac{\partial f}{\partial t} = \nabla \cdot (\mathbf{D} \cdot \nabla f)$ and the $\mathbf{D}$ represents the diffusion coefficents. An example is shown in Figure 2.2. The arrows indicate the particles moving along the diffusion curves and the directions are always toward decreasing distribution function values f. The above derivation only shows one single wave mode. In the magnetosphere, a broad wave spectrum always exists. A general expression for the quasi-linear diffusion of plasma particles in the presence of a specified wave distribution can be found in *Kennel and Engelmann* [1966], where the diffusion formula still holds.

The simulation of such a diffusion process is also named the Fokker-Planck equation [*Fokker*, 1914]. A useful coordinate transformation is from $(v_\perp, v_\parallel)$ to the (v, α) space (or $(p_\perp, p_\parallel)$ to the (p, α) for relativistic conditions) as the magnetospheric particle distribution is often expressedas a function of pitch angle and energy [*Lyons and Williams*, 2013]. In addition, the particles experience bouncing in the radiation belts. Thus, taking the average diffusion over a bouncing period is very common in the radiation belt flux simulations. The formula we use in Chapter 6 is the bounce-averaged 2D Fokker-Planck equation [*Ma et al.*,

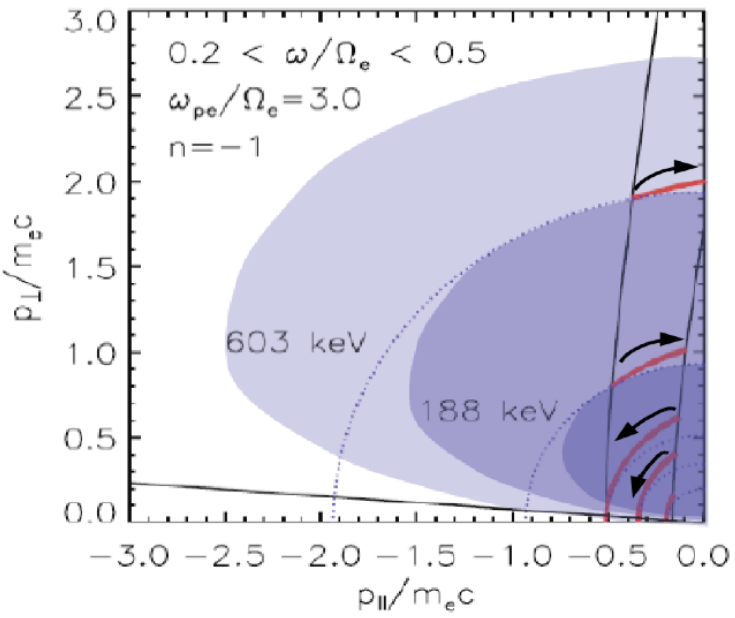

Figure 2.2: Particle interaction with whistler wave in the phase space: Phase space density (blue contour) decreases with increasing energy, with a peak at 90 and a loss cone. Resonance ellipse (black solid) and Diffusion surface (red solid). Particles move along the diffusion surface from higher to lower phase space densities in the regime of resonance ellipse. The figure is adapted from *Horne and Thorne* [2003].

2012]:

$$\begin{aligned}\frac{\partial f}{\partial t} = & \frac{1}{S\left(\alpha_{\mathrm{eq}}\right)\sin\alpha_{\mathrm{eq}}\cos\alpha_{\mathrm{eq}}}\frac{\partial}{\partial\alpha_{\mathrm{eq}}}\left(S\left(\alpha_{\mathrm{eq}}\right)\sin\alpha_{\mathrm{eq}}\cos\alpha_{\mathrm{eq}}\left\langle D_{\alpha_{\mathrm{eq}}\alpha_{\mathrm{eq}}}\right\rangle\frac{\partial f}{\partial\alpha_{\mathrm{eq}}}\right) \\ & + \frac{1}{S\left(\alpha_{\mathrm{eq}}\right)\sin\alpha_{\mathrm{eq}}\cos\alpha_{\mathrm{eq}}}\frac{\partial}{\partial\alpha_{\mathrm{eq}}}\left(S\left(\alpha_{\mathrm{eq}}\right)\sin\alpha_{\mathrm{eq}}\cos\alpha_{\mathrm{eq}}p\left\langle D_{\alpha_{\mathrm{eq}}p}\right\rangle\frac{\partial f}{\partial p}\right) \\ & + \frac{1}{p^2}\frac{\partial}{\partial p}\left(p^3\left\langle D_{p\alpha_{\mathrm{eq}}}\right\rangle\frac{\partial f}{\partial\alpha_{\mathrm{eq}}}\right) \\ & + \frac{1}{p^2}\frac{\partial}{\partial p}\left(p^4\left\langle D_{pp}\right\rangle\frac{\partial f}{\partial p}\right)\end{aligned} \tag{2.11}$$

where the $S(\alpha_{eq})$ is the bounce period $S\left(\alpha_{eq}\right) = 1.38 - 0.32\sin\left(\alpha_{eq}\right) - 0.32\sqrt{\sin\left(\alpha_{eq}\right)}$ [*Lenchek et al.*, 1961].

2.1.3 Example of local acceleration in radiation belts

The local acceleration of highly energetic electrons from 100s keV to several MeV due to the interactions with chorus waves has been successfully modeled by the 2D radiation belt model with Fokker-Planck simulation. Figure 2.3 shows an example simulation of a rapid relativistic electron enhancement event on 9 October 2012 measured by Van Allen Probes [*Thorne et al.*, 2013]. The peak of Phase Space Density (PSD) after the storm is located at the heart of the radiation belt of $L \sim 5$; thus, the observation results are inconsistent with acceleration by inward radial diffusion process [*Ukhorskiy et al.*, 2009]. The chorus wave could be a potential candidate for such local electron acceleration [*Horne and Thorne*, 1998; *Summers et al.*, 1998; *Horne and Thorne*, 2003]. However, the chorus observation obtained from Van Allen Probes at the same period was confined to a limited MLT range. *Thorne et al.* [2013] use the ratio between the precipitated and trapped fluxes measured by low altitude POES satellites [*Kennel and Petschek*, 1966] to approximately model the power spectral intensity of magnetospheric chorus across all the MLT range. With the resulting chorus wave properties and measured electron density profile, they performed the 2D Fokker-Planck simulation at L = 5. The right part of Figure 2.3 shows the comparison between the observation and simulation results. The simulation of the dynamic response of relativistic electrons to chorus scattering agrees well with the observations obtained from the Relativistic Electron–Proton Telescope (REPT)[*Baker et al.*, 2012] instrument. The delayed enhancement of the higher energy electrons and the good agreement between the simulated pitch angle distribution and REPT observation confirm that the chorus scattering to electron acceleration during this storm is the dominant process for relativistic electron acceleration.

Numerous studies have tended to include different physical processes into the diffusion simulation [e.g., *Ma et al.*, 2017; *Drozdov et al.*, 2015; *Shprits et al.*, 2009; *Tu et al.*, 2013; *Ma et al.*, 2018]. However, they nevertheless suffer from several critical issues which limit its general use: 1. The FP simulation requires the time-varying distribution of waves near the Earth be constantly supplied to the model in order to calculate the diffusion coefficients.

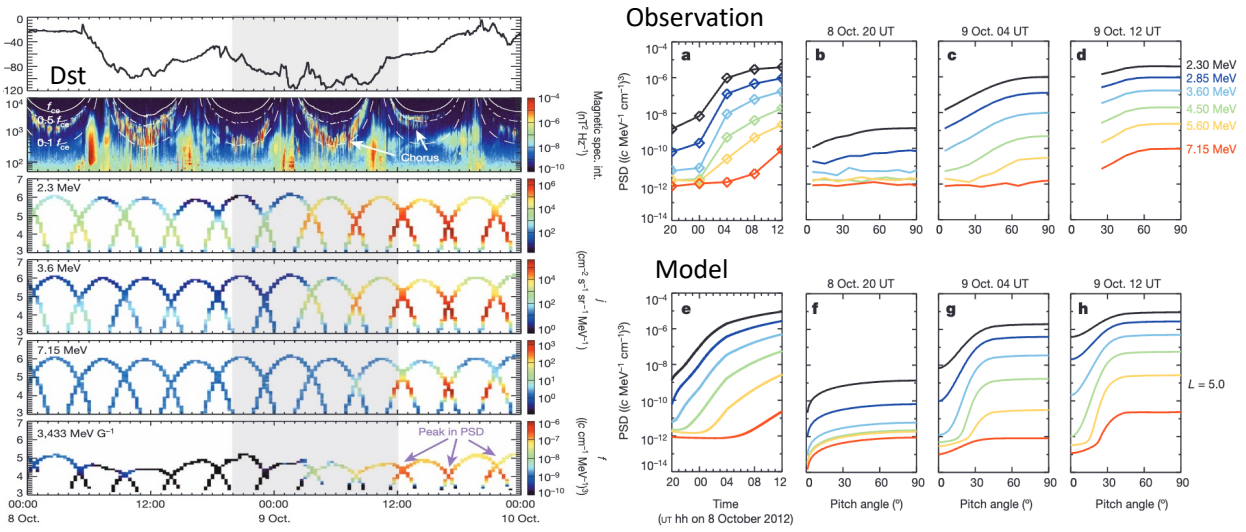

Figure 2.3: Rapid relativistic electron acceleration on 9 October 2012. Left part from top to bottom: 1. The Dst index; 2. Magnetic spectral intensity of highly-structured whistler-mode chorus waves as a function of frequency observed by the EMFISIS instrument on Van Allen probe A; 3-5: Relativistic electron flux observation at 2.3, 3.6 and 7.15 MeV; 6: The phase space density ($f = j/p^2$) of 3433 MeVG^{-1}. Right part: a to d: observation of phase space density during the event; e to h: the Fokker-Planck simulation results. The figure is adapted from *Thorne et al.* [2013].

Typically the wave can be parameterized by geomagnetic activity [e.g., *Li et al.*, 2009]. But this approach is statistical in nature and reproduces a 'statistically averaged' event and always fails at simulating high energetic electrons [e.g., *Drozdov et al.*, 2015]. There is also no guarantee that such parameterization is unique. 2. The FP modeling approach can only represent the effects of diffusive scattering on the particles. It cannot represent nonlinear processes nor include any unknown (or unquantified) physical process that might shift the balance between acceleration and loss processes. The primary objective of this dissertation is to explore different and better methods to simulate the radiation belts, and our main approach is the use of machine learning methods.

2.2 Machine learning method: neural network

Machine learning (ML) is a field of study in artificial intelligence concerned with developing and studying statistical algorithms that can learn from data and generalize to unseen data, and thus perform tasks without explicit instructions [*Samuel*, 1959]. ML is rapidly changing our lives, and the development of ML over the past decade has been astounding. We can observe that large language models, like ChatGPT and its backend models [e.g., *Floridi and Chiriatti*, 2020], can converse and perform various tasks just like humans. Machine learning involves the study of algorithms, more precisely, the study of learning algorithms, to continuously learn, generate, and update models based on the data we provide [*LeCun et al.*, 2015]. Among them, neural networks are the most important and widely used, which is the method I will be employing in this dissertation. The concept of neural networks is widely applied in various deep learning models, even in the complex large language models that are based on the transformer architecture [*Vaswani et al.*, 2017]. In the subsequent chapters, we will be using just a basic multilayer perceptron neural network, which is already capable of effectively reconstructing certain physical phenomena, showing the power of neural networks [*Cybenko*, 1989]. In this section, we briefly introduce what neural networks are and the core backpropagation (BP) algorithm.

2.2.1 Model structure and activation function

In biological neural networks, the most basic component is the neuron. Each neuron is linked to other neurons. When a certain neuron exceeds a threshold, it becomes activated and sends chemical substances to other neurons [*Kohonen*, 1988]. Such an idea is the basis of neural networks in computer science. Figure 2.4 demonstrates the architechture of a multi-layer perception model (MLP) with a hidden layer of five hidden units, and each node can be considered as a "neuron". We use matrix $\mathbf{X} \in \mathbb{R}^{n \times d}$ as n samples where each has d inputs or features. For one-hidden-layer MLP, we denote by $\mathbf{H} \in \mathbb{R}^{n \times h}$ the outputs of the hidden

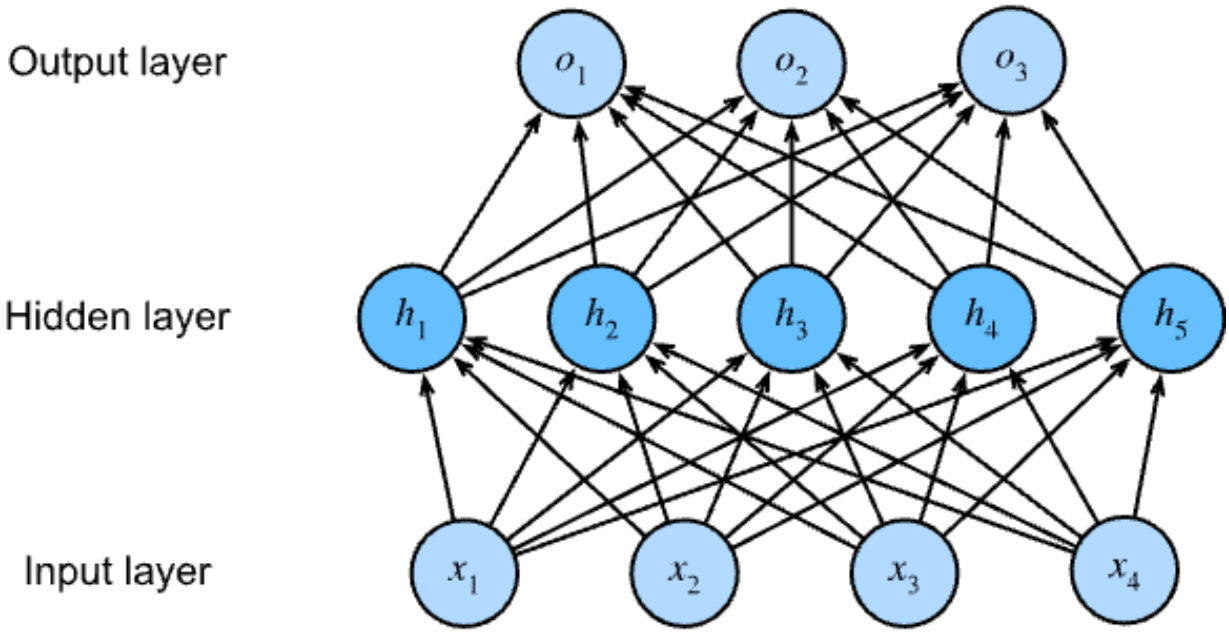

Figure 2.4: A multi-layer perception with a hidden layer of five hidden units. [*Zhang et al.*, 2023]

layer. As can be seen, each unit is fully connected to the units in the adjacent layers. Each neuron accept the signal from the input layer and has hidden layer weights $\mathbf{W}^{(1)} \in \mathbb{R}^{d\times h}$ and biases $\mathbf{b}^{(1)} \in \mathbb{R}^{1\times h}$. So every hidden-layer neuron can receive a signal and has an output:

$$\mathbf{H} = \mathbf{X}\mathbf{W}^{(1)} + \mathbf{b}^{(1)} \tag{2.12}$$

We further denote output-layer weights $\mathbf{W}^{(2)} \in \mathbb{R}^{h\times q}$ and biases $\mathbf{b}^{(2)} \in \mathbb{R}^{1\times q}$, then the outputs $\mathbf{O} \in \mathbb{R}^{n\times q}$ of this MLP model can be written as

$$\mathbf{O} = \mathbf{H}\mathbf{W}^{(2)} + \mathbf{b}^{(2)} \tag{2.13}$$

However, if we combine Equation 2.12 and 2.13, one can realize that this is still a linear model, which cannot capture nonlinear dependencies in the data:

$$\mathbf{O} = \left(\mathbf{X}\mathbf{W}^{(1)} + \mathbf{b}^{(1)}\right)\mathbf{W}^{(2)} + \mathbf{b}^{(2)} = \mathbf{X}\mathbf{W}^{(1)}\mathbf{W}^{(2)} + \mathbf{b}^{(1)}\mathbf{W}^{(2)} + \mathbf{b}^{(2)} = \mathbf{X}\mathbf{W} + \mathbf{b}$$

The key point is that we need a nonlinear activation function σ to be applied to each hidden unit, so then it becomes a nonlinear model

$$\begin{aligned} \mathbf{H} &= \sigma\left(\mathbf{X}\mathbf{W}^{(1)} + \mathbf{b}^{(1)}\right) \\ \mathbf{O} &= \mathbf{H}\mathbf{W}^{(2)} + \mathbf{b}^{(2)} \end{aligned} \tag{2.14}$$

The most popular choice of the activation function is the rectified linear unit (ReLU) [*Nair and Hinton*, 2010] which provides simple nonlinear transformation as

$$\mathrm{ReLU}(x) = \max(x, 0) \tag{2.15}$$

A simple understanding of such an activation function is that the signal has to be larger than 0 and then can be "activated". An online example for a simple neural network model can be found in `https://playground.tensorflow.org/`.

2.2.2 Backpropagation

Backward propagation or backpropagation describes how to calculate or update the parameters of the neural network (weights and bias in each layer) during the training process. We start from one sample $\mathbf{x} \in \mathbb{R}^d$ and ignore the bias term of the hidden layer discussed in the last section. We obtain an output layer variable $\mathbf{o}$:

$$\begin{aligned} \mathbf{z} &= \mathbf{W}^{(1)}\mathbf{x} \\ \mathbf{h} &= \phi(\mathbf{z}) \\ \mathbf{o} &= \mathbf{W}^{(2)}\mathbf{h}. \end{aligned} \tag{2.16}$$

Assuming for the sample $\mathbf{x}$, the label or the true value or the observation of this sample is $\mathbf{y}$, we can define some loss function l to describe the difference between the output of the model and the label:

$$L = l(\mathbf{o}, \mathbf{y}) \tag{2.17}$$

Now with the chain rule, we can update each parameter in the network based on some learning rate η and gradient descent: $\Delta W = -\eta \frac{\partial L}{\partial W}$. Specifically, it's used to find the

parameters (weights) of a function (usually the loss function in a neural network) that result in the smallest possible error by updating these parameters in the opposite direction of the gradient of the loss function with respect to the parameters. The learning rate determines the size of the steps we take to reach a (local) minimum. And we can easily get any derivation based on the chain rule, for example:

$$\frac{\partial L}{\partial \mathbf{W}^{(1)}} = \frac{\partial L}{\partial \mathbf{o}} \frac{\partial \mathbf{o}}{\partial \mathbf{h}} \frac{\partial \mathbf{h}}{\partial \mathbf{z}} \frac{\partial \mathbf{z}}{\partial \mathbf{x}} \tag{2.18}$$

which means we can update any parameters in the neural network.

While the principle may seem simple, there are various engineering challenges in its practical application. For instance: How can we train a model with massive amounts of data? How can we make the program run faster? How can we prevent model overfitting? How should I choose the parameters of the model? We won't go into detail here, but these are important questions for researchers who aren't in the machine learning field but wish to utilize machine learning methods, and more detail can be found in *Zhang et al.* [2023].

ML tasks related to space physics often deal with data obtained from satellite mission. Preparing such data ready for learning is a significant challenge but often overlooked. ML training process typically involves dividing data into different datasets to prevent overfitting and to test model performance. However, the common method of random splitting is usually not applicable to satellite data due to the temporal and spatial continuity in the physical measurements they represent. This can lead to indistinct datasets (not independent) that fail to serve the purpose of preventing overtraining and we will introduce this issue in the radiation belts modeling in Chapter 3.

2.3 Shapley values in Game theory

The Shapley value was originally developed by Lloyd Shapley in cooperative game theory [*Shapley*, 1953]. Multiple players collaborate and generate a certain outcome or value. The Shapley value provides a mechanism to distribute the total generated value among the

players in a manner that is fair and unbiased considers all possible combinations of player participation in various groups or coalitions. This distribution is guided by a set of axioms, ensuring that the allocation is fair and representative of each player's marginal contribution, described further in the example below.

Probability	Order of arrival	1's marginal contribution	2's marginal contribution	3's marginal contribution
$\frac{1}{6}$	first 1 then 2 then 3: 123	$v(\{1\}) = 100$	$v(\{1,2\}) - v(\{1\}) = 270 - 100 = 170$	$v(\{1,2,3\}) - v(\{1,2\}) = 500 - 270 = 230$
$\frac{1}{6}$	first 1 then 3 then 2: 132	$v(\{1\}) = 100$	$v(\{1,3,2\}) - v(\{1,3\}) = 375 - 100 = 275$	$v(\{1,3\}) - v(\{1\}) = 375 - 100 = 275$
$\frac{1}{6}$	first 2 then 1 then 3: 213	$v(\{1,2\}) - v(\{2\}) = 270 - 125 = 145$	$v(\{2\}) = 125$	$v(\{1,2,3\}) - v(\{1,2\}) = 500 - 270 = 230$
$\frac{1}{6}$	first 2 then 3 then 1: 231	$v(\{1,2,3\}) - v(\{2,3\}) = 500 - 350 = 150$	$v(\{2\}) = 125$	$v(\{2,3\}) - v(\{2\}) = 350 - 125 = 225$
$\frac{1}{6}$	first 3 then 1 then 2: 312	$v(\{1,3\}) - v(\{3\}) = 375 - 50 = 325$	$v(\{1,3,2\}) - v(\{1,3\}) = 500 - 375 = 125$	$v(\{3\}) = 50$
$\frac{1}{6}$	first 3 then 2 then 1: 321	$v(\{1,2,3\}) - v(\{2,3\}) = 500 - 350 = 150$	$v(\{2,3\}) - v(\{3\}) = 350 - 50 = 300$	$v(\{3\}) = 50$

Table 2.1: Calculation of Marginal Contributions for Shapley Value

Table 2.1 shows an example of Shapley value calculation example. Assume a code project

with 500 lines needs to be finished by three students, each student's individual coding ability is expressed by the lines of code each can generate:

$$v(1) = 100, v(2) = 125, v(3) = 50.$$

When they cooperate with each other, they get a higher efficiency. For each pair of students, the lines of code generated are:

$$v(1,2) = 270, v(2,3) = 350, v(1,3) = 375$$

Together, they will be able to finish the code, such that their combined coding is:

$$v(1,2,3) = 500$$

The question is, what is the proper way to quantify the contribution of each student? The solution is to calculate the marginal contribution. The marginal contribution of a player (in our case is student) is defined as the difference in value generated by a coalition including that player and the value generated by the coalition without that player. In other words, it measures how much additional value the player brings to the coalition. For example, $v(1,2) - v(1) = 170$ means the marginal contribution of student 2 when student 1 and 2 working together is 170, compared to when student 1 worked independently.

The Shapley value of a player is computed as the weighted average of the marginal contributions of that player across all possible coalitions. The formula considers all the permutations of players and calculates the contribution of a player to each possible coalition they can be part of. For three students there are 6 possibilities when considering different order of arrival, and after all the possible combination shown in Table 2.1, the contribution from the first student is:

$$\varphi_1(v) = \frac{1}{6}(100 + 100 + 145 + 150 + 325 + 150) = \frac{970}{6},$$

the second is:

$$\varphi_2(v) = \frac{1}{6}170 + \frac{1}{6}125 + \frac{1}{6}125 + \frac{1}{6}125 + \frac{1}{6}125 + \frac{1}{6}300 = \frac{970}{6},$$

and the third is:

$$\varphi_3(v) = \frac{1}{6}230 + \frac{1}{6}275 + \frac{1}{6}230 + \frac{1}{6}225 + \frac{1}{6}50 + \frac{1}{6}50 = \frac{1060}{6}.$$

The total contribution is $\frac{970}{6} + \frac{970}{6} + \frac{1060}{6} = 500$.

The Shapley value can be proved to posess many desirable properties. The most important one is efficiency which means the sum of the Shapley value of all agents or players equals the value of total coalition, as we just showed that the total lines of three students are 500:

$$\sum_{i \in N} \varphi_i(v) = v(N), \tag{2.19}$$

where N is the set of players.

Building on the foundation of the Shapley value from cooperative game theory, SHAP (SHapley Additive exPlanations) extends this concept to the field of machine learning, particularly for the interpretation of model predictions [*Lundberg and Lee*, 2017] where the players in the game are now taken to be the model features. We will introduce this SHAP method in Chapter 4.

CHAPTER 3

ORIENT: Outer RadIation belt Electron flux Neural neTwork model

In this chapter, we present a set of neural network models that reproduce the dynamics of electron fluxes in the range of 50 keV $\sim$ 1 MeV in the outer radiation belt. The Outer Radiation belt Electron Neural net model for Medium energy electrons (ORIENT-M) uses only solar wind conditions and geomagnetic indices as input. The models are trained on electron flux data from the Magnetic Electron Ion Spectrometer (MagEIS) instrument on-board Van Allen Probes, and they can reproduce the dynamic variations of electron fluxes in different energy channels. The model results show high coefficient of determination ($R^2 \sim$ 0.78-0.92) on the test dataset, which is an out-of-sample 30-day period from February 25 to March 25 in 2017, when a geomagnetic storm took place, as well as an out-of-sample one year period after March 2018. In addition, the models are able to capture electron dynamics such as intensifications, decays, dropouts, and the Magnetic Local Time (MLT) dependence of the lower energy ($\sim<$ 100 keV) electron fluxes during storms. The models have reliable prediction capability and can be used for a wide range of space weather applications. The general framework of building our model is not limited to radiation belt fluxes and could be used to build machine learning models for a variety of other plasma parameters in the Earth's magnetosphere, including density [*Bortnik et al.*, 2016a; *Chu et al.*, 2017a] and waves [*Huang et al.*, 2022; *Chu et al.*, 2023; *Bortnik et al.*, 2018].

3.1 Introduction

As discussed in Chapter 1, the exact response of the radiation belts to solar wind driving is difficult to predict due to various competing loss and acceleration processes, often giving vastly different responses to seemingly similar driving conditions [*Reeves et al.*, 2003] but occasionally even being accelerated up to roughly 10 MeV. The generally accepted process of radiation belt flux enhancement is believed to proceed as follows: an increase in the strength of the convection electric field causes an enhanced drift of plasma-sheet electrons into the inner magnetosphere, where they gradient-drift eastwards, and become unstable to plasma wave excitation. A particular class of waves, called whistler-mode chorus waves is excited on the dawn side of the Earth by ∼10-100 keV 'source' electrons, and these waves then transfer a portion of their energy to higher energy 'seed' electrons (>100 keV), that are further accelerated to relativistic energies (∼MeV) facilitated by Ultra-Low Frequency (ULF) waves [e.g., *Bortnik and Thorne*, 2007; *Li et al.*, 2006; *Reeves et al.*, 2003; *Thorne et al.*, 2013]. Thus, developing useful models to describe the trapped electron flux across a range of different energy channels is important for understanding and predicting the dynamics and distribution of the radiation belts.

The outer radiation belt electron fluxes and their dynamics have been modeled using a variety of approaches including both data-driven and physics-based models. The empirical AE8 and AE9 models are statistical models which are static, and reconstruct the distribution of electrons from 40 keV to 7 MeV [*Ginet et al.*, 2013; *Sawyer and Vette*, 1976]. Other statistical models such as CRRESELE [*Brautigam and Bell*, 1995] covers 500 keV ∼ 6.6 MeV, the IGE-2006 [*Sicard-Piet et al.*, 2008] and the POLE [*Sicard-Piet et al.*, 2006] are applicable only for geostationary orbit, whereas the FLUMIC [*Wrenn et al.*, 2000] and the MODE-DIC model [*Hands et al.*, 2015] model the worst case scenario for 1-day fluence and environment for spacecraft internal charging. These empirical models depend on L shell and energy but are usually independent of geomagnetic activity, meaning that they are static,

i.e., they reproduce 'statistically averaged' conditions. Several machine learning models have also been developed to study trapped electron fluxes in the radiation belts. These include *Balikhin et al.* [2011] who used the Nonlinear Autoregressive Moving Average with Exogenous inputs (NARMAX) approach, and *Zhang et al.* [2020] who used Artificial Neural Networks (ANNs) with quantile regression. Both models focus on the fluxes at geosynchoronous (GEO) orbit. *Smirnov et al.* [2020] adopted a gradient boosting decision tree (GBDT) method on GPS data to model the fluxes of electrons with energies in the range 120-600 keV in the MEO region which only captures one altitude. *Lima et al.* [2020] used a combination of data collected at low earth orbit and LANL-01A at GEO orbit and POES electron fluxes as the input of the model to predict MeV energy flux and *Claudepierre and O'Brien* [2020] also included POES data from LEO as the driver of their neural network model, which operates on a daily cadence.

Using physics-based models is another important way to replicate and understand the dynamic behavior of the radiation belts as discussed in Section 2.1. The common method is through the integration of the Fokker-Planck (FP) equation [*Lyons and Thorne*, 1973; *Glauert et al.*, 2014; *Ma et al.*, 2015; *Reeves et al.*, 2012; *Tu et al.*, 2013]. However, the FP model can only represent the effects of diffusive scattering on the particles, it cannot represent nonlinear processes, nor include any unknown (or unquantified physical process which might shift the balance between acceleration and loss processes). And such physical-based modeling requires artificial or observed initial and boundary conditions to drive the simulation which also need to be specified during the course of the simulation.

Here, we present a novel strategy based on the Artificial Neural Network (ANN) model to overcome some of these shortcomings. This approach is versatile and can be applied to a variety of physical quantities sampled at sparse locations and times, and has already been utilized in space weather modeling the plasma density, chorus and hiss waves, and in conjunction with physics-based radiation belt modeling [*Bortnik et al.*, 2016a; *Chu et al.*, 2017a, 2021]. We describe and demonstrate the development of several ANN models of outer

radiation belt electron fluxes covering energy channels from ∼50 keV to ∼1 MeV based on Van Allen Probes data. Since solar wind driving and geomagnetic activity alone determine the fluctuation of the outer radiation belt, the neural network model accepts these parameters as inputs without relying on any boundary conditions from other satellite data, making this model a tool with great potential in predicting and understanding radiation belt dynamics. We show that our electron flux model captures the dominant features of the variability at different time scales, as well as the energy-dependent dynamics and the MLT dependence of the low energy channel.

3.2 Data description: electron flux measurement from Van Allen Probes

3.2.1 MagEIS Electron Flux data

The primary data used throughout this work are obtained from the Magnetic Electron Ion Spectrometer (MagEIS) instrument suite [*Blake et al.*, 2014] onboard NASA's Van Allen Probes [*Mauk et al.*, 2014]. The identically instrumented twin-spacecraft Van Allen Probes mission has a highly elliptical low-inclination orbit with an apogee of $\sim 6R_E$ and a perigee of $\sim$ 600 km. The MagEIS instruments measure electron fluxes throughout this orbit over a wide energy range (∼30-4 MeV) with four electron spectrometers (LOW:∼30-200keV, M75, and M35:∼200 keV to 1 MeV, HIGH: 1-4MeV). The current study illustrates the capabilities of the machine learning model using four selected energy channels from the MagEIS instrument (54 keV, 235 keV, 597 keV, and 909 keV shown in Figure 3.1). Extensive background correction of MagEIS spin-averaged fluxes was performed to remove background contamination due to inner belt protons and high energy electrons that produce bremsstrahlung X rays [*Claudepierre et al.*, 2015, 2019]. However, there are periods when the background correction cannot be performed, and as a result, background corrected MagEIS data at energies <∼220 keV is only available at L > 4 on RBSP-B. For lower energy electron fluxes, the drift

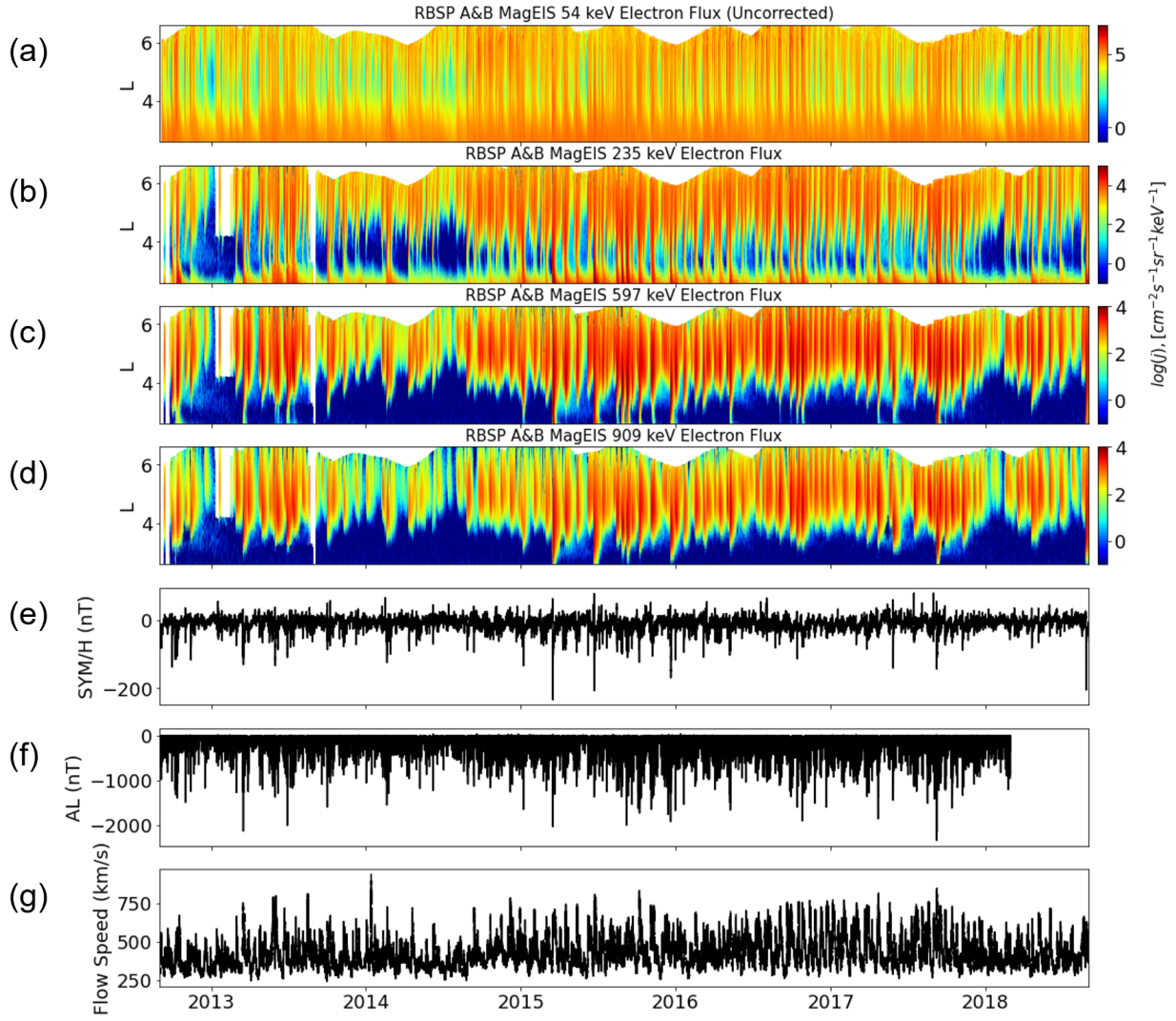

Figure 3.1: (a-d) Spin-Averaged fluxes of electrons with energies of 54, 235, 597, 909 keV from MagEIS on RBSP A and B for the indicated time interval. The MagEIS fluxes reflect uncorrected data for channel 54 keV and corrected data for the remaining channels. (e-g) 5-minute resolution SYM-H and AL indices and solar wind speed from the OMNI dataset.

period is relatively long. Thus the data available on both probes are preferentially used in our study in order to capture the magnetic local time (MLT) dependence. For the above reasons, we use uncorrected data on 54 keV channel and background corrected data on other three channels.

3.2.2 OMNI dataset

The variation of the Earth's outer radiation belt is known to be driven by the solar wind (e.g., solar wind pressure leading to magnetopause shadowing, inward convection of plasma from the tail, and creation of ultra-low frequency waves facilitating radial diffusion) and the resultant geomagnetic activity (e.g., whistler-mode chorus and hiss waves induced by the plasma injections from the magnetotail). Therefore, the neural network model uses both solar wind parameters as well as geomagnetic indices acquired from the OMNI data set (`https://omniweb.gsfc.nasa.gov/`) as input parameters (5-minute resolution). It is important to use both because occasionally structures observed in the solar wind can miss the Earth resulting in minimal geomagnetic activity, or vice versa, so using both solar wind parameters and geomagnetic indices reflects both fundamental drivers and their geoeffectiveness [*Walsh et al.*, 2019]. The OMNI AL and AE indices end after March 1 2018, so the electron flux data used in the model training process is from October 2012 to February 2018. The candidate input parameters include AE, AL, AU, ASY-D, ASY-H, Bz-GSM, E, solar wind velocity, solar wind pressure, proton density, SYM-H, and SYM-D.

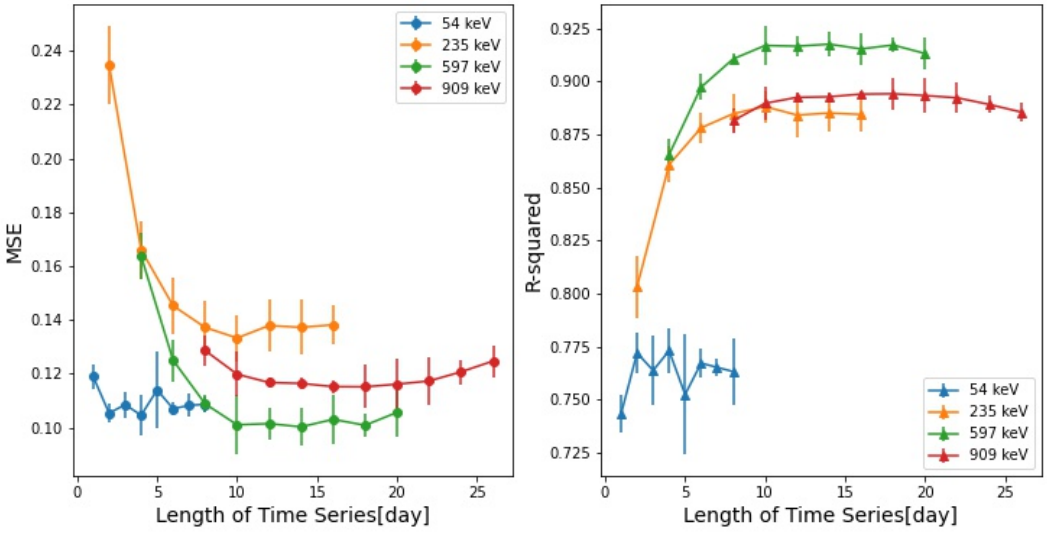

Figure 3.2: Model performance on the test dataset using different lengths of time series as input parameters for each channel. The error bars show the median and standard deviation of MSE (left panel) and coefficient of determination R^2.

3.3 Method: training a machine-learning model from satellite observation

3.3.1 Model description

We use a simple fully connected Multi-Layer Perceptron (MLP) model to reconstruct the energetic electron fluxes from several different channels throughout the outer radiation belt. The approach represents an extension of the technique used in a number of previous studies, which successfully modeled plasma density, waves, and electron fluxes [*Bortnik et al.*, 2016a, 2018; *Chu et al.*, 2017a,b]. The input parameters used for each neuron in layer l are the products of the output of the preceding layer's $(l-1)$ nodes with their associated weights

$$z_j^l = f\left(\sum_{i=0}^{N-1} z_i^{l-1} w_{ij} + b_i\right) \tag{3.1}$$

where i and j denote the neuron number in the preceding $(l-1)$ and current (l) layers, respectively, and w_{ij} and b_i are the weights and biases in the hidden layer. The output of each neuron in the hidden layers is calculated using a RELU activation function

$$f\left(z^l\right) = \max\left(0, z^l\right) \tag{3.2}$$

which is one of the most widely used activation functions in deep learning [*LeCun et al.*, 2015; *Nair and Hinton*, 2010]. After each hidden layer, we place a batch normalization layer to prevent the vanishing and exploding gradient problem [*Ioffe and Szegedy*, 2015].

The outputs of the preceding $(l-1)$ layer's neurons are all used as the inputs of the neurons in the next layer (l), thus creating a fully-connected feedforward neural network. Since the corrected MagEIS electron fluxes has many zero values, the model takes the function $log_{10}(flux+1)$ as its output, where the 1 is added to avoid taking the log of zero, but does not affect the flux value otherwise since flux values typically take on large values $\sim 10^4 - 10^6$ as shown in figure 1. The model is trained using the Nesterov-accelerated Adaptive

Moment Estimation (Nadam) optimizer with default settings in Tensorflow (`https://www.tensorflow.org/api_docs/python/tf/keras/optimizers/Nadam`) to minimize the mean squared error (MSE) of the output. The dropout and early stopping methods are used in the same way in previous studies [*Bortnik et al.*, 2016b, 2018; *Chu et al.*, 2017a,b, 2021].

The whole dataset of electron flux measurements from RBSP A and B (October 2012 - April 2019) was split into three distinct subsets: Part 1: One-year interval between March, 2018 and April, 2019 when the AL and AE indices from the OMNI dataset were not available; Part 2: One-month interval between February 25 and March 25, 2017, when a geomagnetic storm occurred; Part 3: Remaining data. We used Part 3 to train, validate and test the model. Part 1 and Part 2 were only used to evaluate the model's true out-of-sample performance. The Part 3 was further split into 2-day segments. The 2-day segment length was chosen so that it would be much larger than the time resolution of the electron fluxes and input parameters, to ensure that the data samples that are close in time will not be correlated between testing and training sets, and it would be much smaller than the whole period of five years to ensure a large number of time chunks and that target flux data in the testing and training sets were distributed similarly. It is worth noting that in each 2-day interval, both RBSP A and B observations are merged together from the outset and then divided into separate data segments. Therefore, we ensure that the observations of RBSP A and B from the same time intervals will be retained together in either the training or test data set, will never appear in both, in order to avoid data leakage.

The training process of the final model includes two stages: Stage 1: Input parameter selection. In this stage, we use a 5-fold cross-validation method, a subsample of 20% segments are retained as the validation data for testing the model, and the remaining 4 subsamples are used as training data. The cross-validation process is then repeated 5 times, with each of the 5 subsamples used exactly once as the validation data to get the most accurate quantification of the errors. The detailed process of input parameters selection is described in Section 3.3.2; Stage 2: Hyperparameter optimization for best model selection. After we

determine the input parameters, we optimize the hyperparameters to obtain a best final model, with 70% of segments used for the training set, 15% for the validation set and 15% is set side as the test set to evaluate the model performance. The training process uses the training dataset to update the weights and biases, and its performance is assessed on the validation dataset. When the MSE of the validation set stops improving for several steps in a row (8 steps in this study), the training process ends to avoid overfitting and ensure maximum generalizability to unseen data.

3.3.2 Input parameters selection and hyperparameters tuning

Our ANN models can be described as $F_i(\mathbf{X}(t); \mathbf{Q}_{1i}, \mathbf{Q}_{2i}, ..., \mathbf{Q}_{ki})$, where i denotes the energy channel being modeled, k denotes the selected different input indices, and $\mathbf{X}(t)$ represents the position of the spacecraft at the time of observation, using the vector (L, $\sin(MLT)$,$\cos(MLT)$,$MLAT$). The reason for using trigonometric functions for the azimuthal coordinate is to eliminate the discontinuity at $MLT = 0$. The $\mathbf{Q}_{ki}(t, t_{0i}, t_{hi})$ is a time series of time-averaged candidate solar wind parameters or geomagnetic indices with resolution t_{0i} and time history of length t_{hi}. The set of time resolution values t_0 for the 909 keV channel was based on our previous 1.8 MeV model [*Chu et al.*, 2021] and decreasing with energy based on the different characteristic dynamic time scales. The initial t_h is based on the electron lifetime observed by *Claudepierre et al.* [2020a] for different channels and is further tuned in the following step. The feature selection technique utilized here is essentially focused on adding the most informative predictors to the model sequentially [*Kuhn et al.*, 2013] and evaluating its performance. First, We select a 3-hidden-layer neural network model with 500, 100, and 10 neurons respectively, and with 0.2 dropout rate for each layer as a base model. The model size selection is based on our total sample size and previous study experience. We loop through the candidate $\mathbf{Q}$ in Section 3.2.2 as input and evaluate the test performance using group 5-fold cross-validation. After we iterate through all the input parameters $\mathbf{Q}$, we select the time series with best performance (e.g., AL), and then combine

Channel	t_0	Best t_h	$\mathbf{Q}_k$
54 keV	30 min	4 d	AE, SYM-H, Psw, Vsw
235 keV	60 min	10 d	AL, Psw, SYM-H, Vsw
597 keV	90 min	14 d	AL, SYM-H, Psw, Vsw
909 keV	120 min	18 d	AL, SYM-H, Vsw, Psw

Table 3.1: Selected lengths of time history t_h, time resolution t_0 and parameters $\mathbf{Q}_k$ at different channels

that $\mathbf{Q}_{best}$ with another $\mathbf{Q}$ to repeat the iteration process. Finally, we stop the iteration when $k = 4$ for all the channels due to consistency and the test results that improvements of R^2 e.g.,score value at $k = 5$ are small (less than 0.01). The specified parameters $\mathbf{Q}_k$ for each channel are shown in Table 3.1 in decreasing order of importance. The fact that final parameters include solar wind speed (V_{sw}), pressure (P_{sw}), SYM-H and auroral electrojet (AE or AL) index is consistent with our physical understanding of the processes involved and a large number of previous studies [e.g., *Baker et al.*, 1979, 2014; *Wing et al.*, 2016, 2022].

We then studied the model performance at various time periods to discover the ideal length t_h for the time series of input parameters. Figure 3.2 (left) plots the median and standard deviation of the test performance based on the group 5-fold cross-validation, while the right panel shows those of the coefficient of determination, denoted as R^2. The best t_h values determined for each channel are shown in Table **??**. They are considerably longer than the estimated electron lifetime in the outer radiation belt for the corresponding energy [*Claudepierre et al.*, 2020b,a], which suggests that dynamics with time scales smaller than simple decay would be captured in the input time series. After we determined the input parameters, we retrain the models as described in Section 3.3.1 Stage 2. The hyperparameters of the ORIENT-M models, including the number of hidden layers, the number of neurons in each hidden layer and the dropout rates, are optimized using a Tree-structured Parzen

Model structure	Optuna_range	54 keV	235 keV	597 keV	909 keV
num_layers	(3,4)	4	4	4	4
n_units_layer0	(128,512)	291	412	432	428
dropout_rates0	(0.01,0.4)	0.211	0.368	0.011	0.382
n_units_layer1	(4,128)	119	105	114	95
dropout_rates1	(0.01,0.4)	0.385	0.091	0.092	0.075
n_units_layer2	(4,128)	4	116	93	95
n_units_layer3	(4,128)	29	128	12	120

Table 3.2: The Optuna hyperparameter search range and final results for each energy. The 'num layers' represents the number of hidden layers in the fully-connected neural network. The 'n units' stands for the neuron numbers for each layer. The 'dropout ratesx' is the dropout rate for the corresponding layer. The ranges in brackets mean a float number is suggested from min to max for each trial. The final hyperparameters are selected from 200 trials based on results on the validation dataset for each channel.

estimator algorithm [*Bergstra et al.*, 2011, 2013] implemented in Optuna [*Akiba et al.*, 2019]. The final models' structure and Optuna's hyperparameter search space are shown in Table 3.2. We are aware of the limitations that the tuning process of the hyperparameters should be performed at once, including the time-lags of the input parameters, the hyperparameters of the neural networks. However, the number of hyperparameters is so large that the search space of hyperparameters is huge and will require a very large amount of computation power. Therefore, the workflow has been adapted as described above to save computation time.

3.4 Model Evaluation and Results

A popular metric widely used in machine learning is the R^2 score. This indicator is used to quantify the fraction of variance explained by the model. It provides an indication of

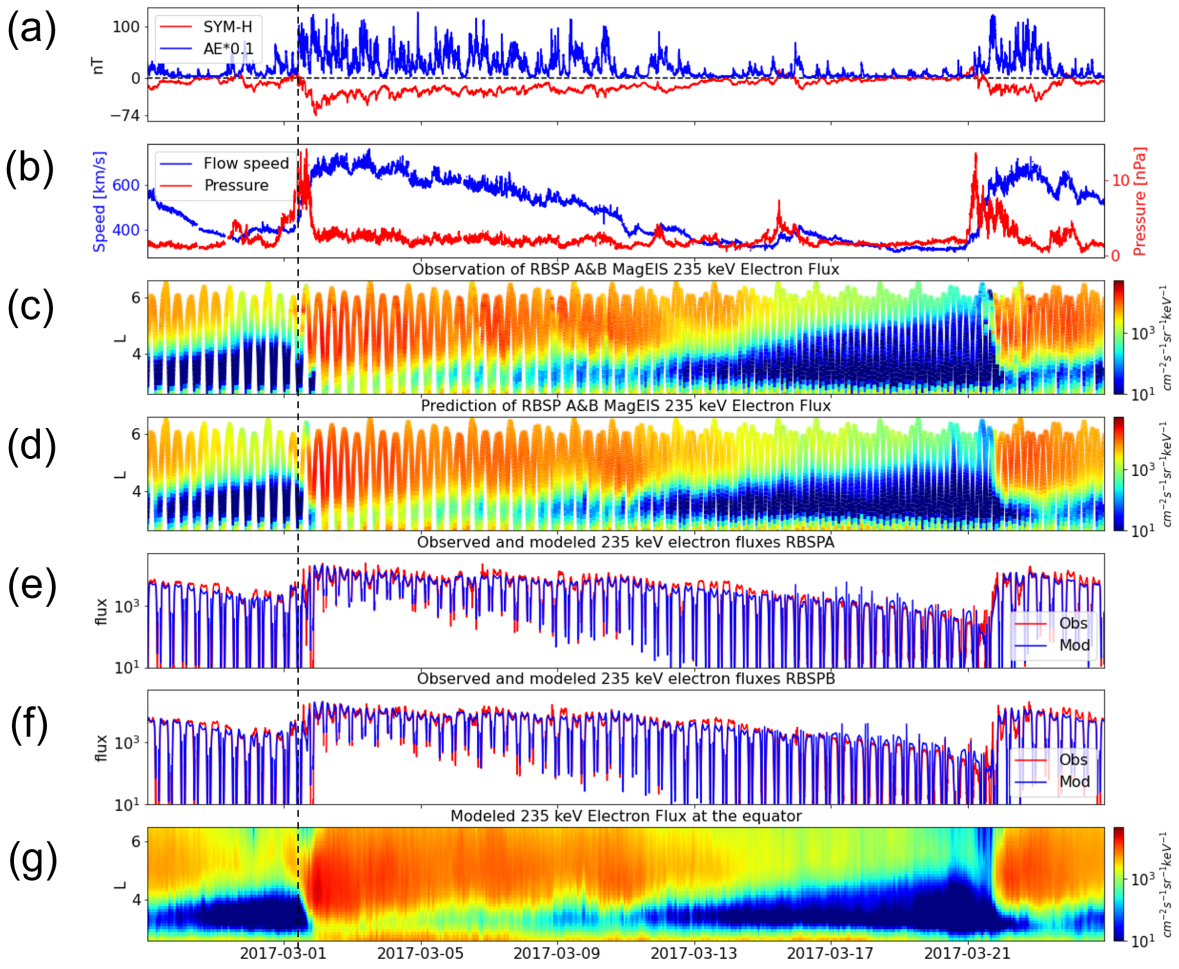

Figure 3.3: An example of the 235 keV model results during the month-long period between February 25, 2017, and March 25, 2017, which was held out from the training set for test purposes. (a) geomagnetic indices SYM-H and AL; (b) The solar wind flow speed (V_{sw}) and dynamic pressure (P_{sw}); (c-d) the observed and modeled 235 keV electron fluxes as a function of L shell and time; (e-f) the observed and modeled 235 keV electron fluxes along the trajectories of Van Allen Probe A and B; (g) the modeled 235 keV electron fluxes on the equatorial plane.

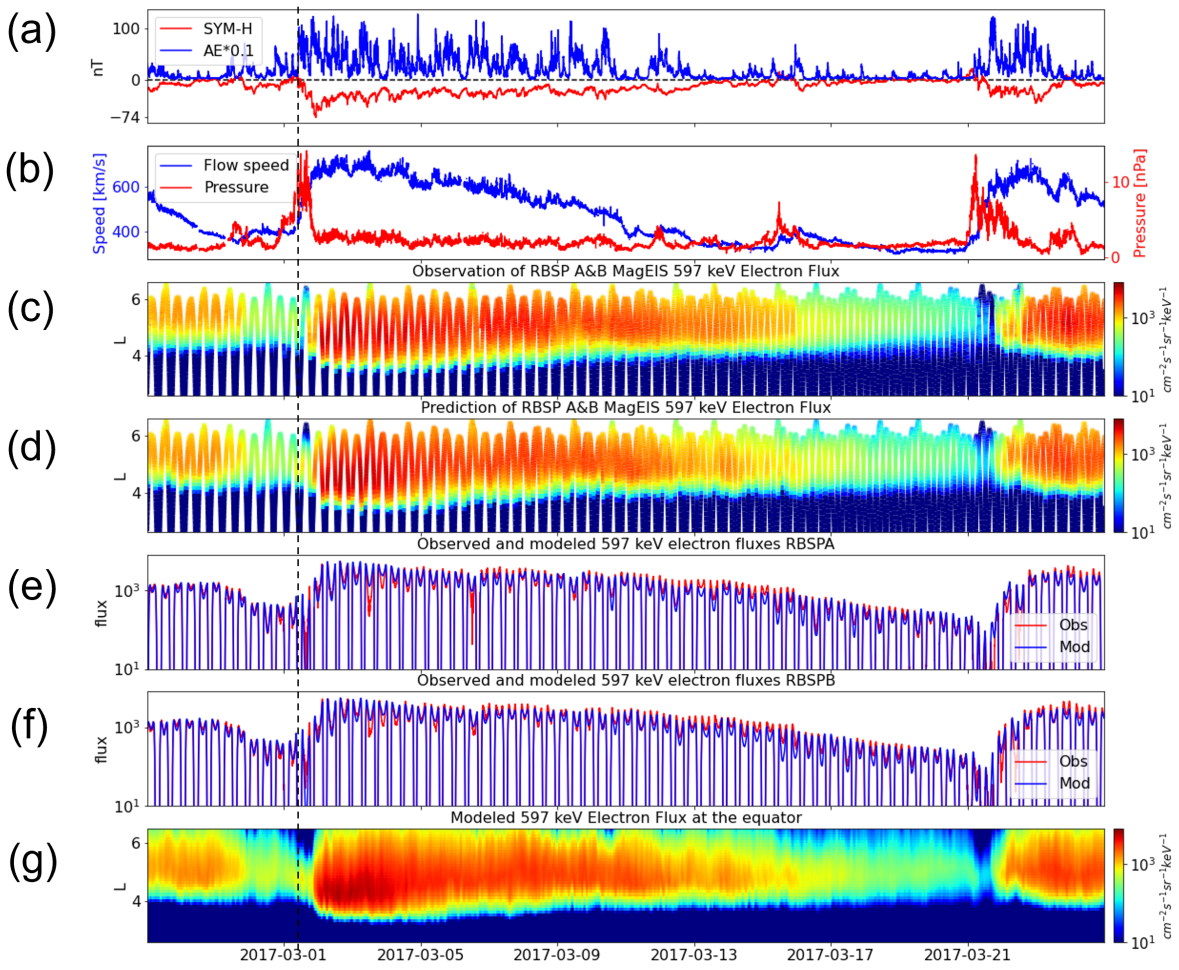

Figure 3.4: Similar to Figure 3.3, but for the 597 keV electron fluxes.

goodness of fit and therefore a measure of how well the unseen samples are likely to be predicted by the model, through the proportion of explained variance. If $\hat{y}$ is the predicted value of the ith sample and y_i is the corresponding true value for total n samples, the estimated R^2 is defined as:

$$R^2(y, \hat{y}) = 1 - \frac{\sum_{i=1}^{n} (y_i - \hat{y}_i)^2}{\sum_{i=1}^{n} (y_i - \bar{y})^2}$$

where $\bar{y} = \frac{1}{n} \sum_{i=1}^{n} y_i$ and this R^2 score is the same with prediction efficiency, PE, described in *Reeves et al.* [2012].

Figure 3.3 and 3.4 show a comparison between the observations and model results for two energy channels (235 and 597 keV) for the out-of-sample one-month period between February 25, 2017, and March 25, 2017, during which a moderate geomagnetic storm (Dst minimum -74 nT) occurred. The geomagnetic indices (SYM-H and AE), the solar wind dynamic pressure (P_{sw}), and solar wind speed (V_{sw}) are shown in panels a and b. A strong interplanetary shock arrived at 9 UT on March 1, 2017, as indicated by the substantial and sudden increase (denoted by the vertical dashed line) in solar wind velocity and solar wind dynamic pressure.

Figure 3.4c, d, and g show the same analysis but for 597 keV electron fluxes. Again, the models are seen to accurately reproduce the general variation of the electron fluxes as well as several key aspects of the general radiation belt behavior, including the effects of physical processes such as rapid local acceleration, radial diffusion, and flux decay. In addition, the comparison of Figure 3.3 and Figure 3.4 clearly shows the capabilities of our model in reconstructing the energy-dependent dynamics of the outer radiation belt.

The analysis in Figure 3.3 and Figure 3.4 shows that each model is able to capture the rapid electron flux enhancement at 2017-03-01 UT and shows excellent agreement in the peak value of the flux and its location. The model-reproduced enhancement first occurs in the 235 keV channel and is later visible in the 597 keV channel, which demonstrates that the low energy seed population is gradually accelerated, most likely due to wave-particle

interactions as has been suggested previously [*Horne et al.*, 2003; *Jaynes et al.*, 2015; *Li et al.*, 2014], consistent with observations.

In addition, at 235 keV, the electron fluxes in this enhancement event are seen to fill the slot region and penetrate into the inner zone, showing that the enhancement of electrons of the inner zone is also well captured. At 597 keV and 909 keV (see Figure 3.10), the electron fluxes do not penetrate into the lower L shells, and the ANN model reproduces the "impenetrable barrier" precisely, implicitly "baking in" all the relevant physical processes into the model that prevent further penetration of these electrons to lower L-shells [*Baker et al.*, 2014; *Reeves et al.*, 2016]. Last, the slow decay of the electron fluxes is well captured. Interestingly, the models successfully reproduce the timing, L-shell, and energy dependence of this decay process. From March 14, the flux decayed more rapidly at $4.0 < L < 4.5$ for the 235 keV channel electrons than it did for 597 keV electrons consistent with previous observations and theoretical estimates of electron lifetimes. Similar features are also observed before March 1 [*Claudepierre et al.*, 2020b,a; *Reeves et al.*, 2016].

Figure 3.3e and 3.3f show the comparison between the observed (red) and modeled electron fluxes along the RBSP-A and RBSP-B trajectories, and a similar analysis is shown for the 597 keV electron fluxes in the Figure 3.4e and 3.4f. Based on this comparison, the overall R^2 value of those two channels for the out-of-sample period are calculated to be 0.91 (235 keV) and 0.96 (597 keV) and the mean-squared error (MSE) between model results and observations are 0.10 (235 keV) and 0.05 (597 keV). The out-of-sample performance metrics are consistent with the performance of Part 3 test dataset analysis shown in Figure 3.5. These results indicate that the models can predict the (sequentially organized) out-of-sample data with a 90% cross-correlation (i.e., variability of the response data around its mean) and a factor of ~ 2 performance in those channels which are comparable to the instrument accuracy. The performance of the 54 keV electron fluxes are not as good as the higher energy channels, as expected due to the complicated and rapid dynamics, as well as consisting of uncorrected data, which may add uncertainty to observed flux values. But the result in

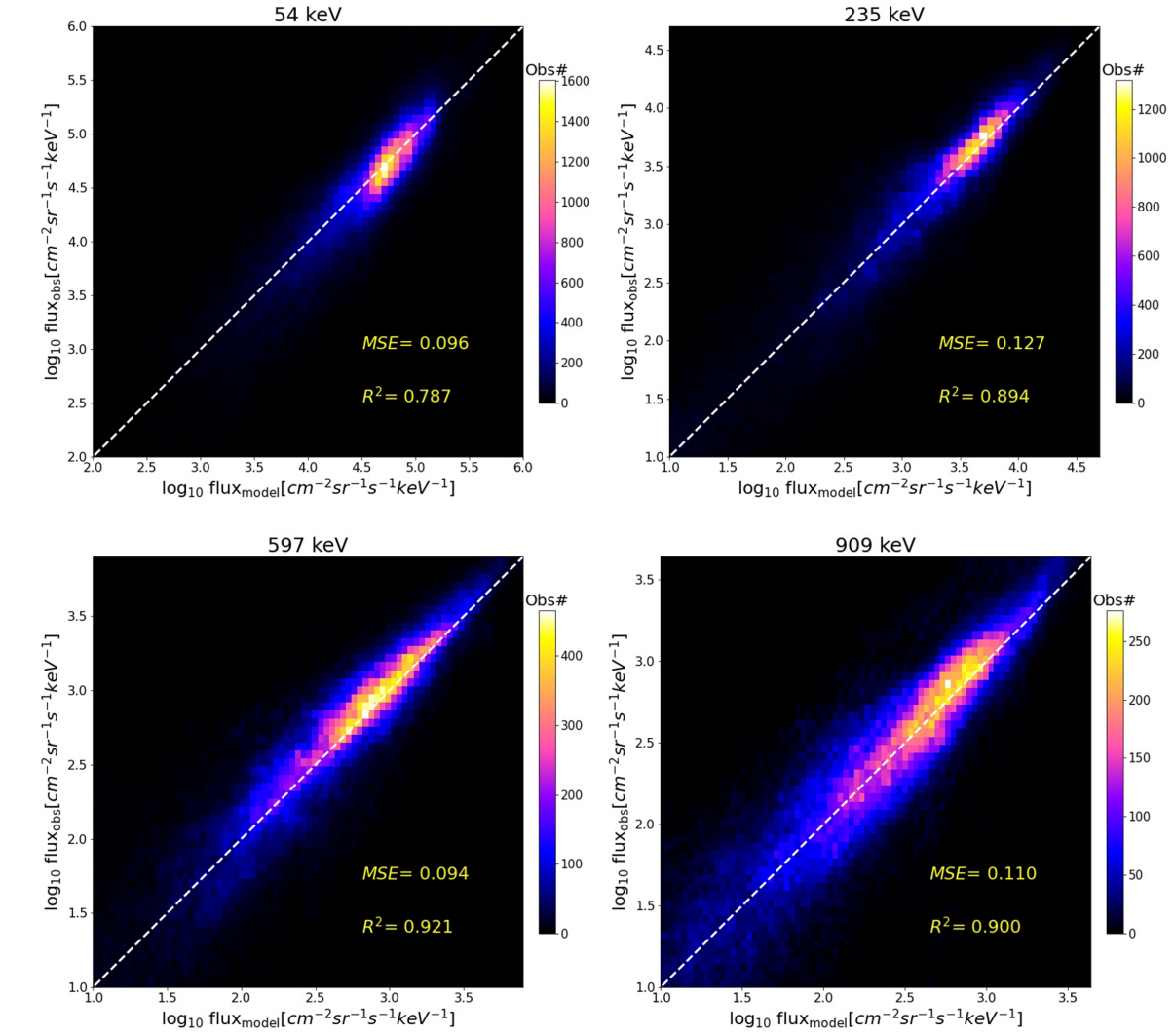

Figure 3.5: Model performance on the test dataset of Part 3 for different electron energy channels, (a-d) test data at 54, 235, 597, and 909 keV. The white dashed lines are diagonal lines that indicate perfect agreement (y=x) between the observations and model results. The coefficient of determination R^2 and MSE are shown at the right bottom corners.

the out-of-sample period and test dataset ($R^2 \sim 0.8$) are still satisfactory and capture the important dynamics (See Figure 3.11).

Figure 3.6 and 3.7 (a - c) show comparisons between the observed and modeled 235 keV and 597 keV electron fluxes along the trajectories of RBSP A and B between March 1, 2018 and April 1, 2019. It is important to note that here we are using predicted AL index since the observed OMNI AL index is not available after March 2018. Because the electron fluxes during this time period were not included in the training process (Section 3.3.2), the comparisons demonstrate the models' out-of-sample predictive ability. The predicted AL index using upstream solar wind measurements is available at `https://lasp.colorado.edu/home/personnel/xinlin.li` [*Li et al.*, 2007a; *Luo et al.*, 2013], which has a linear correlation coefficient of 0.846 and a prediction efficiency of 0.715. The errors, as shown in Figure 3.6c and 3.7c, are defined as the difference between the training target of observed and modeled electron fluxes:$log_{10}(flux_{obs}+1) - log_{10}(flux_{model}+1)$. The results show that our models can reproduce rich dynamics in the fluxes, with rapid enhancements penetrating through the slot region into the inner zone. In particular, the models capture the rapid enhancement and penetration depth during the strong storm on Aug 26, 2018. The R^2 value of those two channels for the out-of-sample period along the orbit are calculated to be 0.80 (235 keV) and 0.87 (597 keV) and the mean-squared error (MSE) between model results and observations are 0.2 (235 keV) and 0.15 (597 keV). We emphasize that the errors originate from both the error in the predicted AL index and from our models. Figure 3.6d and 3.7d show the RBSP-A observations and the ORIENT-M output for $L \sim 5.2$ (select data from $5.1 < L < 5.3$). The R^2 scores between the two are 0.71 (235 keV) and 0.77 (597 keV). One can therefore conclude that the ORIENT-M model generalizes well on the unseen data, both at a fixed L and along the orbit.

The R^2 values of the four channels' test datasets for different L-shells and MLTs are shown in Figure 3.9. It is shown clearly that except the margin regions, our models can produce good results. The 54 keV model performance of the inner zone, which extends to

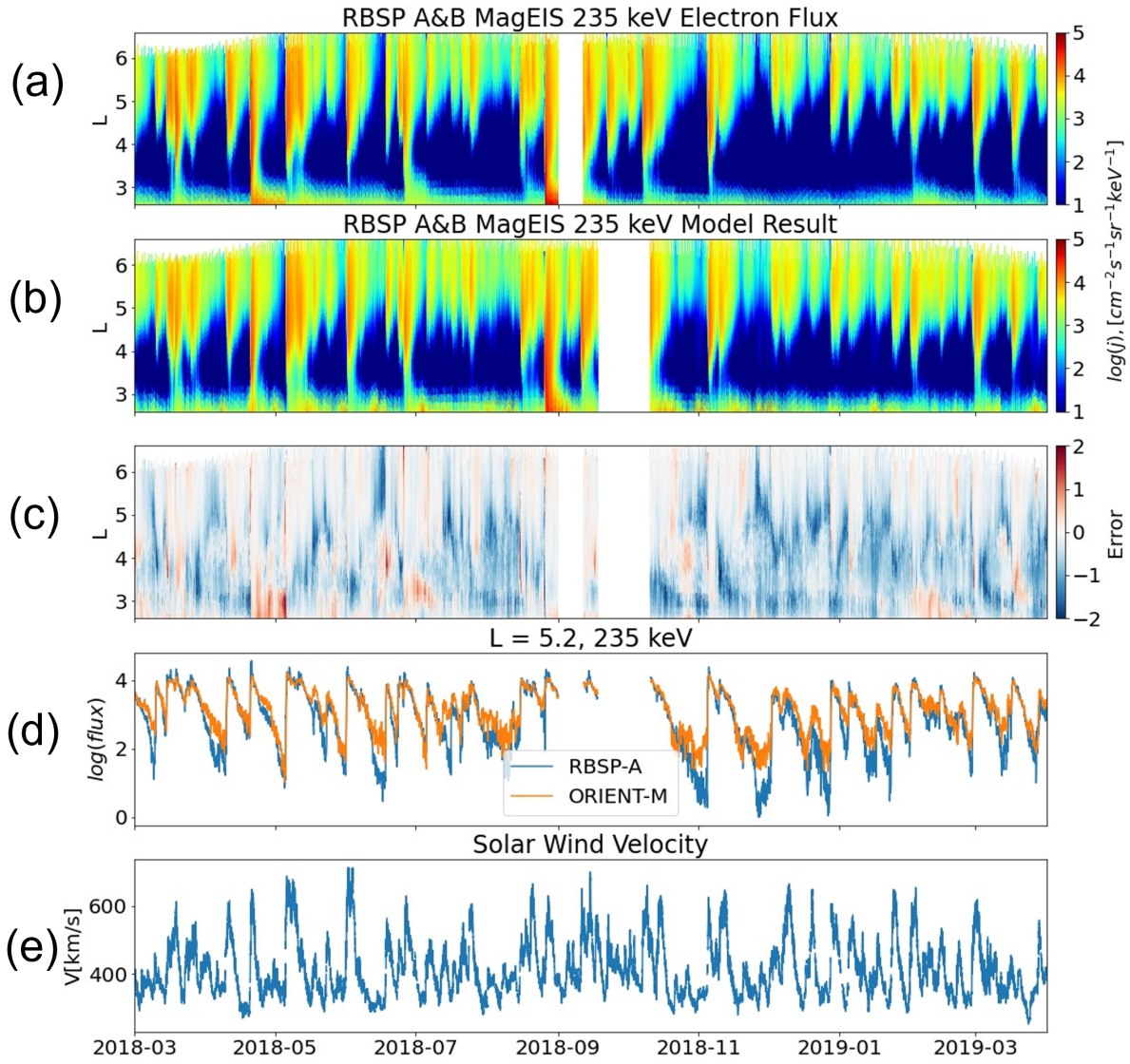

Figure 3.6: Out-of-sample model results produced along the Van Allen Probes' trajectories after March 2018 using the predicted AL index as input while the other inputs are obtained from the OMNI database. (a) The observed 235 keV electron fluxes along the trajectories of Van Allen Probes. (b) The 235 keV model results along the trajectories. (c) The differences between the observed and modeled electron fluxes, which are defined as $log_{10}(flux_{obs}+1) - log_{10}(flux_{model}+1)$. (d) comparison of observed and predicted flux at the fixed L-shell of 5.2 (e) solar wind velocity

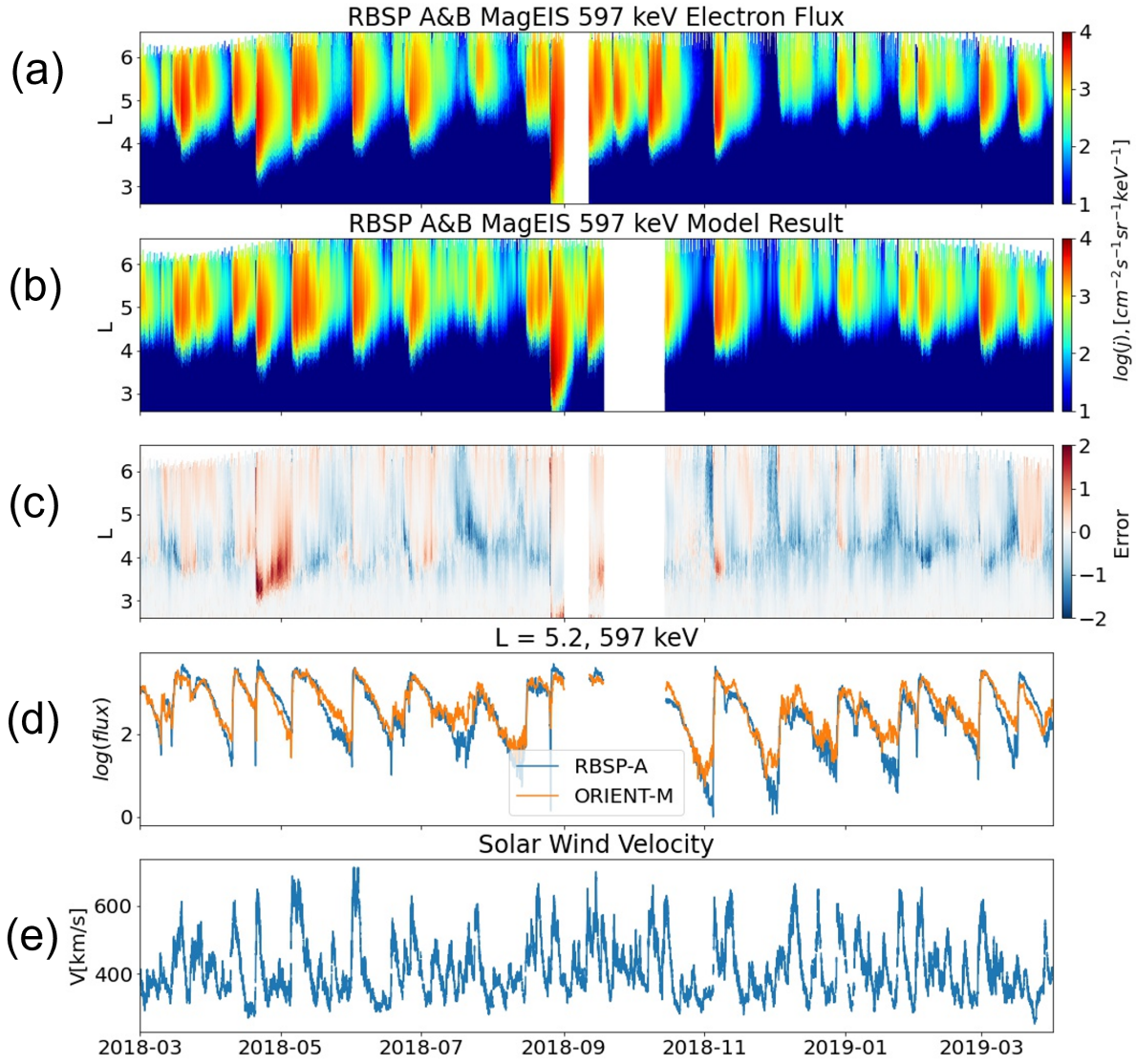

Figure 3.7: Similar to Figure 3.6, but for the 597 keV electron fluxes.

higher L shell for low energy flux, is not as good as the outer zone. A possible explanation may be that the dynamics of inner zone are much less than that of the outer zone and our model cannot capture it accurately. For the regions with low R^2 value of 597 keV ($L \sim 3$, MLT from 6 to 8) and 909 keV ($L \sim 3$, MLT from 4 to 8), the samples in the test dataset are only composed of very low flux measurements ($flux < 10[cm^{-2}sr^{-1}s^{-1}keV^{-1}]$) so that these discrepancies can be negligible.

Since the velocity of the electron drift motion around the Earth is energy-dependent, the global electron distribution following storms and substorms is expected to show an energy-related variation in MLT. This energy-dependent distribution results from a competition of the electron drift period and the loss timescale for that particular energy of electrons. For relativistic electrons (∼MeV), the drift period is very small (tens of minutes) and the loss timescale is large (several days), so the drift motion dominates, and the fluxes are almost symmetrical in MLT about the Earth. However, at lower electron energies (tens to a few hundred keV), the energy-dependent magnetic drifts are far slower, the drift periods are longer, and the loss timescales are shorter, such that the electron fluxes can vary dramatically within a limited range of MLTs.

Figure 3.8 shows the modeled equatorial electron flux distribution variation for 54 keV, 235 keV, and 597 keV (A2, B2, C2) and the corresponding RBSP observations (A1, B1, C1) during a geomagnetic storm that occurred on April 8, 2016. The ORIENT-M model results show the distribution of L-shell and MLT, which exhibit different dynamics for each energy channel. Before the storm (time a), the electron fluxes at each energy channel are seen to be approximately symmetric in MLT. However, when the storm begins (time b), there is an observed enhancement for the 54 keV electrons at the Earth's dawnside consistent with plasmasheet electrons being convected from the tail and drifting Eastwards due to magnetic gradients. In contrast, the higher energy channels exhibit a dropout in fluxes that has a roughly MLT-symmetric distribution. At the peak of the geomagnetic activity (as measured by a minimum in the AL index) the 54 keV electron fluxes (time c) show significant MLT

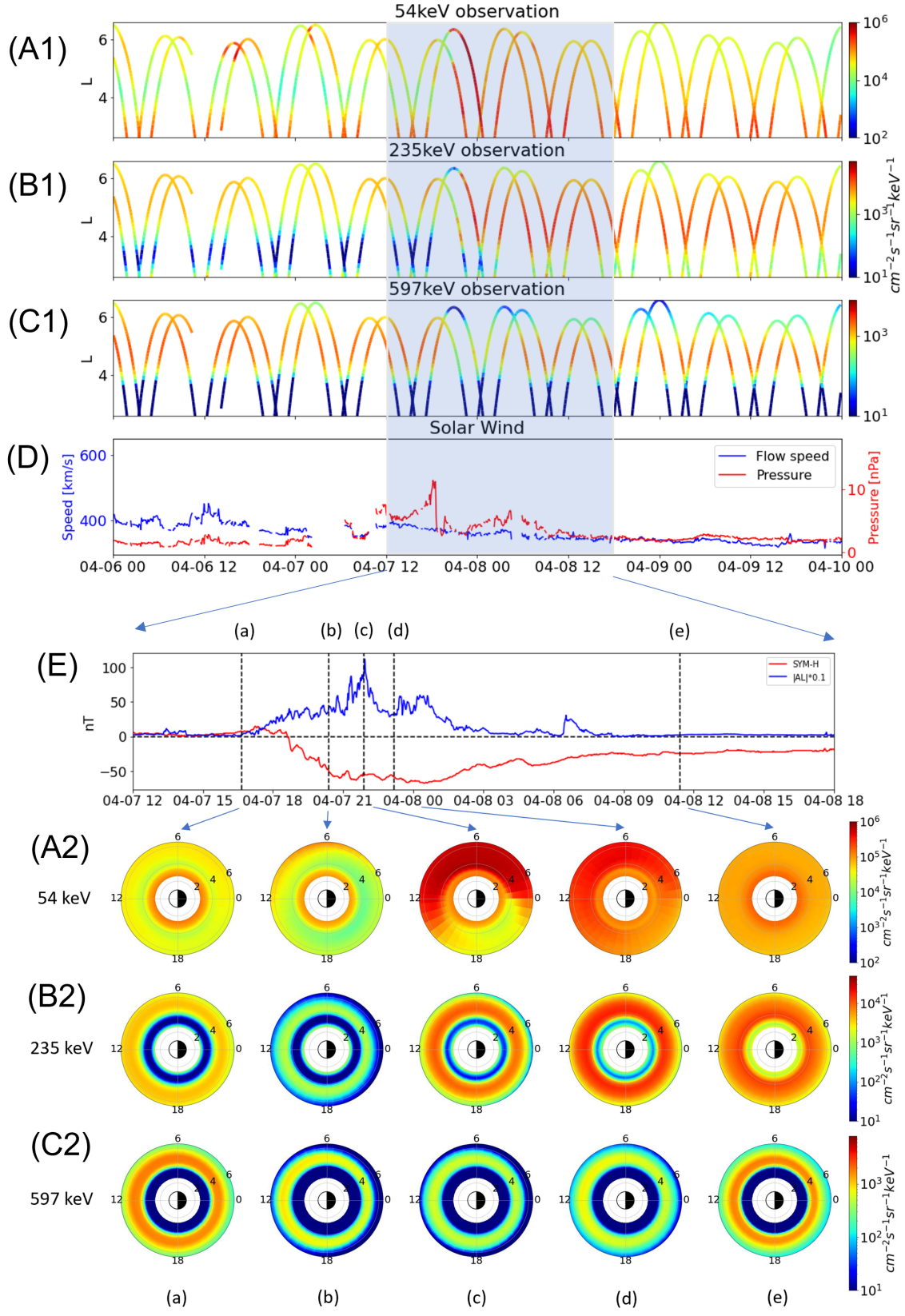
54keV observation
(A1)
235keV observation
(B1)
597keV observation
(C1)
Solar Wind
(D)
Flow speed
Pressure
Speed [km/s]
Pressure [nPa]
04-06 00
04-06 12
04-07 00
04-07 12
04-08 00
04-08 12
04-09 00
04-09 12
04-10 00
(a)
(b)
(c)
(d)
(e)
(E)
SYM-H
|AL|*0.1
nT
04-07 12
04-07 15
04-07 18
04-07 21
04-08 00
04-08 03
04-08 06
04-08 09
04-08 12
04-08 15
04-08 18
(A2)
54 keV
(B2)
235 keV
(C2)
597 keV
L
cm⁻²s⁻¹sr⁻¹keV⁻¹

Figure 3.8: MLT dependence of electron flux. (A1-C1) Observations from 2016-04-06 to 2016-04-10 for 54keV, 235keV and 597keV channel. (D) Solar wind speed and pressure from OMNI. (E) Selected range of SYM-H and AL (2016-04-07/12:00 - 2016-04-08/18:00). (A2-C2) A series of panels showing the model reconstruction of the electron fluxes as a function of L-shell and MLT for different energy channels (54 keV, 235 keV, and 597 keV) at different snapshots in time: (a) 2016-04-07/16:40, in the quiet period before the storm, (b) 2016-04-07/20:25, during the main phase, (c) 2016-04-07/21:55 the time of maximum $|AL|$, (d) 2016-04-07/23:10, early recovery, and (e) 2016-04-08/11:25, the late recovery period after the storm.The top panel shows the SYM-H and AL index during the course of the storm.

asymmetry in the electron flux enhancements, which is observed predominantly at $L \sim 3-6$, and is a reflection of the eastward drift of electrons around the Earth, as well as the rapid loss processes (e.g., scattering by chorus waves) that remove the majority of the enhanced electron fluxes as they drift from the day through to the dusk sectors (See Figure 3.8 54 keV (d). It is worth mentioning that the result of Figure 3.8 cannot be verified at every MLT since we only have two satellites that cannot be everywhere present simultaneously.

The results of localization to the dawnside of the Earth are consistent with a previous study of the same observation, a case study, and statistical distribution result [*Allison et al.*, 2017; *Zhao et al.*, 2017a]. In the early recovery phase of the storm (time d), the enhanced fluxes begin to diminish, and the distribution begins to take on a more MLT-symmetric structure. In the late recovery (time e), the electron distributions in all channels begin to relax back to their pre-storm values. The dropout process might result from the magnetopause shadowing as the dynamic pressure increases. It is interesting to note that the peak flux levels occur at increasingly later times, with increasing electron energies, which is consistent with previous observations [*Thorne et al.*, 2013] and is likely related to the timescales of the local acceleration process. It is worth mentioning that the detailed physics of radiation belt dropouts is still an open problem which we do not aim to address in the present

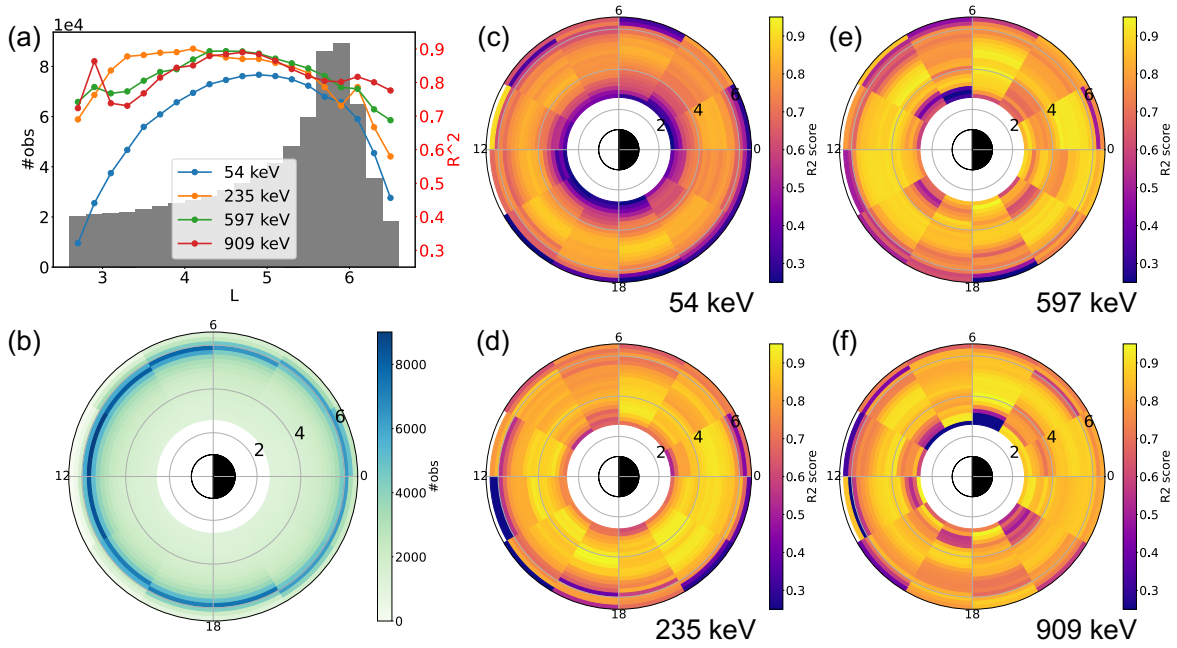

Figure 3.9: R^2 score in the test dataset. (a): R^2 values of test datasets for different L shells. The background gray hist data shows all the data distribution along L shell of 54 keV channel. (b) The training data distribution of 54 keV. (c) -(f): The R^2 values of test dataset as function of L and MLT for different channels. The result includes 20 Lshell bins from $L = 2.6$ to $L = 6.6$ with $\Delta L = 0.2$ and 12 MLT bins with $\Delta MLT = 2$.

study. We can only speculate that since there was a dynamic pressure enhancement when the drop out happened, it is likely that magnetopause shadowing was the main loss process, but interpretation of this physics is not our focus.

Thus, Figure 3.8 and 3.9 show that the ORIENT-M model is able to reconstruct the dynamic evolution of electron fluxes at different energies and capture the L-shell and MLT dependence of both the lower energy fluxes as well as the higher energy fluxes, which is challenging to study using in-situ observations alone.

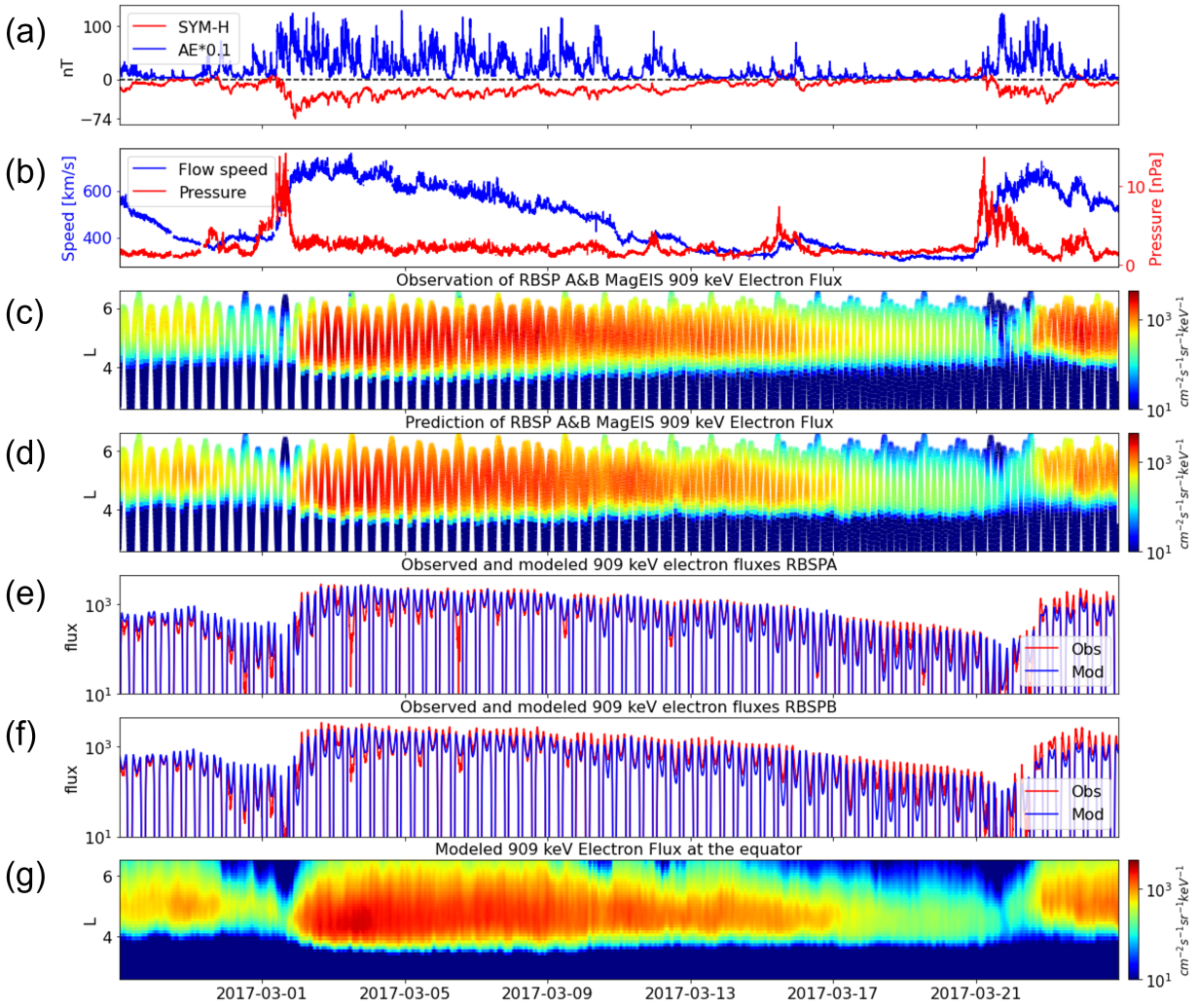

Figure 3.10: Similar to Figure 3.3, but for the 909 keV electron fluxes.

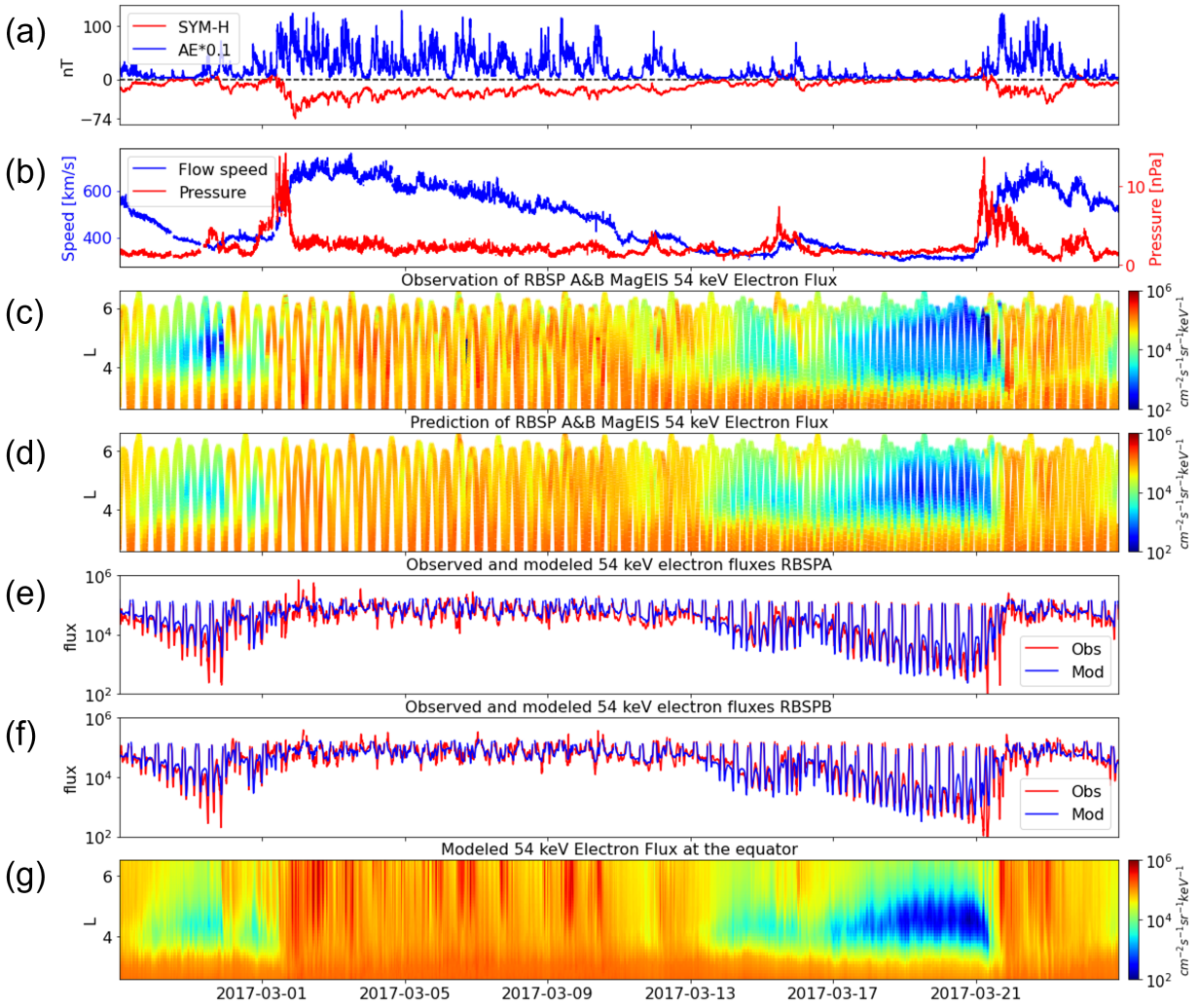

Figure 3.11: Similar to Figure 3.3, but for the 54 keV electron fluxes.

3.5 Summary and discussion

Here, we presented a set of Outer Radiation belt Electron Neural net model for Medium energy electrons (ORIENT-M). The ORIENT-M models are driven purely by a time history of geomagnetic indices and solar wind parameters, meaning that they do not need any other in situ data (e.g., fluxes from LEO satellites) to provide boundary conditions as inputs into the model, and thus our models are able to reconstruct energetic electron fluxes for periods deep in the past and into the future, as long as the geomagnetic indices and solar wind parameters are available. Our models are trained using six years of electron flux data from the MagEIS instrument onboard Van Allen Probes, and we have shown only four representative energy channels in this study. Any predictions of our models for periods in the past or the future are thus essentially a prediction of what the MagEIS instrument on Van Allen Probes should observe under the input conditions provided to the model at that time.

The model performance of the test dataset (which was held out during model training), as well as for complete out-of-sample periods, i.e., a geomagnetic storm in March 2017, was demonstrated and shows a high coefficient of determination ($R^2 \sim 0.7 - 0.9$). The model could reproduce the effects of particle acceleration, decay of the electron fluxes, and energy-dependent dynamics of electron fluxes in the radiation belt. Given its excellent performance in predicting low to high energy electron fluxes, our model was able to capture the MLT-dependent electron flux dynamics. We presented the MLT dependence during a geomagnetic storm that occurred on April 8, 2016. The timing and MLT differences of electron enhancement at 54 keV were well captured by the model, and hence the implication is that the model baked in all the relevant physical processes that shaped the resulting electron distribution. The electron flux asymmetry was seen to be much higher in the dawn sector and the eastward diffusion drift process was reflected in the model result.

The ORIENT-M model presented in this study represents a novel capability in modeling

the subrelativistic (10s to 100s keV) electron flux population. At present, such electron fluxes are studied with either first-principles physics-based numerical modeling [*Jordanova et al.*, 2010; *Li et al.*, 2010], neither of which is able to capture the energy-dependent, dynamical variation of the global distribution of the observations. The present model is aimed at filling this important gap in our modeling capabilities and can be used as an important tool for both space weather (i.e., spacecraft charging) applications, as well as to discern the physical processes that control the dynamics of this key particle population.

CHAPTER 4

Opening the Black Box of the Radiation Belt Machine Learning Model

In this chapter, we discuss how to explain the machine learning model results of radiation belts fluxes and investigate two typical events during the storm and non-storm times. Many Machine Learning (ML) systems, especially deep neural networks, are fundamentally regarded as black boxes since it is difficult to grasp how they function once they have been trained fully. Here, we tackle the issue of the interpretability of a high-accuracy ML model created to model the flux of Earth's radiation belt electrons. The Outer RadIation belt Electron Neural net (ORIENT) model uses only a time history of solar wind conditions and geomagnetic indices as input features. Using the Deep SHAPley additive explanations (DeepSHAP) method, for the first time, we show that the 'black box' ORIENT model can be successfully explained. Two significant electron flux enhancement events observed by Van Allen Probes during the storm interval of 17–18 March 2013 and non–storm interval of 19–20 September 2013 are investigated using the DeepSHAP method. The results show that the feature importance calculated from the purely data-driven ORIENT model identifies physically meaningful behavior consistent with current physical understanding.

4.1 Introduction

In the previous chapter, we tried to solve these shortcomings by presenting an alternative approach to radiation belt modeling using a set of neural network models to reproduce the

radiation belt fluxes. This model, the "Outer RadIation belt Electron Neural neTwork" (ORIENT) model, consists of two sub-models, namely ORIENT-M [*Ma et al.*, 2022] which covers "Medium" ($\sim$ 50 keV$-$1 MeV) energies, and ORIENT-R [*Chu et al.*, 2021] which covers relativistic and ultra-relativistic electron energies ($\sim 1.8 - 7$ MeV). These models are trained on data from the Van Allen Probes [*Mauk et al.*, 2013] MagEIS [*Blake et al.*, 2014] and REPT [*Baker et al.*, 2012] instruments, respectively, and have been extensively tested and validated showing very high accuracy performance for out-of-sample data. Importantly, the ORIENT model successfully captures electron dynamics over long- and short timescales for a range of different energies.

Despite the exciting performance and broad usage of neural network models as we discussed in the previous chapter, the lack of interpretability has been a significant concern resulting from using such black-box models [e.g., *Camporeale*, 2019]. There has been a growing demand for explainable models in the ML community. As a result, explainable artificial intelligence (XAI) has been developed as a subfield of ML to provide results with human-interpretable explanations [e.g., *Lipton*, 2018]. Indeed, several interpretable models have been developed recently for forecasting geomagnetic indices [e.g., *Ayala Solares et al.*, 2016; *Iong et al.*, 2022]. In this paper, we adopt a state-of-the-art feature attribution method called DeepSHAP [*Lundberg and Lee*, 2017], to explain the behavior of the ORIENT model at a representative electron energy of $\sim$ 1 MeV, during a storm time event and a non-storm time event. The remainder of this chapter is organized as follows: Section 4.2 introduces the method of interpreting neural network models used in this study and the general framework to investigate the radiation belt electron flux model. In Section 4.3, we show the feature attribution results for two significant electron flux enhancement events that occurred during the storm time of 17 March 2013 and the non-storm time of 19 September 2013 and interpret the results in the context of our current physical understanding. These events were initially selected by the Geospace Environment Modeling (GEM) focus group "Quantitative Assessment of Radiation Belt Modeling", and have been well discussed by previous studies

[e.g., *Tu et al.*, 2019; *Ma et al.*, 2018]. In Section 4.4, we conclude with a summary of our key findings.

4.2 SHAP method: A model explainer of the black-box machine learning model

As discussed in section 2.3 in general terms, one of the popular and representative methods for machine learning model explanations is the SHapley Additive exPlanation (SHAP) proposed by *Lundberg and Lee* [2017]. SHAP assigns each input feature an importance value (SHAP value) for a specific output and the idea of SHAP is based on the Shapley value [*Shapley*, 1953]. The Shapley value was proposed to determine the fair contribution of an individual player in a game with a coalition of players $\mathcal{F}$. In brief, the Shapley value is calculated by averaging the expected marginal contribution of one player after all potential combinations have been taken into account. One can transpose the Shapley value into explaining to the machine learning model when the players of the cooperating game become the input features and the profit becomes the output. *Lundberg and Lee* [2017] show that the Shapely value is a unique solution that can be applied to the entire class of additive feature attribution methods, and they propose SHAP values as a unified measure of feature importance that various methods approximate. The definition of the additive feature attribution method is:

$$g\left(z'\right) = \phi_0 + \sum_{i=1}^{M} \phi_i z_i' \tag{4.1}$$

Here M is the number of simplified features, ϕ is the feature contribution, $z' \in \{0,1\}^M$ and z' is a binary variable indication whether feature i is present. Notice that this explanation model use simplified inputs x' that map the original input through the local function $x = h_x(x')$ which try to ensure $g\left(z'\right) \approx f\left(h_x\left(z'\right)\right)$ when $z' \approx x'$. The unique solution of the explanation model g that satisfies the desirable property (local accuracy, missingness, and consistency)

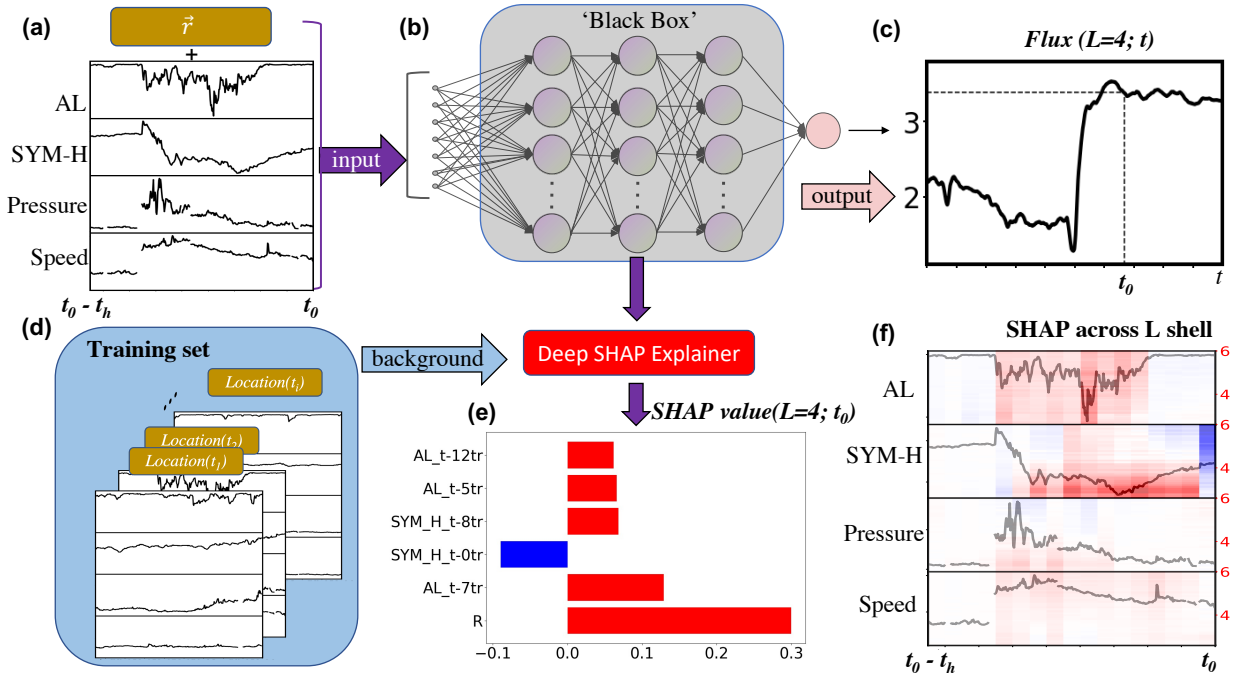

Figure 4.1: Framework used in explaining the feature importance of the ORIENT model. (a) Model inputs including spacecraft location, geomagnetic indices, and solar wind history, (b) propagation through the neural network model to obtain (c) the output, (e) shows how the feature importance is calculated based on (d) the training dataset and the DeepSHAP Explainer, (f) shows how the feature importance value (SHAP) in (d) is now calculated for the fluxes across all the L-shells and superimposed onto the features, blue corresponds to a feature's decreasing effect on the output and red corresponds to an increasing effect.

can be found in Equation 8 in *Lundberg and Lee* [2017]:

$$\phi_i(f,x) = \sum_{z' \subseteq x'} \frac{|z'|!\,(M - |z'| - 1)!}{M!} \left[f_x\left(z'\right) - f_x\left(z' \backslash i\right) \right] \tag{4.2}$$

where the values ϕ_i are exactly the Shapley values and $f_x\left(z'\right) = f\left(h_x\left(z'\right)\right) = f(z_S)$, and S is the set of non-zero indexes in z'. However, it is difficult to calculate the exact Shapely values because most ML models cannot handle arbitrary patterns of missing input values when calculating $f(z_S)$ (i.e. for a given neural network model, we can not remove any input features). To address this issue, $f(z_S)$ is approximated with the conditional expectation $E\left[f(z) \mid z_S\right]$ and the proposed SHAP value is the solution to Equation (3) with such approximation.

The exact computation of SHAP value is still challenging because of the factorial computational complexity which becomes intractable for models with many features. For the deep neural network model, they proposed a method to approximate the SHAP values known as Deep SHAP. This method further approximates $E\left[f(z) \mid z_S\right]$ as $f\left(\left[z_S, E\left[z_{\bar{S}}\right]\right]\right)$ when assuming feature independence and model linearity (Equations 10-12 in Lundberg and Lee (2017)). The interpretation of this assumption is that the missing input feature can be approximated by the average values (expectations) of this feature from the given background samples (i.e. training dataset). Such assumption can be used in Deep SHAP which is a computationally effective method specifically for deep neural network models. Consider a linear model with feature independence as an example: $f(x) = \sum_{j=1}^{M} w_j x_j + b$, the SHAP results are $\phi_0(f,x) = b$ and $\phi_i(f,x) = w_j\left(x_j - E\left[x_j\right]\right)$. Similarly, when assuming the deep model is linear, one can treat each layer as a linear model and the SHAP values can be linearly backpropagated through the network to get the importance of each feature (see Equations 13-16 in *Lundberg and Lee* [2017]). For each data point $\vec{x}$ to be explained, the sum of its SHAP values equals the difference between the model prediction $f(\vec{x})$ and the mean value of model prediction of the background samples:

$$\sum \phi_i = f(\vec{x}) - E(f(\vec{x})) \tag{4.3}$$

where ϕ_i is the SHAP value of the ith feature. Positive (Negative) SHAP value ϕ_i indicates the ith feature has a positive (negative) impact on the output, leading the model to have a higher (lower) output than the average background $E(f(\vec{x}))$. A detailed explanation of Deep SHAP can be found in *Chen et al.* [2021] and *Lundberg and Lee* [2017].

4.3 The explained results from the ORIENT model

4.3.1 Storm time enhancement

Figure 4.2 shows the model and SHAP values of input features for the storm-time radiation belt acceleration event that occurred during 17-19 March 2013. The observed flux of 909 keV electrons is shown in Figure 4.2e as a function of time and L-shell, and the results of the ORIENT-M model on the equatorial plane are shown in Figure 4.2f which successfully capture the initial dropout and following enhancement during the storm. The SHAP values are then calculated for every feature, at every time in the look-back time series, and for the flux value at every L-shell, and shown in Figure 4.2h-w for outputs at four different time snapshots (A-D) as indicated by the vertical dashed lines in Figure 4.2. Figure 4.2g shows the SHAP values as a function of L-shell only. It is worth noting that Figure 4.2h-w are zoomed in to the most recent time history to highlight the storm effect.

The idea of Figure 4.2h-w is that each feature, and indeed each sample in the time series of each feature can contribute to the final flux value in different ways. We see that these can change depending on which phase of the storm, and L-shell the flux value is observed. At time A, before the storm onset, the feature importance of geomagnetic activity and solar wind parameters are all close to zero, indicating that they do not contribute significantly to the flux variation. At time B, a strong dropout event occurs: the SYM-H index gradually decreases to ~ -100 nT accompanied by an AL decrease to ~ -1000 nT. The P_{sw} and V_{sw} were notably enhanced at the same time. Despite the fact that these changes took place simultaneously, they have very different contributions to the output: Changes in AL

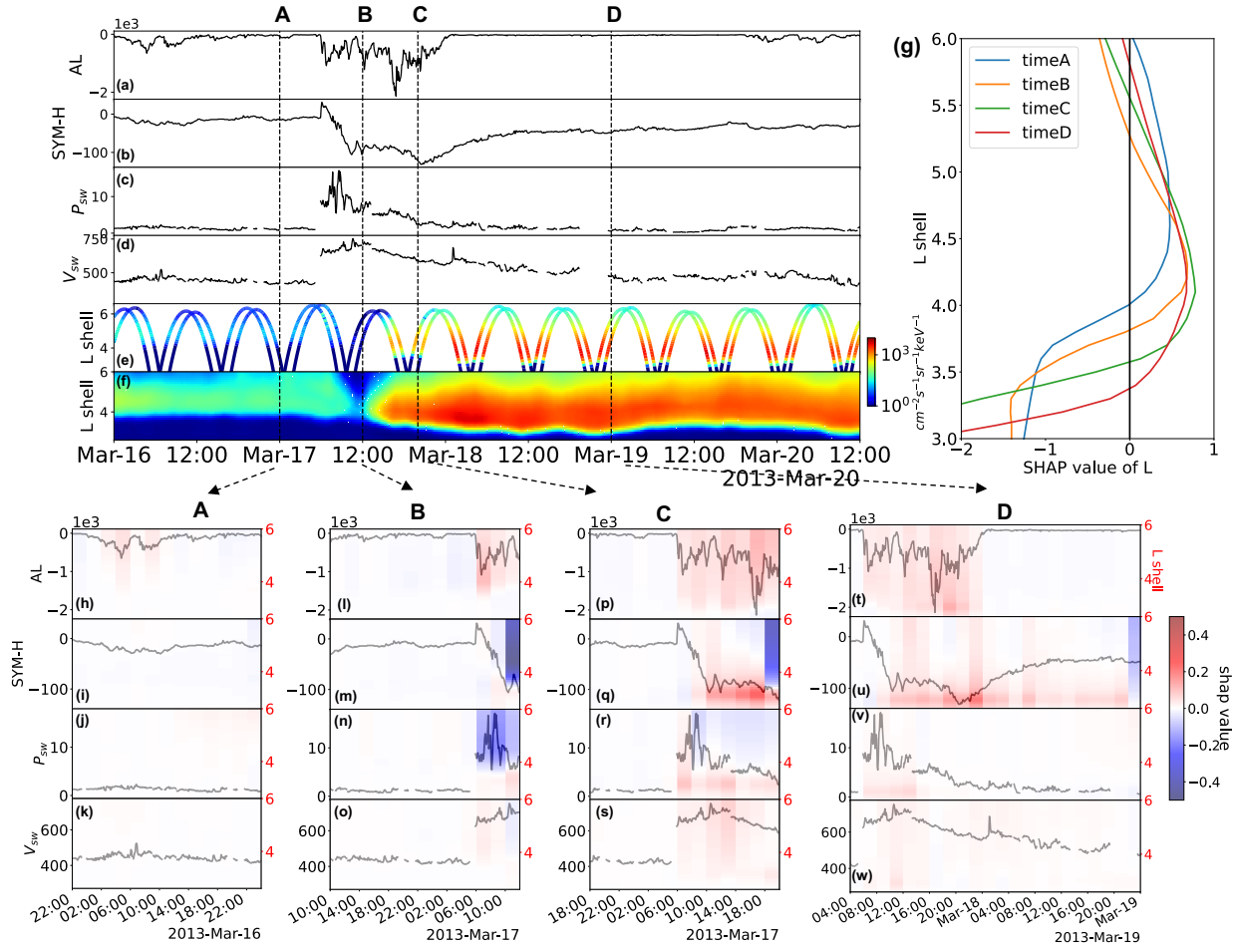

Figure 4.2: ORIENT Model output and feature attribution results for the storm time event of 17 March 2013. Input time series: (a) AL index, (b) SYM-H index, (c) Solar wind dynamic pressure, P_{sw} (d) Solar wind speed, V_{sw} (e) Observed 909 keV electron fluxes as a function of time and L-shell, (f) ORIENT model reconstruction of 909 keV electron fluxes on the equatorial plane, (g) Feature importance based on L-shell, (h)-(k): Color-coded SHAP feature contributions for the model output at time A (2013-Mar-17-0:00) and the corresponding input zoomed in a one-day look-back window, (i)-(o): at time B (2013-Mar-17-12:00), (p)-(s): at time C (2013-Mar-17-20:00), (t)-(w): at time D (2013-Mar-19-0:00) but zoomed in a two-day look-back window.

contribute positively while changes in P_{sw} and SYM-H contribute negatively as shown in Figure 4.2l-n. Thus, the SHAP values indicate that there is a local competition between acceleration and loss of fluxes at $L > 4$. The contributions from the V_{sw} are very close to zero compared with the other three parameters as shown in Figure 4.2o. Interestingly, the feature contributions for the dropout period are only significant at $L > 4$ for time snapshot B.

At time snapshot C, the feature contributions to this enhancement are very different from previous times: The contributions from AL are positive and extend through the whole L range as shown in Figure 4.2p and 4.2t. The contributions from SYM-H are positive at the lower L-shells but the importance closest to time C is negative for the higher L-shells as shown in Figure 4.2q indicating that it contributes to short-term loss at higher L, but long-term acceleration at the lower L-shells. The contributions from P_{sw} are less important compared to time snapshot B. Remarkably, the change of pressure at the same time gives negative contributions at higher L-shell and positive ones at lower L-shells as shown in Figure 4.2r, suggesting that the same parameter can drive different responses at different L-shells at the same time. The feature importance of the solar wind is positive and larger than at time B.

At time D, the contributions from pressure and solar wind are again close to zero as shown in Figure 4.2v and 4.2w. Figure 4.2g demonstrates that the SHAP values as a function of L are always positive at the acceleration region ($L \sim 4 - 4.5$) and negative at lower L-shell, suggesting an ambient, low-level acceleration which is presumably just outside the plasmapause, and an ambient loss outside of $L \sim 6$, presumably due to an outward drift to the magnetopause boundary. Interestingly, the contribution at $L \sim 6$ is around zero at time A but turns negative at time B when the dropout happens, possibly due to enhanced radial outward diffusion [*Shprits et al.*, 2006]. It is also worth noting that the intersection of zero SHAP value and the contributions ($L \sim 4$) moves to the lower L-shells as the storm progresses, suggesting that the plasmapause and acceleration region (due to chorus waves)

moved to lower L-values [e.g., *Thorne et al.*, 2013].

4.3.2 Non-storm time enhancement

Figure 4.3 shows a similar analysis to Figure 4.2 but examines a non-storm time enhancement event that occurred during the period 18-21 September 2013, despite the fact that SYM-H remained higher than -30 nT (which would typically signal a geomagnetically ''quiet' period). The electron fluxes gradually grew near the $5 < L < 6$ region and the ORIENT model successfully reproduced this behavior on the equatorial plane as shown in Figure 4.3e-Figure 4.3f. The enhancement at times B, C, and D exhibit a clear correlation to the peaks in AL with positive SHAP values, and remarkably, the strongest peak where AL~ -1000 nT was found to coincide with the highest feature contributions values (deep reds). In contrast, the period of AL ~ 0 nT gives generally weak negative contributions to the fluxes as shown in Figure 4.3l, p, and t. Interestingly, the positive SYM-H in the last 2-hour window of time A gives positive contributions to the flux, and at times B and C, they give negative contributions. The reason for these contradictory results is not clear and needs further investigation. Figure 4.3g demonstrates that the contribution from higher L-shells becomes gradually enhanced from time A to time D. Interestingly, the intersection of zero SHAP value and contributions around $L \sim 4.3$ does not move which is a very different response than that observed in the storm time event (Figure 4.2). The summed SHAP values of each Q and the SHAP of L are shown in Figure 4.4f (for $L = 5.2$) and h (for $L = 3.2$). For the high L-shell case, it is seen clearly that there was a sudden enhancement in the AL contribution which results in a major increase in flux as shown in Figure 4.4f. For the low L-shell case, the contributions are much less significant than at the high L-shell since the fluxes are extremely low throughout the time interval displayed.

The acceleration occuring during the non-storm time enhancement has been discussed in previous studies [*Schiller et al.*, 2014; *Su et al.*, 2014]. By performing 3D radiation belt simulations, *Ma et al.* [2018] showed that radial diffusion by ultra low-frequency waves plays a

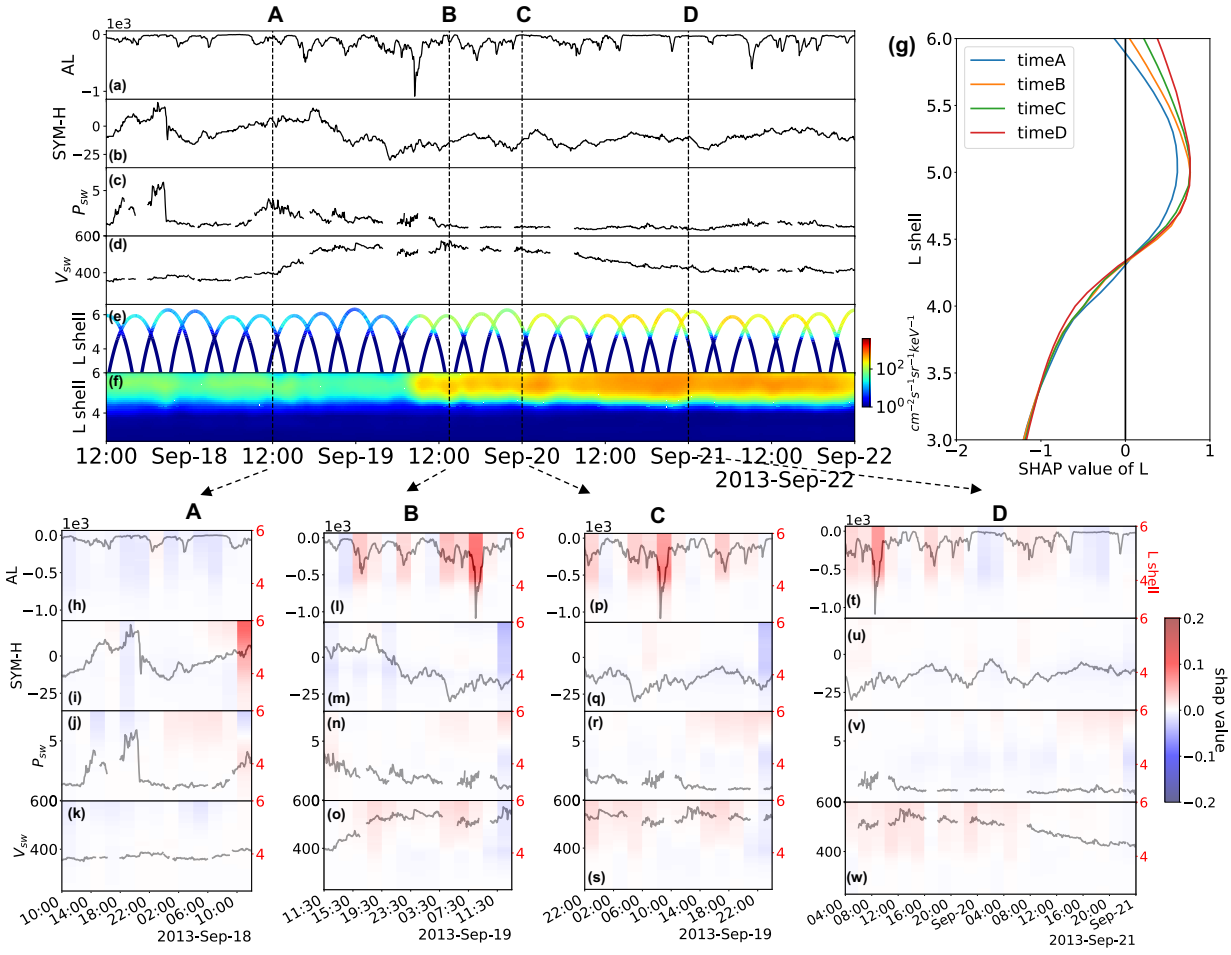

Figure 4.3: Similar analysis to Figure 4.2 but for a contrasting non-storm time radiation belt acceleration event, the selected times A: 2013-Sep-18-12:00, B: 2013-Sep-19-13:30, C: 2013-Sep-20-0:00 and D: 2013-Sep-21-0:00. Results show the direct influence of injection activity (as proxied by the AL index) on the flux enhancement.

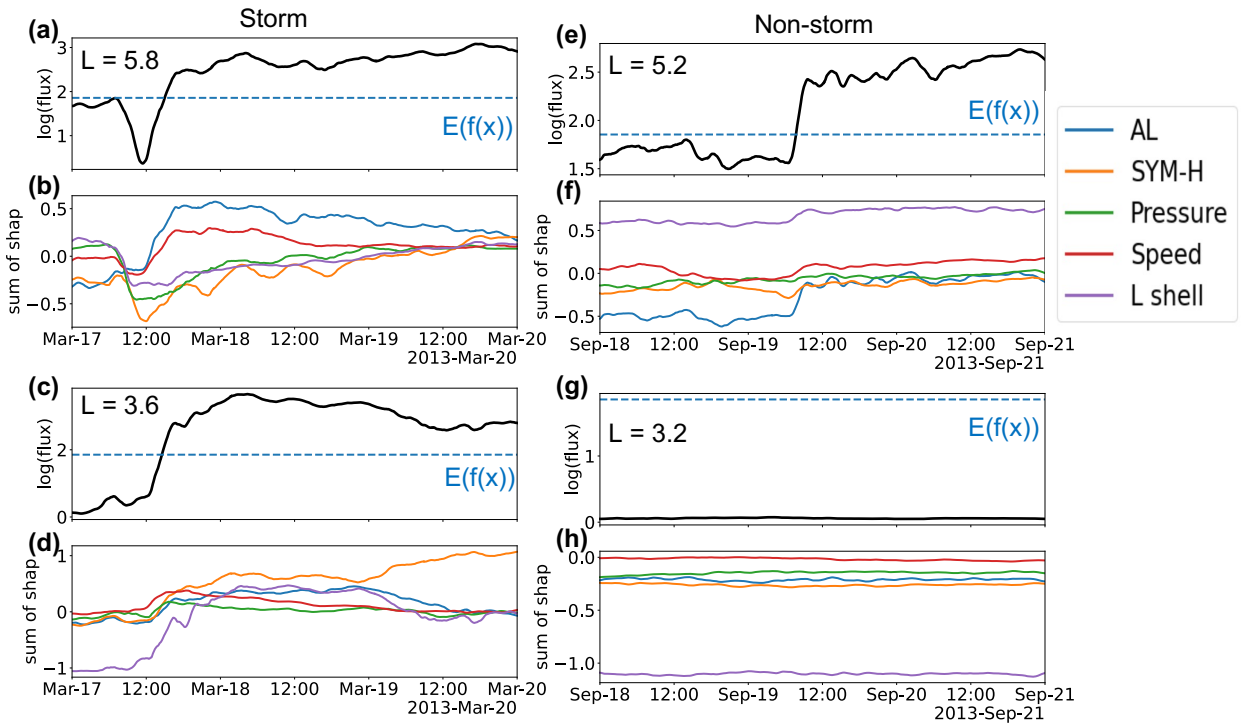

Figure 4.4: Model results at specific L-shell and the sum of SHAP value for each parameter. (a) Storm time model result at $L = 5.8$, blue dashed line is the baseline value $E(f) = 1.854$ which is the average output of selected background samples. (b) At $L = 5.8$, the sum of SHAP values of AL, SYM-H, Pressure, and Speed, and the SHAP value of L-shell as a function of time. (c)-(d) Same as (a)-(b) at $L = 3.6$. (e-f) Same as (a)-(d) at $L = 5.2$ and $L = 3.2$ for non-storm time.

dominant role in this enhancement. However, none of these studies made a direct connection between the acceleration event and substorm activity. Here, we show clear evidence that this non-storm time enhancement is related to the substorm activity. Along with the result of the storm time event, the feature attribution method shows that the substorm injection process may contribute to the acceleration of electron flux, which is consistent with the acceleration scenario presented in *Jaynes et al.* [2015].

The SHAP technique is an additive feature attribution method, meaning that the contributions for each value of Q could be added over the look-back window to compare their total contributions to the flux during this storm time event. This is illustrated in Figure 4.4 for two events and two L-shells in each event. Figure 4.4a shows the March 2017 storm described above, giving the modeled flux at a relatively high L-shell ($L = 5.8$) and 4b shows the sum of SHAP values for each Q together with the SHAP value of L-shell as a function of time. Figure 4.4c and d show the same results but for $L = 3.6$. For high L-shell, as the storm progresses, the SYM-H and P_{sw} firstly give negative contributions to the output, and then recover to zero while the V_{sw} and AL have positive contributions. At the dropout time around March 17-12:00, the negative contribution from SYM-H, P_{sw}, and L dominate. For low L-shell, the SYM-H and P_{sw} both try to enhance the flux at first, but the positive feature contribution from pressure quickly recovers to zero while the contribution from SYM-H is found to be predominantly rising. The contribution from AL also rises but is less than SYM-H at the lower L-shell. Interestingly, at the end of the storm (March 20), the contribution to low L-shell enhancement is dominated only by the SYM-H index. The fact that the intersection in Figure 4.2g moves downward to the lower L-shell during the storm also plays an important role in the flux enhancement, which is indicated by the enhancement of SHAP value from the L-shell as shown in Figure 4.4d.

The feature attribution results are in consistent with our physical understanding and previous studies during this storm time event [e.g., *Turner et al.*, 2013; *Ma et al.*, 2018]. The dayside magnetopause causes trapped electrons to escape to the system's outer boundary

through magnetopause shadowing [*Ukhorskiy et al.*, 2006] and occurs as a result of the magnetopause moving suddenly inward in reaction to increased solar wind dynamic pressure. The subsequent enhanced outward radial transport by enhanced ultra-low frequency wave activity can facilitate the sudden dropouts of electrons [*Shprits et al.*, 2006]. Similarly, our feature attribution results show that the increased pressure during the storm intends to drastically reduce the flux, but at only a high L-shell. Furthermore, simultaneous changes in AL and SYM-H lead to very different outcomes. The cluster of AL peaks always contributes to the acceleration of fluxes at higher L-shell while the main phase of SYM-H contributes to the dropout at higher L-shell and enhancement at lower L-shell, possibly due to the so-called 'Dst effect' [*Kim and Chan*, 1997]. The ring current alters the magnetic field and electrons moved radially outward (inward) to conserve their third adiabatic invariant, their fluxes decrease (increase) for fixed energy as their first invariant is also conserved. One of the difficulties in analyzing geoeffectiveness during storms is that all the responses happen simultaneously and the driver is a combination of different effects. Thus, with the feature attribution method introduced here, we can quantitatively analyze and unravel the contributions from different inputs to the system.

4.4 Summary and discussion

The traditional approach to understanding energetic electron fluxes in Earth's radiation belt is to use Fokker-Planck simulations with assumed boundary conditions (typically guided by observations) and different, highly parameterized diffusion coefficients. This approach has several limitations, as outlined in the introduction section. In this study, we use a recently developed neural network 'ORIENT' model with inputs that include the time history of geomagnetic indices and solar wind parameters. Although the ORIENT model results show high accuracy and can capture the electron dynamics across the energy range (10s keV to several MeV) over long- and short-time scales, the neural network is nevertheless a 'black

box' model. The interpretability of such models is an important issue that needs to be addressed and is of interest to all physicists. Here, we apply the feature attribution method based on the DeepSHAP technique to our ORIENT-M model at representative energy (909 keV) and demonstrate the general flow of opening the 'black box' of radiation belt (and similar) ML models.

With the proposed framework, we analyze two GEM-challenge enhancement events on 18 March 2013 (storm time) and 19 September 2013 (non-storm time). The DeepSHAP method successfully and quantitatively revealed the feature attribution for the different inputs. For the storm time event, the strong enhancement of solar wind pressure contributed to the rapid dropout seen at higher L-shells, which is consistent with the magnetopause shadowing effect and outward radial diffusion process. The acceleration of electron fluxes at higher L-shells was contributed dominantly by clusters of AL peaks while at lower L-shell, the acceleration was mainly contributed by the SYM-H index. The rapid decrease of the SYM-H index also contributed to the dropout at high L-shell during storm time. Different contributions to the fluxes from SYM-H at high and low L-shell were seen to be consistent with the well-known 'Dst effect'. Regarding the non-storm time event, the acceleration was found to be clearly correlated to the substorm injection process. These findings, which are consistent with current physical understanding, not only demonstrate the reliability of the interpretation method, but its potential to help the discovery of missing physical processes. Additionally, the analysis presented in this chapter demonstrates not only the accuracy of our ML model but most importantly that most of the physical processes are captured in the training of the ORIENT model. Our study thus provides the framework and encouragement for a new way to model and explain radiation belt dynamics and other similar ML models. For a trustable machine learning model which predicts a physical quantity, we need to make predictions in a physically consistent manner. However, it is hard to tell just from the matrix, such as mean-square error or correlation coefficient calculated from years of data, that the model is good enough. In this paper, we demonstrate that with the proposed SHAP framework, the

notable physical process revealed by our previous machine learning model is consistent with our physical understanding.

There are many other explanation methods available to compute feature importance for any black box model such as the Local Interpretable Model-Agnostic Explanations (LIME) [*Ribeiro et al.*, 2016] and the Integrated Gradient [*Sundararajan et al.*, 2017] methods, among others. Many of these types of methods define some baseline of missingness which is the key to interpretability because we always want to know if a feature is missing, what would be the effect on the output. We did not discuss the uncertainty of SHAP since we use a large number of background samples ($\sim 100,000$) to model the missingness and the value would converge to the SHAP values. The uncertainty mostly comes from the model itself. Since the events we selected are not in the out-of-sample dataset, there could be differences when explaining individual samples in an over-fitted model between the training and test datasets. So, a well-trained model with a high accuracy should always be prioritized. One can bootstrap the training dataset with sampling and train the model on every bootstrap and then estimate the SHAP value to achieve the confidence level. This topic is fairly technical and the advantages and disadvantages need to be carefully considered, so it is reserved for future work. However, caution should be exercised when using feature attribution techniques like SHAP. The DeepSHAP and other methods usually assume feature independence so this property not only requires us to develop highly accurate models but also to choose input features with care. Fortunately, we chose input features based on the strategy of adding the most informative predictors sequentially when building ORIENT model. This strategy helps in avoiding features with high co-linearity such as AL and AE. Another important problem is that since we assume the independence of each feature, the hidden interaction between geomagnetic indices and solar wind parameters is ignored. One potential solution is using tree-like models when building the machine learning model, and the SHAP methodology is able to handle the tree-like model with the global interpretation and feature interaction, which is a topic to be investigated in future studies.

CHAPTER 5

Machine Learning Interpretability of Outer Radiation Belt Enhancement & Depletion Events

In this chapter, we investigate the response of outer radiation belt electron fluxes to different solar wind and geomagnetic indices using an interpretable machine learning (ML) method. We reconstruct the electron flux variation during 19 enhancement and 7 depletion events and demonstrate the feature attribution analysis called SHAP (SHapley Additive exPlanations) on the superposed epoch results for the first time. We find that the intensity and duration of the substorm sequence following an initial dropout determine the overall enhancement or depletion of electron fluxes, while the solar wind pressure drives the initial dropout in both types of events. Further statistical results from a dataset with 71 events confirm this and show a significant correlation between the resulting flux levels and the average AL index, indicating that the observed "depletion" event can be more accurately described as a "non-enhancement" event. We thus demonstrate that our novel SHAP-Enhanced Superposed Epoch Analysis (SHESEA) method can be used as an insight discovery tool in various physical systems.

5.1 Introduction

A number of previous studies have demonstrated that geomagnetic storms can result in either an increase or a decrease of the fluxes of relativistic electrons in the outer radiation belt. *Reeves et al.* [2003] examined 276 storms from 1989 to 2000 revealing that approximately

half of the geomagnetic storms resulted in increased radiation belt electron fluxes, roughly a quarter resulted in decreased fluxes and a quarter were roughly unchanged. *Turner et al.* [2013] analyzed the electron phase space density (PSD) of 53 storms with main phase minimum Dst < -40 nT, revealing that 58% of the storms resulted in relativistic electron PSD enhancement, 17% resulted in depletion, and the rest remained unchanged. These studies primarily focused on geomagnetic storm times, identified with a threshold set by the SYM-H index. *Katsavrias et al.* [2019] employed a superposed epoch analysis to investigate flux changes during geospace disturbances by combining both storm and non-storm events.

Despite significantly advancing our understanding of radiation belt dynamics, these studies contain certain limitations. Particularly, these studies have faced challenges in delineating the relative importance of different driving factors that occur simultaneously. Their findings are primarily based on statistical results only and cannot reproduce the processes observed in the satellite data with the identified drivers.

In this chapter, we employ the same interpretable machine learning (ML) method used in Chapter 4 in conjunction with a superposed epoch analysis to investigate the enhancement and depletion events of relativistic electrons in the outer radiation belt. Section 5.2 introduces the methodology, Section 5.3 presents the results, and our conclusions are discussed and summarized in Section 5.4.

5.2 Method: SHAP-Enhanced Superposed Epoch Analysis (SHESEA)

In this study, we utilize an ML model that is trained on relativistic electron flux data, specifically the 909 keV channel, from the Magnetic Electron Ion Spectrometer (MagEIS) instrument [*Blake et al.*, 2014] aboard the Van Allen Probes [*Mauk et al.*, 2014]. This model has demonstrated remarkable accuracy when tested with out-of-sample data, giving $R^2 \sim 0.78 - 0.92$ [*Ma et al.*, 2022]. In *Ma et al.* [2023], the authors implemented the SHAP method

to provide insight into the workings of the ML model using 2-hour average values of AL, SYM-H, Psw, and solar wind speed Vsw as inputs. For each input data point $\vec{x}$ to be explained, the sum of the SHAP values corresponds to the difference between the model prediction and the average prediction of the model for only background samples:$\sum \phi_i = f(\vec{x}) - E(f(\vec{x}))$ where ϕ_i is the SHAP value of the i th feature. Positive (Negative) SHAP value ϕ_i indicates that the feature has a positive (negative) impact on the output value.

Figure 5.1 shows examples of a typical acceleration (left panels) and depletion (right panels) event, with color-coded SHAP values superimposed on each of the corresponding inputs in Figures 5.1a-d and 5.1g-j. In each of these panels, the y-axis on the right side of the panel indicates the particular L-shell at which the output fluxes are being affected by the current feature, in accordance with the SHAP value displayed in color. In each event, the times at which the output fluxes to be explained are indicated by the vertical dashed lines. For the enhancement event, it is seen that the cluster of AL peaks occurring at $\sim$ 0600 –2300 UT on 17 March 2013 dominantly contributes to the acceleration of fluxes across a broad range of L-shells from $\sim$ 3–6, while the main phase and minimum of SYM-H contribute to the enhancement at lower L-shells around 3.5. For the depletion event shown in the right column, although the strong peaks in the AL index occurring before 13 September 2014 show positive SHAP values (i.e., causing flux enhancements at L $>$ 4), the following low intensity, continuous AL indices after 13 September 2014 and pressure enhancement occurring around 1500UT on 12 September 2014 show negative contributions to the flux at high L shells (L $>$ 4) which ultimately lead to a depletion of the fluxes after 13 September 2014.

The events selected in *Katsavrias et al.* [2019] consist of 71 intervals during the RBSP era which satisfied a set of specific conditions from at least 12 hours before each event starts: the average solar wind speed must be below 400 km/s, and pressure must be under 3 nPa; the geomagnetic SYM-H index must be consistently over -20 nT, the AL index above -300 nT, and Bz between -5 and 5 nT. The end time of the event is taken to be the time when all parameters revert to their pre-event levels. The authors then select 20 enhancement and 8

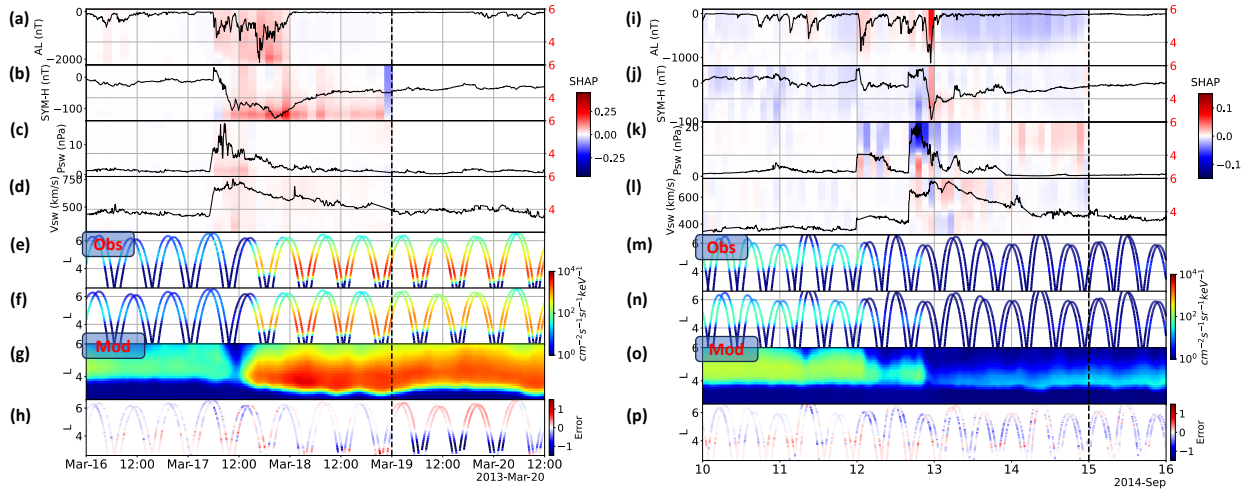

Figure 5.1: Van Allen Probes observation, ML model and SHAP results of enhancement and depletion events. Left column: Enhancement event of 17 March 2013, input time series of the ML model:(a) AL index, (b) SYM-H index, (c) solar wind dynamic pressure, Psw, (d) solar wind speed, Vsw, (a-d) together with color-coded SHAP feature contributions for the model output at time 00 UT on 19 March 2013. (e) Observed 909 keV electron fluxes as a function of time and L-shell. (f) model reconstruction along the trajectories. (g) model reconstruction of 909 keV electron fluxes on the equatorial plane. (h) The differences between the observed and modeled electron fluxes, which are defined as log10(fluxmod + 1) - log10(fluxobs + 1). Right column: same as (a-h) for the depletion event of 13 September 2014. The SHAP results are input feature contributions for output at time 00 UT on 15 September 2014, across all L shells.

depletion events from these 71 events for their superposed epoch analysis method. The events we use in the present study are the same as the *Katsavrias et al.* [2019] dataset described above, except for 1 enhancement and 1 depletion event in December 2013 where the gap in solar wind data was too large for us to reasonably interpolate in order to reproduce the required ML output for our SHAP method. Another slight difference is that we define the t_0 epoch as the time of maximum dynamic pressure of the solar wind instead of the time of the maximum compression of the magnetopause. In addition to the standard superposed epoch analysis that was used in the above study, here we calculate the SHAP value of each feature for each event, for the output fluxes at three different times: $t_0 + 5h$, $t_0 + 1d$ and $t_0 + 2d$, in order to gain insight into how each feature controls the output. The SHAP "enhanced" superposed epoch analysis (SHESEA) is colored with the median SHAP values of the input parameters for all the events, in order to identify the ML interpretation results as a function of storm phase, L-shell, and event type. We also calculate the ML output flux of each event and show the median flux results.

5.3 Results: The factor controling depletion and enhancement events

Figure 5.2 shows the results corresponding to the 19 enhancement events. Panels 5.2a to 5.2d show the time series of each of the inputs and the superposed results for AL, SYM-H, Psw, and Vsw displaying the median in black, and upper and lower quartiles in red. The median flux from the ML model in Figure 5.2e shows that the minimum flux level occurs roughly at $t_0 + 5h$ as indicated by the third vertical dashed line, following the dropout. The median SHAP results of the flux at $t_0 + 5h$ are colored-coded and superimposed on the input time series in the upper four panels of each column. It is clearly recognized that the negative contribution to the output flux comes mainly from the Psw maximum (Figure 5.2c) at around t_0, and SYM-H (Figure 5.2b) closer to the time of the observation

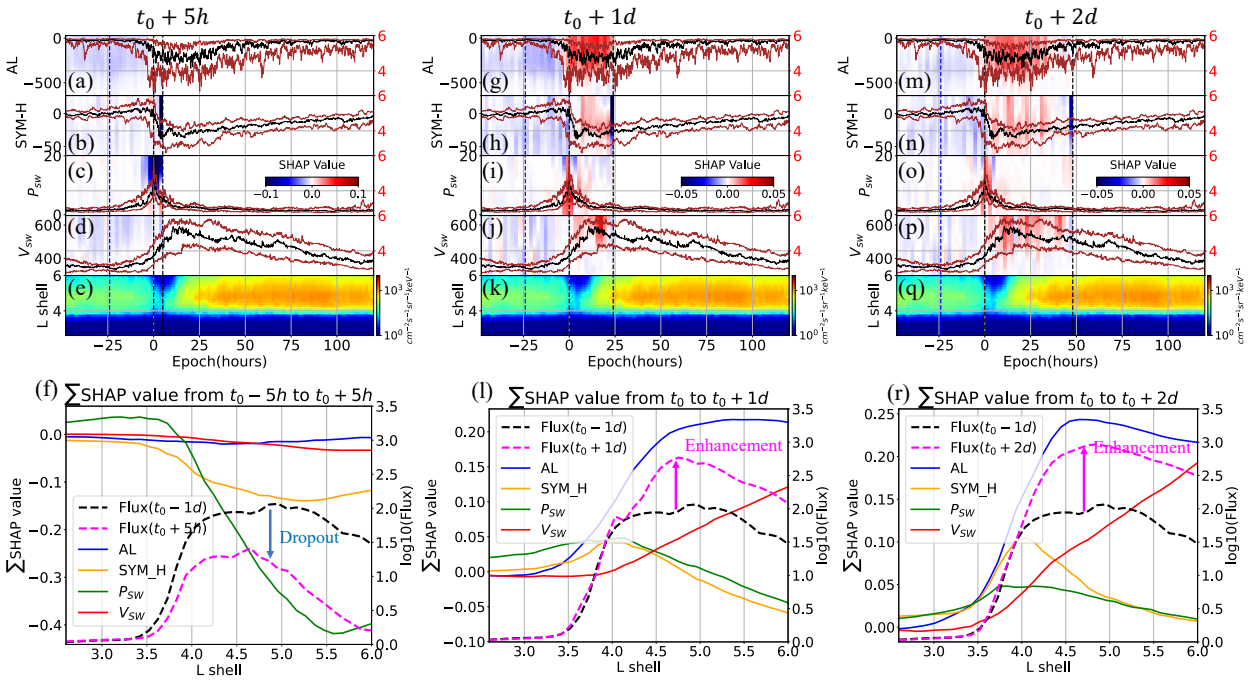

Figure 5.2: Superposed epoch analysis and SHAP interpretation of geomagnetic indices and solar wind parameters for an enhancement event at three different times. The black lines in the upper three panels correspond to the median value, while the red lines correspond to the upper and lower quantiles. The vertical dashed line at $t_0 = 0$ is defined as the maximum of the solar wind pressure Psw. The vertical dashed line at $t = t_0 - 24h$(1d) is used to define the initial flux as used in panels (f, l, and r). The vertical dashed lines at $t_0 + 5h$ (a-f), $t_0 + 24h$ (g-l) and $t_0 + 48h$ (m-r) are the times used to evaluate the corresponding SHAP values. The median SHAP values of all events are then color-coded on the corresponding input features. (e, k and q) show the median flux results from ML model at 909 keV energy. The dashed lines in (f, l and r) show the initial flux (black) and target flux (Magenta) at different L shells and times. The solid lines show the sum of median SHAP results of different indices: AL (blue), SYM-H (yellow), Psw (green) and Vsw (red) indicating their overall event importance.

at $t_0 + 5h$, where all other input values contribute to the output only weakly at this time. Figure 5.2f shows the sum of median SHAP values shown in Figure 5.2a-d, of the different indices (solid lines), and the output flux result at $t_0 + 5h$ (yellow dashed line) compared to the initial flux at $t_0 - 1d$ (purple dashed line). The flux is seen to decrease at higher L-shells (L > 4). The corresponding sum-SHAP results indicate that Psw (green line) is the primary contributor to the dropout as it has the lowest negative sum-SHAP values occurring at L > 4. The feature attribution results here are consistent with physcial understanding gained from previous studies during the storm time event [*Turner et al.*, 2013]. They can be interpreted to mean that the dayside magnetopause causes trapped electrons to escape the outer boundary through magnetopause shadowing [*Ukhorskiy et al.*, 2006] and occurs as the result of magnetopause moving abruptly inward in reaction to increased Psw. The enhanced SYM-H may be indicative of the Dst effect, inflating the outer radiation belt to larger L-shells and accelerating the rate of magnetopause shadowing loss.

Figures 5.2g to 5.2l show the result for the early acceleration phase at $t_0 + 1d$, when the enhancement of the fluxes starts to become apparent. The cluster of AL peaks (Figure 5.2g) occurring immediately after t_0 is brightly highlighted in red (i.e., positive SHAP values) which indicates that it contributes most to the acceleration of fluxes at higher L-shell (L > 4). It is worth noting that the high solar wind speed (Figure 5.2j) also contributes to the acceleration at high L-shells, and we believe that is due to the collinearity between AL and Vsw, and will be discussed at the end of this section. Interestingly, there is some positive contribution to the flux from Psw (Figure 5.2i) at low L-shells (L<5) which may be associated with the compression occurring in the interior region of the ring current, but this conjecture requires further investigation.

Figures 5.2m to 5.2r show the SHAP results for the late acceleration phase, at $t_0 + 2d$, when the flux has reached its upper limit. As above, the results show that the highest contribution to the acceleration is from the cluster of AL peaks occurring immediately after t_0. Thus, it can be surmised that high-intensity continuous substorm activity produces

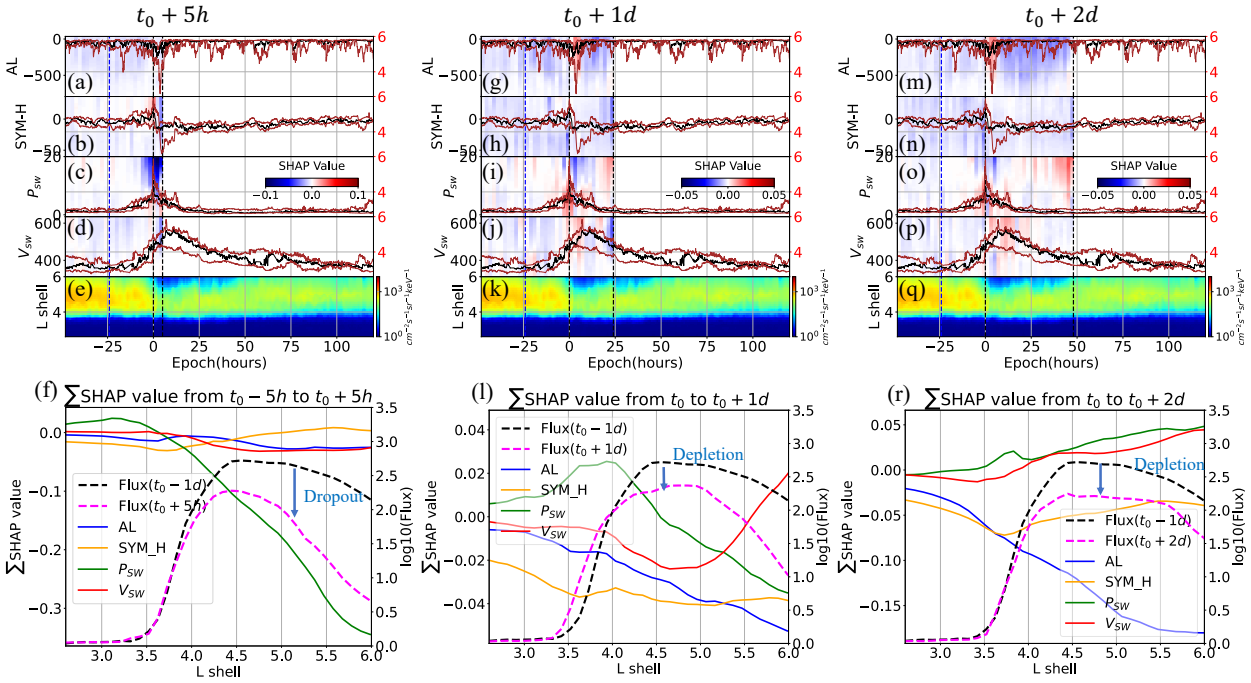

Figure 5.3: Same as Figure 5.2 except for depletion events

enhanced fluxes of outer belt electrons through the injection of source and seed electrons [*Jaynes et al.*, 2015], and continuous acceleration by enhanced chorus waves during such active times [e.g. *Hua et al.*, 2022a].

Figure 5.3 demonstrates the SHAP-enhanced superposed epoch analysis results corresponding to the 7 depletion events identified as described above. Figures 5.3a to f show the dropout process occurring in a very similar manner to the one in Figure 2e, with the minimum flux still occurring at around $t_0 + 5h$. The Psw enhancement is again seen to provide a negative contribution to the flux at higher L-shells (L > 4). The results indicate that the effect of magnetopause shadowing is present in both groups of events, and electrons are quickly lost at higher L-shells because of the same process, with a smaller contribution coming from SYM-H in the present set of events. Figures 5.3g to l show the early-stage development of the depletion of the fluxes and the SHAP results after the pressure maximum at $t_0 + 1d$. The late stage development of the depletion is displayed in Figures 5.3m-r for

the period $t_0 + 2d$. Figure 5.3r shows the negative sum-SHAP values from AL and Figures 5.3g and 5.3m indicate that those negative AL contributions are the result of quiet substorm activity following the pressure enhancement. It is perhaps surprising at first that an extended period of low AL values act as the dominant contributor to the flux depletion, but this can be understood as follows: since the events in both acceleration and depletion groups experience a similar dropout process, the key determining feature of whether the flux ultimately becomes enhanced or depleted is essentially the total substorm activity that follows the dropout, as indicated by AL after t_0. The strong, continuous substorm activity (indicated by cluster of AL peaks) leads to subsequent overall acceleration, whereas quiet substorm activity (indicated by period of AL $\sim$ 0 nT) is needed to create a depletion.

To further confirm our conclusions obtained from the SHAP results, Figure 5.4 shows the statistical results from a larger dataset containing 71 events obtained in a similar way as previously described in Section 5.2. Figures 5.4a to 5.4c depict the average measured flux from Van Allen Probes at different L-shells and three distinct times. The epoch time t_0 still represents the maximum of solar wind dynamic pressure Psw, and the three times picked for comparison are the initial stages prior to the dropout ($t_0 - 1d$), the dropout stage ($t_0 + 5h$), and the final stage ($t_0 + 2d$). The average |AL| is calculated in the time interval ranging from t_0 to $t_0 + 2d$ as indicated on the SHAP results in Figures 5.2 and 5.3 for each event. Figure 5.4a demonstrates that under quiet substorm activity ($\overline{|\mathrm{AL}|} < 100$nT), the flux first decreases for L > 4 at the dropout stage, and the flux at the final stage remain at low levels similar to the flux level at the dropout stage. This indicates that the relativistic electron flux cannot be accelerated in this range of substorm activity levels. Figure 5.4b shows a similar flux level to Figure 5.4a at both the initial and dropout stages but the flux at the final stage (red-colored curve) is enhanced to a level that is higher than the initial stage.

Figure 5.4c presents the results corresponding to very strong substorm activity levels following the pressure maximum. The pre-storm flux is slightly higher than in Figures 4a and 4b, and the flux at the dropout stage is also higher at low L-shells. This could be related

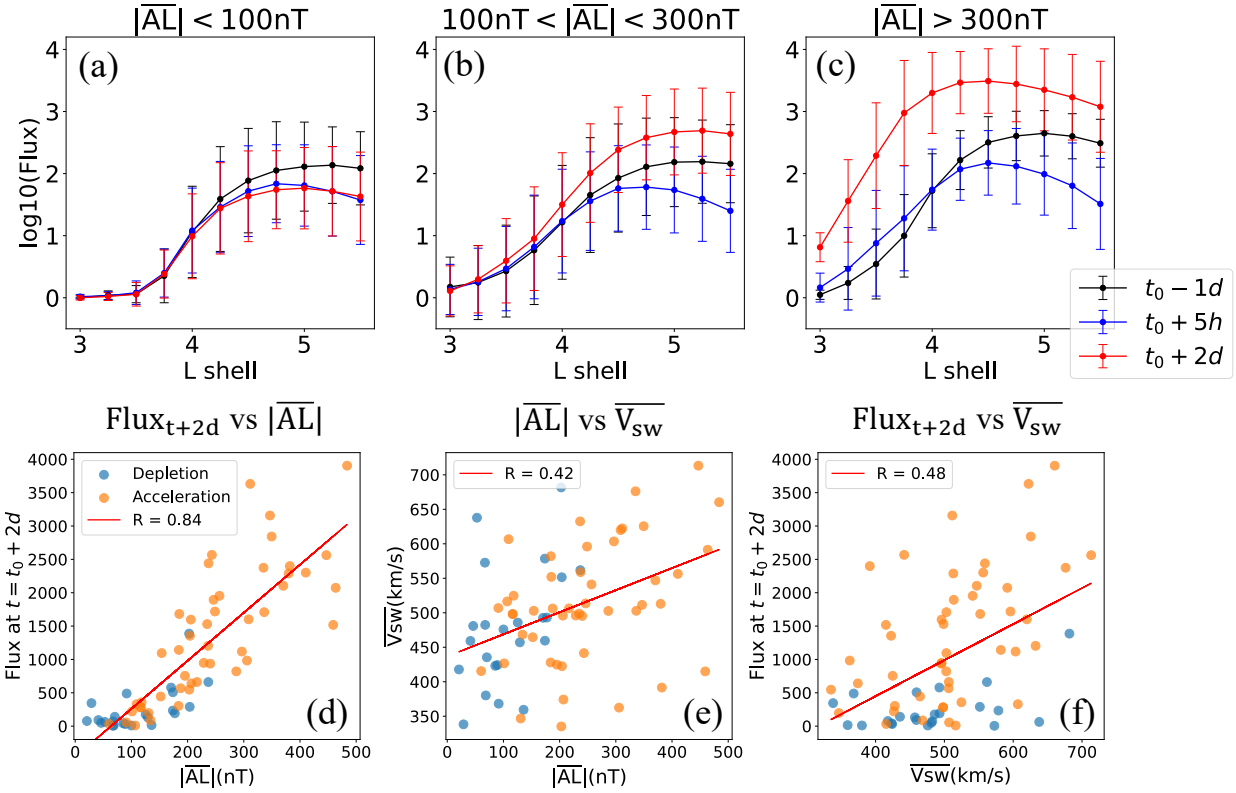

Figure 5.4: The statistical results from 71 flux events and the relation to different geomagnetic indices and solar wind parameters. (a-c) The statistical flux measurements for 909 keV energy at $t_0 - 1d$ (black), $t_0 + 5h$ (blue) and $t_0 + 2d$ (red) with different $\overline{|\mathrm{AL}|}$, where the $\overline{|\mathrm{AL}|}$ is the average |AL| from t_0 to $t_0 + 2d$. The vertical error bars in each plot show the minimum and maximum range of the distribution of events in each L-shell bin. (d) shows the resulting flux at $t_0 + 2d$ from measurements at L = 5 categorized by depletion (blue) and acceleration (orange) events, and its linear relation with $\overline{|\mathrm{AL}|}$. (e) shows the relation between $\overline{|\mathrm{AL}|}$ and $\overline{\mathrm{Vsw}}$, where $\overline{\mathrm{Vsw}}$ is average Vsw also from t_0 to $t_0 + 2d$. (f) shows the resulting flux at $t_0 + 2d$ and its relation to $\overline{\mathrm{Vsw}}$, indicating that the correlation exists, but is not as strong as that with $\overline{|\mathrm{AL}|}$.

to the fact that these strong substorm events usually follow strong geomagnetic storms, which may affect the characteristics of the dropout (and will be examined in future studies). The fluxes at the final stage are seen to be enhanced to a significantly higher level than those corresponding to weak and moderate substorm conditions.

Figure 5.4d then demonstrates the relation between the flux at $t_0 + 2d$ (Flux_{t+2d}) at L = 5 and the average absolute value of the AL index, $\overline{|\text{AL}|}$. The results show a high correlation coefficient ($R = 0.84$) between the two values which is consistent with previous studies [*Hua et al.*, 2022a, 2023a; *Mourenas et al.*, 2019; *Smirnov et al.*, 2020]. Compared to prior studies, our interpretable ML SHAP method doesn't require extensive statistics based on different variables. Instead, it directly identifies the key influencing variable AL and the time ranges after Psw enhancement that are most significant. Our findings indicate that the depletion events can essentially be thought of as "non-acceleration" events, occurring when the substorms that follow the enhanced Psw are not sufficiently strong to enhance the flux above its prior dropout level.

Although the SHAP profiles shown in Figures 5.2l and r suggest that the high solar wind speed contributes to the flux enhancement, it is not necessarily a condition that directly relates to the fluxes. This can be explained by noting that the training process of the ML model uses a feature selection method by adding the most informative drivers sequentially to the model [*Ma et al.*, 2022], and shows that AL is the most important parameter, but adding Vsw does not affect model performance much since most of its information is reflected in AL, but also include geoeffectiveness. Figure 5.4c shows the correlation between the average AL and Vsw, and Figure 5.4f shows the relation between Flux_{t+2d} and the average Vsw. Neither AL nor the flux shows a good correlation to Vsw. In fact, the AL index can be modeled more accurately by the combination of solar wind speed and IMF Bz [*Li et al.*, 2007b; *McPherron et al.*, 2015]. The prolonged southward Bz together with high solar wind speed gives strong, continuous AL excursions, which drive the flux enhancement in the ML model. So the SHAP result of solar wind contribution may be due in large part to the collinearity between AL

and Vsw.

5.4 Summary and discussion

In this chapter, we investigated the response of relativistic radiation belt electron fluxes at 909 keV to various solar wind and geomagnetic drivers. By combining an interpretable ML method and superposed epoch analysis, we reconstructed the fluxes and directly identified the key driving features of the electron flux enhancement and depletion events as a function of time from the Psw enhancement and L-shell.

The application of SHAP feature attribution method to the 19 enhancement and 7 depletion events has shown the following:

1. An increased solar wind dynamic pressure is the dominant contributor to the dropouts preceding both enhancement and depletion events.

2. The high-intensity, continuous substorm activity following the pressure maximum (indicated by a cluster of AL peaks) contributes to the rapid increase of electron fluxes following the dropout during enhancement events.

3. The quiet condition, or lack of substorm activity following the initial dropout, contributes to the decrease of electron flux during depletion events.

To get more insight into our results, we performed a statistical study on a large set of 71 geospace disturbances events. The results show significant correlation between the resulting fluxes and average AL value following solar wind pressure maxima. These results, in combination with our SHAP results, indicate that the depletion events can be thought of essentially as "non-acceleration" events that occur when substorm activity following the pressure maximum is not sufficient to accelerate the fluxes above its pre-storm level.

Our study utilizes a novel approach to modeling and understanding the dynamics of Earth's radiation belt. Although the Superposed Epoch Analysis (SEA) is a popular method

for identifying correlations between physical parameters involved in radiation belt dynamics, and hence inferring the causative driving factors, it has a number of important limitations. Specifically, the SEA cannot identify the roles of key parameters during rapid radiation belt flux changes, when the different parameters change simultaneously, or their roles in driving flux dynamics change as a function of time and/or L-shell; therefore, its results are often difficult to verify using physics-based models such as quasilinear simulations. In contrast, our interpretable ML model is not only capable of accurately reproducing the dynamics of the radiation belt, but it can also directly identify the key features corresponding to various significant dynamics, as they evolve in time and space, and which are shown to be in line with our physical understanding.

The results show that average AL has a significant correlation with the resulting flux levels suggest that it is important to incorporate the AL index more directly into the radiation belt modeling. It is worth noting that the cluster of AL peaks can not only be used in identifying strong whistler-mode wave intensity [*Li et al.*, 2009], but can also relate to the plasma frequency to gyrofrequency ratio (ω_{pe}/ω_{ce}) that affects the electron loss and energization efficiency and time scales [*Agapitov et al.*, 2019]. The purely data-driven results will serve as a baseline for future studies, that the density and wave models based on AL can be used in the radiation belt simulation. Furthermore, our conclusions should be applicable to a wide energy range of radiation belt electrons (e.g., 500 keV - 7 MeV), although there may be some quantitative differences for different energies. We only investigate a typical energy channel to demonstrate our method and leave others for future studies. The dropout occurrence rate and the magnitude of flux decrease during dropout may depend on the electron energy [*Xiang et al.*, 2018]. The acceleration of higher energy electrons also requires a longer time to develop [*Thorne et al.*, 2013], therefore requiring the SHAP values in the previous times.

Finally, a number of caveats of our present work need to be mentioned. The uncertainty of the SHAP interpretability method comes primarily from the ML model itself, and there could be differences between the training and test datasets when explaining individual samples, so

a model with very accurate performance should always be prioritized, as in the present case. We show the model performance and each model result in the provided repository [*Ma*, 2023]. The SHAP and other feature attribution methods usually assume feature independence, and this property requires us to choose the input features carefully, since it is clear that solar wind parameters ultimately control geomagnetic index values, albeit in complex ways. Although we chose our input features based on the strategy of adding the most informative predictors sequentially, there could still be hidden interactions that are ignored such as the solar wind and AL mentioned above. Possible solutions are using tree-like models that can have global interpretation and feature interaction [*Lundberg et al.*, 2018], or using encoding and self-supervised methods [e.g. *He et al.*, 2020] to map the input features to higher dimensions.

Despite the above caveats, we have demonstrated that a SHAP-enhanced superposed epoch analysis (SHESEA) has the unique ability to provide context for the standard SEA method, showing how independent variables control the dependent variable, how their roles vary as a function of time and how this behavior changes as a function of space. This approach is general, and can be applied in a variety of situations where a standard SEA method is typically used, and is a novel way that ML can be used as an insight discovery tool in physical science.

CHAPTER 6

Back to physics: Simulating the Earth's Outer Radiation Belt Electron Fluxes and Their Upper Limit: A Unified Physics-Based Model Driven by the AL Index

It is understood that geomagnetic indices and solar wind conditions can drive the electron flux dynamic in the radiation belts in Chapter 3. Further, the interpretable methods in Chapter 4 and 5 revealed that the continuous substorm activity (AL) is the key input feature that determines the flux level after storms. In this chapter, we go back to physics and use what we learned from the ML models to perform the physics-based simulation. We develop a physical model driven by the integral auroral index (AL), which influences the amplitude of plasma waves and the density of the background plasma. We simulate a large sample of 186 events from 2012 to 2018 for the first time. The results show that this model not only reproduces the acceleration of electrons at high energy levels but also reveals that sustained strong substorms act as a switch: high energy electrons are seen to be accelerated only when the intensity of sustained substorms exceeds a certain threshold.

6.1 Introduction

Linking the solar wind or the geomagnetic perturbations caused by the solar wind with the dynamics of electrons has become an essential method for understanding and predicting

the radiation belt dynamics as the flux level of energetic electrons varies significantly in response to changes in the properties of the solar wind or geomagnetic conditions [*Li and Hudson*, 2019]. Statistical analyses examined the correlation between high energy electrons and solar wind conditions and geomagnetic activities, for instance, *Meredith et al.* [2003] found that the most significant electron flux enhancements outside the plasmapause were associated with periods of prolonged substorm activity. *Zhao et al.* [2017b] demonstrated there is a good relation between ultra-relativistic electron enhancement ($>$ 3 MeV) and solar wind speed, as well as the AL index. *Zhao et al.* [2019a] further showed that even small and moderate storms can accelerate electrons to multi-MeV energies. However, statistical studies alone have difficulty explaining the exact causativephysical mechanisms involved, as different driving factors typically occur simultaneously [e.g. *Tsurutani et al.*, 2006]. Event studies have also been performed to investigate the underlying physical mechanisms causing the relativistic electron acceleration. The mechanisms of particle acceleration are generally divided into two categories or a combination of the two effects: local acceleration by chorus waves [e.g. *Thorne et al.*, 2013; *Reeves et al.*, 2013] and inward radial diffusion from higher L-shells [e.g. *Ozeke et al.*, 2019, 2020]. *Drozdov et al.* [2015] used the Kp index to parameterize the diffusion coefficients to drive a long-term Fokker-Planck simulation, but the results show a significant discrepancy for the ultra-relativistic electrons. Our previous research using ML methods successfully simulated electrons at relativistic energy levels and achieved better results than general physical models [*Chu et al.*, 2021; *Ma et al.*, 2022], but it was less effective in simulating electrons in the ultra-relativistic range, likely due to a much smaller set of events at these high energies. Thus, the present study focuses on understanding electron flux behavior, informed by the results of our previous machine-learning-based models, especially for the ultra-relativistic range.

Agapitov et al. [2019] and *Allison et al.* [2021] suggested that during geomagnetically active times, the electron density drops to a very low values and creates favorable conditions for ultra-relativistic electron acceleration by chorus waves, consistent with earlier simulations

by *Thorne et al.* [2013]. *Hua et al.* [2022a, 2023b] show the maximum electron flux at different energy levels is strongly correlated to the cumulative effects of substorms instead of storms. Our previous ML models were driven only by geomagnetic indices and solar wind parameters, and with interpretable ML methods, we automatically discovered the integrated AL is a key parameter in the acceleration mechanism for relativistic and sub-relativistic electrons [*Ma et al.*, 2023, 2024]. These studies indicate that we can use the AL index to model the time-varying physical parameters needed for traditional Fokker-Planck simulations, thereby obtaining a general model driven only by the auroral index. We use this idea as a basis for further investigation into the acceleration mechanisms of ultra-relativistic electrons, and perform a series of simulations that cover all the 2012-2018 storm time events. We describe our methods in Section 6.2 and demonstrate the result in Section 6.3. We discuss our conclusions in Section 6.4.

6.2 Events selection and Simulation Methodology

We attempt to simulate all the storm-time enhancement events occurring during the Van Allen Probe era and investigate the conditions that led to the acceleration of relativistic and ultra-relativistic electrons. The criteria used to select simulation events are that the minimum SYM-H < -25nT, and there is at least a 2-fold increase at 597 keV electron flux (the upper energy of seed population) during the storm event. We selected 186 events from September 2012 to September 2018 based on the above criteria, and then we performed simulations of each event.

Figure 6.1a-o presents one of our selected storms occurring on 2012-10-09 which has been well studied in the past [*Thorne et al.*, 2013]. The time t_0 is defined as SYM-H minimum (same for all the events) on 10-09, the event start date is defined as $t_0 - 1$ day as the left vertical dashed line, and the simulation period is from t_0 to $t_0 + 2$ days (taken to be the same for all the events) as shown in the shaded area. The most significant challenge for us is how

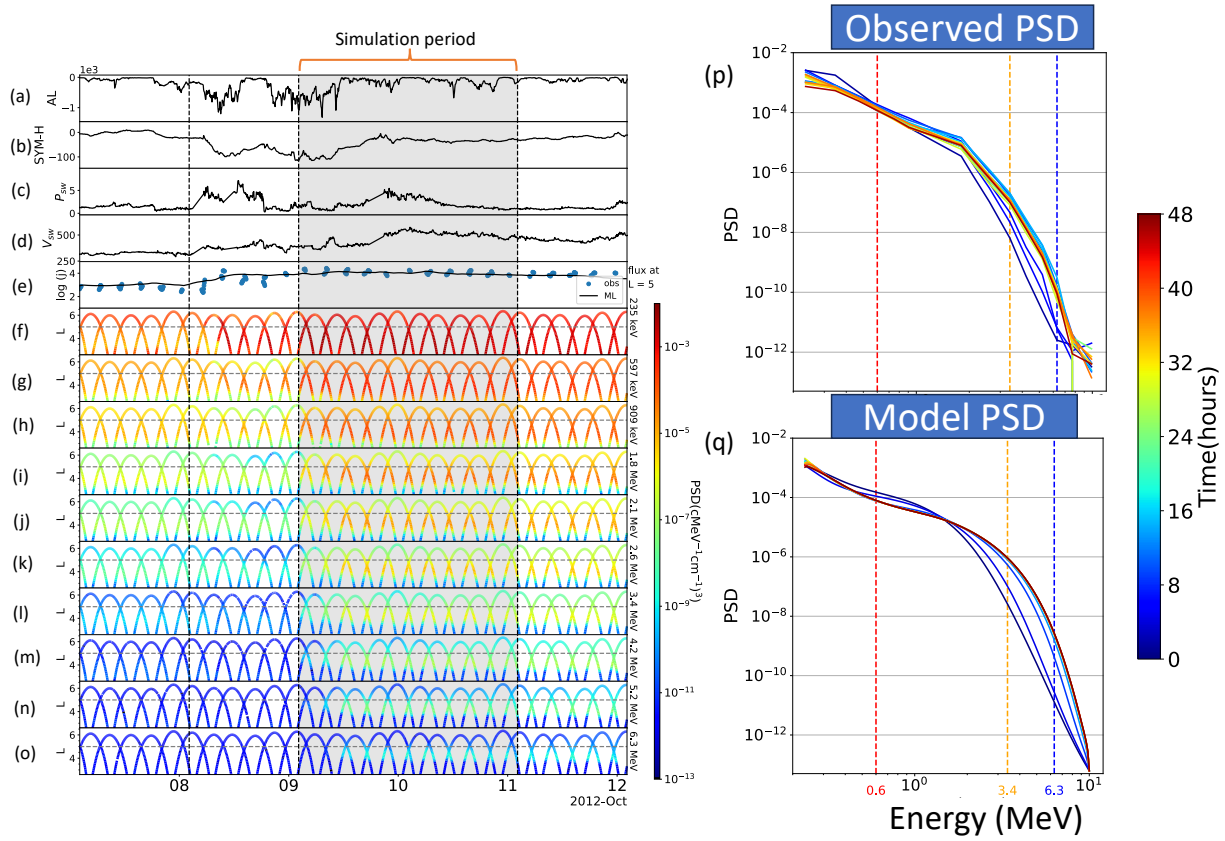

Figure 6.1: An example of a selected case and its associated FP simulation which occurred on 2012-10-09. (a-d) Geomagnetic indices such as AL and, SYM-H, and solar wind dynamic pressure P_{SW}, and solar-wind speed V_{SW};, (e) black solid line shows the machine learning result of 235 keV electron flux at L = 5 and MLT = 6 (black line) together with observations (blue dots). (f-o) The observation PSD of different energy channels, where black horizontal dashed lines represent L = 5. (p) Observed PSD color-coded with time. (q) FP simulation result of the event. The vertical dashed lines in (p) and (q) represent 0.6 MeV (red), 3.4 MeV (yellow) and 6.3 MeV (blue) energies.

Frequency spectrum			
ω_m	$0.25\Omega_{ce}$	d_ω	$0.10\Omega_{ce}$
Wave normal angle		**Wave latitude range**	
θ_{min}	$0°$	MLT 0 to 4	$0° - 15°$
θ_{max}	$45°$	MLT 4 to 8	$0° - 25°$
θ_m	$0°$	MLT 8 to 12	$0° - 45°$
θ_w	$30°$	MLT 20 to 24	$0° - 20°$

Table 6.1: The wave properties used in the diffusion coefficient matrix calculation. The wave frequency is determined by a Gaussian distribution $B^2(\omega) \sim \exp\left(-\frac{(\omega-\omega_m)^2}{\omega_w^2}\right)$. The wave normal angle distribution is $B^2(\theta) \sim \exp\left(-\frac{(\tan(\theta)-\tan(\theta_m))^2}{\tan^2(\theta_w)}\right)$ with cutoffs at θ_{min} and θ_{max}.

to perform 186 simulations since the traditional Fokker-Planck simulation approach requires a large amount of computational sources to calculate the diffusion coefficients [*Ni et al.*, 2008]. We use a diffusion matrix pre-calculated from statistical results of wave properties with different density values and a wave amplitude $B_w = 100$pT which are then scaled by the modeled wave amplitude and interpolated as a function of density, as done in the lookup table method to calculate diffusion coefficients [*Hua et al.*, 2022b]. The statistical wave properties used in this study are based on the Van Allen Probes survey [*Li et al.*, 2016] and listed in Table 6.1.

We use the integral hourly AL index value obtained from the OMNI dataset summed over the previous 3 hours as the driver for each hourly step to model the wave amplitude and density profile. Figure 6.2a shows the correlation between the cumulative AL and the power of the magnetic field fluctuations. The data is obtained from Van Allen Probes observations near the heart of the outer belt acceleration region, at L = 5, collected over L from 4.8 to 5.2 and observed within 15° from the magnetic equator when the probes are outside of plasmapause. The statistical results are divided into 6 levels of activity and four

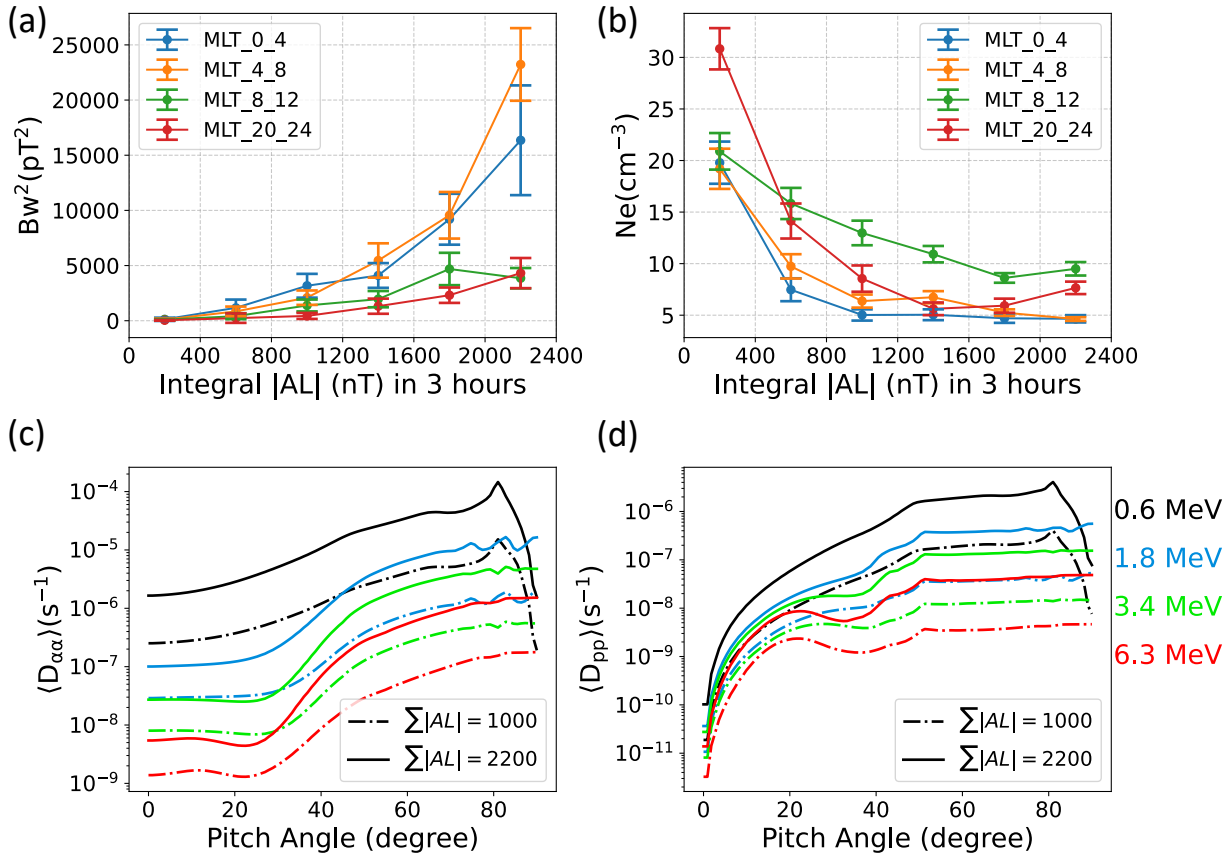

Figure 6.2: Stastical results of AL driven wave and AL driven density models at L = 5 and the corresponding average diffusion coefficients. (a) The statistical result of wave magnetic intensity at four different MLT sectors. (b) The statistical result of electron density. (c) The average pitch angle diffusion coefficients $\langle D_{\alpha\alpha} \rangle$ and (d) the average momentum diffusion coefficients as a function of pitch angle at different energies.

different MLT sectors which we will use to calculate the average diffusion coefficients. The acceleration over the dayside MLT sector 12 – 20 h is ignored due to the low chorus wave activity that occurs near the equator in that region. It is clear that as geomagnetic activity increases, the associated wave magnetic intensity increases, especially in the night-dawn sectors, consistent with previous studies [e.g. *Teng et al.*, 2018]. It is worth mentioning that the vertical lines extending from each data point represent only 10% of the standard deviation in the measurements for the sake of clarity, which means that there are huge uncertainties for large wave amplitude. Figure 6.2b shows the electron density measurement outside the plasmapause near L = 5, similar to Figure 6.2a. Importantly, a global decrease in density is observed during high geomagnetic activity. Such low-density observations (below 10 cm^{-3}) can contribute to the ultra-relativistic electron acceleration as the wave phase velocity and electron resonance energy increase with a density reduction [*Agapitov et al.*, 2019; *Allison et al.*, 2021]. The combination of wave power enhancement and density decrease during the intense substorm period can result in a factor of 10 enhancement in the average pitch angle and momentum diffusion coefficients, as shown in Figures 6.2c and 6.2d.

The chorus waves typically cause both pitch angle scattering loss and acceleration of electrons in the radiation belts. The scattering and acceleration rates are represented by the bounce-averaged pitch angle $\left\langle D_{\alpha_{\mathrm{eq}}\alpha_{\mathrm{eq}}}\right\rangle$, momentum $\langle D_{pp}\rangle$, and mixed pitch angle-mementum $\left\langle D_{\alpha_{\mathrm{eq}}p}\right\rangle$ diffusion coefficients. To evaluate the electron flux variations due to chorus, we perform a local acceleration simulation driven by chorus waves by numerically solving the 2D Fokker-Planck equation [*Ma et al.*, 2012], expressed as:

$$\begin{aligned}\frac{\partial f}{\partial t} = & \frac{1}{S\left(\alpha_{\mathrm{eq}}\right)\sin\alpha_{\mathrm{eq}}\cos\alpha_{\mathrm{eq}}}\frac{\partial}{\partial\alpha_{\mathrm{eq}}}\left(S\left(\alpha_{\mathrm{eq}}\right)\sin\alpha_{\mathrm{eq}}\cos\alpha_{\mathrm{eq}}\left\langle D_{\alpha_{\mathrm{eq}}\alpha_{\mathrm{eq}}}\right\rangle\frac{\partial f}{\partial\alpha_{\mathrm{eq}}}\right) \\ & + \frac{1}{S\left(\alpha_{\mathrm{eq}}\right)\sin\alpha_{\mathrm{eq}}\cos\alpha_{\mathrm{eq}}}\frac{\partial}{\partial\alpha_{\mathrm{eq}}}\left(S\left(\alpha_{\mathrm{eq}}\right)\sin\alpha_{\mathrm{eq}}\cos\alpha_{\mathrm{eq}}p\left\langle D_{\alpha_{\mathrm{eq}}p}\right\rangle\frac{\partial f}{\partial p}\right) \\ & + \frac{1}{p^2}\frac{\partial}{\partial p}\left(p^3\left\langle D_{p\alpha_{\mathrm{eq}}}\right\rangle\frac{\partial f}{\partial\alpha_{\mathrm{eq}}}\right) \\ & + \frac{1}{p^2}\frac{\partial}{\partial p}\left(p^4\left\langle D_{pp}\right\rangle\frac{\partial f}{\partial p}\right)\end{aligned} \tag{6.1}$$

where f is the phase space density (PSD), t is the time, and $S(\alpha_{eq})$ represents the bounce period approximated by $S\left(\alpha_{eq}\right) = 1.38 - 0.32\sin\left(\alpha_{eq}\right) - 0.32\sqrt{\sin}\left(\alpha_{eq}\right)$ [*Lenchek et al.*, 1961]. The lower energy boundary is set as the electron PSD at 235 keV provided by our machine learning model [*Ma et al.*, 2022], which is primarily driven by the AL index during the post-storm period [*Ma et al.*, 2023, 2024], as shown in the solid line in Figure 6.1e. The lower boundary is set to be higher than in previous simulations as we focus on the relativistic electrons. The initial PSD distribution is adopted from a spline fitting from 235 keV to 7.7 MeV, and the upper energy boundary is set at 10 MeV with a constant value $10^{-13}\left(\mathrm{cMeV}^{-1}\ \mathrm{cm}^{-1}\right)^3$. The initial pitch angle distribution is assumed to be $f\left(\alpha_{\mathrm{eq}}, p\right) = f\left(\alpha_{\mathrm{eq}} = 90^{\circ}, p\right)\sin\alpha_{\mathrm{eq}}$. With the time-varying wave amplitude and total electron density from statistical results, we now update the diffusion coefficients every hour with the changing integrated AL driver. Figures 6.1p and 6.1q demonstrate the observation and simulation results. The model captures the rapid enhancement at high-energy levels clearly and the simulation result is consistent with a few previous studies on the same event [*Hua et al.*, 2022c; *Thorne et al.*, 2013].

6.3 Results

Our focus in this study is not to reproduce a single event but to capture the collective behavior of the model on radiation belt acceleration of relativistic and ultra-relativistic electron fluxes occurring consistently over many events. Figure 6.3 shows the results of all 186 simulations at different energy channels. Notably, the model underestimates the electron PSD below 2 MeV shown in Figures 6.3 a-c. Such a modeling bias is expected, as our simulation only considers local acceleration and does not take radial diffusion into account. Specifically, the radial diffusion process will transport energetic electrons from higher L shells inward, resulting in the additional enhancement at our simulation position L = 5 [*Zhao et al.*, 2019b]. The radial diffusion coefficients may be higher at lower energies [*Liu et al.*, 2016], which leads

to a more significant bias in the lower energy range. In addition, the bias may also come from the fast injection process as the injected electron energy during storm time can be higher than the lower boundary (235 keV) in the simulation. Another possible issue is the difference between the fluxes measured by MagEIS and the REPT instruments at 1-2 MeV energies. For example, the REPT flux measurement at 1.8 MeV is about 2-10 times higher than the MagEIS at a similar energy channel 1.728 MeV [*Boyd et al.*, 2019]. Figures 6.3d-g show a very good agreement between the simulation and observation at the relativistic energy range. Importantly, multiple years of observations show that the ultrarelativistic electron flux is only sometimes increased after storm times, especially at higher energy levels [*Baker et al.*, 2019]. Figure 6.3i shows the model performance at 6.3 MeV with red lines separating the results into different regions. It is clearly seen that the model captures not only the enhancement but also most non-enhancement events where the post-storm flux level remains at the noise level. These results demonstrate that our method parameterized by the AL index can successfully capture the threshold between enhancement and non-enhancement for electron fluxes.

We now aim to understand what leads to the critical enhancement threshold levels that control high energy fluxesy levels. Given that our model is driven by the AL index, we investigate the relation between the result electron flux and integral AL (integrated with 5-min resolution AL from $t_0 - 1$ day to $t_0 + 2$ day) and compare the results from observations and simulations. Figure 6.4a shows the flux observations at the end of each event. The flux is normalized by the minimum and maximum flux for each energy channel among all the events. Each dot represents one flux observation color-coded by the normalized flux. At lower energies (< 1 MeV), the fluxes have a strong linear relationship with the integral of the AL index, which is seen more clearly in Figure 6.4b. At higher energies (> 1 MeV), the flux remains at a very low level when the integral AL is low, but becomes enhanced only when the integral AL surpasses a threshold x_0. We thus define a criterion to find such a

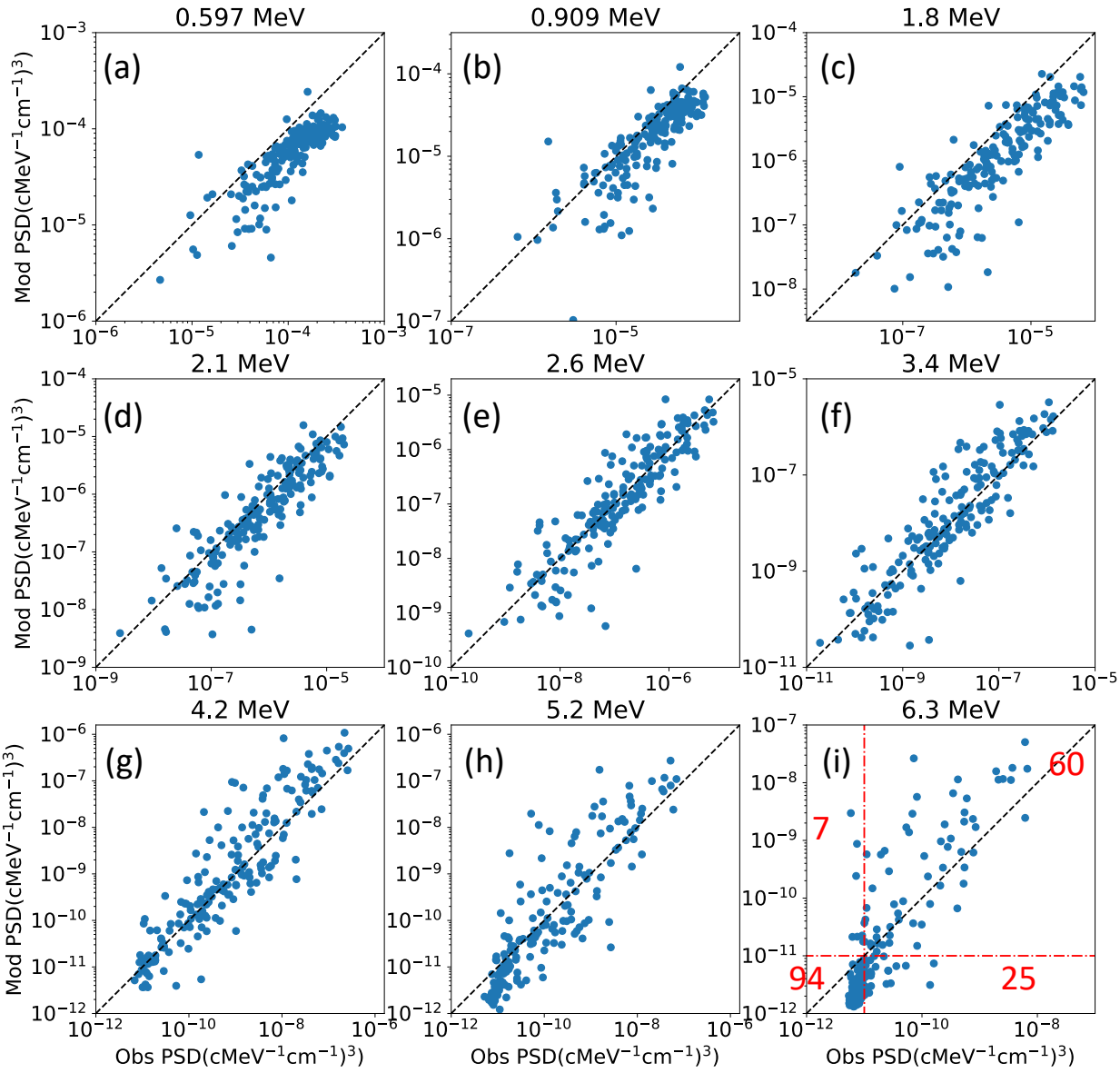

Figure 6.3: Model results compared with the observations at different energy channels. The model performance for the occurrence of 6.3 MeV flux enhancement is marked by the red lines and event numbers. The model captures 94 events that are below the noise level and 60 events that are above it, thus identifying a naure bouondary between enhancement and non-enhancement events.

critical threshold x_0:

$$\frac{\sum_{x \geq x_0} I(y(x) > 0.05)}{\sum_{x \geq x_0} 1} \geq 0.70 \tag{6.2}$$

where the x is the integral AL of each event, and $y(x)$ is the corresponding flux value. The "switch" function I is 1 when $y\,(x) > 0.05$, otherwise is 0. So, such criterion can find the critical threshold x_0 where 70% of the events can end with a clear enhancement when the integral AL is larger than x_0. The observation threshold is shown as dashed lines in Figures 6.4b-d and as a dash-cross line for each energy channel in Figure 6.4a, and the threshold increases with increasing energy as expected. Figure 6.4e-g shows the model results. We calculate the threshold with the same criterion for the modeled flux in Figures 6.4e-g, and the results compare very well with the observation, which confirms our notion that electron flux enhancements only become significant when substorms of a certain intensity persist for a sufficient duration, acting as a type of "turn on switch". Moreover, our physics-based model demonstrates that this is due to the controlling effect of prolonged substorm activity on increasing the chorus wave intensity and lowering the electron density in the radiation belt acceleration region (Figure 6.2).

6.4 Conclusions and Discussion

In this chapter, we investigated the local acceleration process of radiation belt electron fluxes driven by chorus waves and electron density provided by our models under various geomagnetic conditions. Using a lookup table method, we performed a series of event-specific radiation belt diffusion simulations to investigate electron acceleration during storm time during the Van Allen Probe era using an ensemble of 186 storm events. Our findings reveal that:

1. The chorus wave intensity and plasma density are both controlled by accumulated substorm activity: the stronger the substorm, the greater the wave intensity and the lower the electron density. This phenomenon is most pronounced in the night to

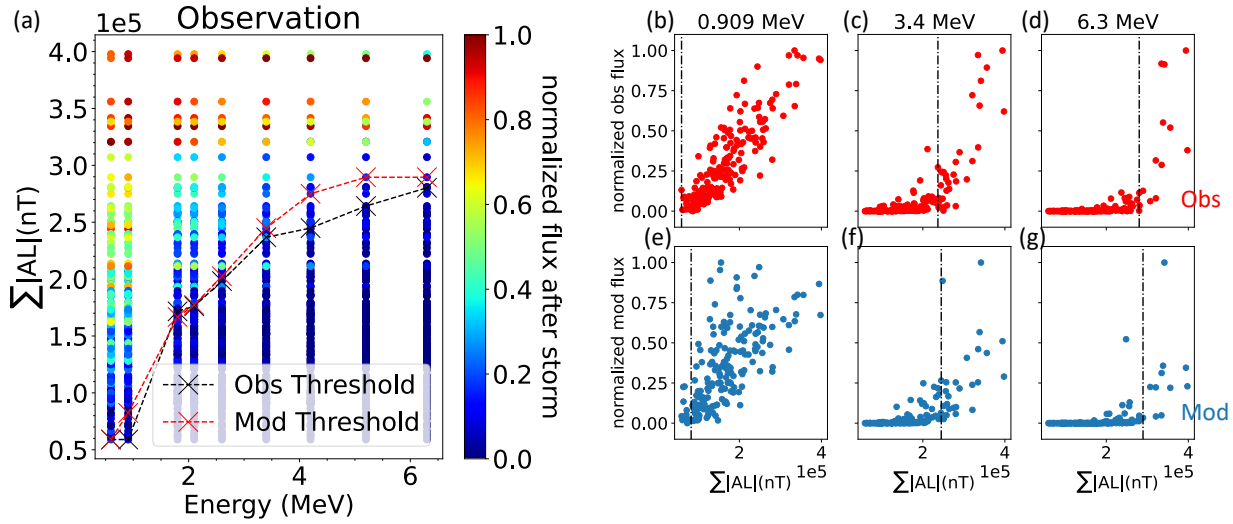

Figure 6.4: The modeled electron flux threshold comparison with observation. (a) The observed flux, normalized and color-coded by each channel's maximum and minimum flux. The dashed line and cross show the observed threshold (black) and modeled threshold (red). (b-d) The observation results and the threshold at different energies. (e-g) The simulation results and the threshold at different energies.

the dawn MLT region which is critical for electron acceleration due to the intense, equatorial chorus waves that occur there.

2. We develop a general substorm-driven, local acceleration model using a lookup table method and simulate a large number of strom-time acceleration events at a range of energies, with good performance, illustrating that the accumulated substorm activities is the key parameter controlling relativistic and ultra-relativistic electron acceleration.

3. The electron fluxes following geomagnetic disturbances show a clear threshold integral AL, which controls whether a particular electron flux energy channel will be enhanced or not. These results indicate that the continuously elevated substorm activity is the determining factor for ultra-relativistic electron acceleration, and we demonstrate that this is due to the influence of substorms on both the electron density and wave intensity.

This study sheds new light on modeling and understanding the acceleration mechanism of ultra-relativistic electron fluxes. As far as we are aware, this is the first time that the critical geomagnetic activity threshold levels, physical models, and the underlying conditions under which electron flux can increase at high energies have been directly linked. The clear relationship between relativistic electron flux enhancement and sustained substorm activity sheds new light on the drivers of acceleration leading to potentially more effective and accurate model development in the future. For the sake of simplicity, we only consider local acceleration by lower band chorus waves in the heart of the outer radiation belt acceleration region at L = 5, which is close to the peak of the chorus wave intensity [*Aryan et al.*, 2021] and the maximum electron fluxes in the radial profile in the outer belt [*Hua et al.*, 2022a]. However, the model's good performance suggests that this processs may be the predominant mechanism and we can gradually add other mechanisms based on this model in the future studies.

Although in our model, substorms only affect the wave amplitude and the total electron density, it is important to note that enhanced injections are implicitly included in the

boundary and initial conditions, and their relationship with substorms has been generally known and appreciated [e.g. *Reeves et al.*, 1990]. When selecting events, we did not impose strict constraints on different Dst index, but we cannot conclude that Dst has no significant impact on relativistic electron enhancement. We followed the results obtained from ML to start with the AL index and studied the electron acceleration outside the plasmapause. The relationship between relativistic electron acceleration and geomagnetic storm strength still merits careful investigation.

CHAPTER 7

Summary and Outlook

In this chapter, I summarize the work presented in this thesis and briefly introduce some other models of different magnetospheric quantities that were born from, or inspired by this research. I then give an outlook on future research directions.

7.1 Summary

Earth's outer radiation belt contains relativistic electrons that are extremely dynamic and have the potential to cause harm to astronauts and satellites. Therefore, it is crucial to have a comprehensive understanding of the behavior of particles in the radiation belt.

We first try to address how to model Earth's radiation belt electrons. The typical approach is through Fokker-Planck (FP) simulations, which is a diffusion model describing the evolution of the electrons phase space density. However, the FP model nevertheless suffers from some simplifications that limit its general usage: (a) The diffusion coefficients due to plasma waves in the magnetosphere are usually parameterized by different geomagnetic indices, but there is no guarantee that such parameterizations are unique, and it could not represent nonlinear or potentially unknown physical processes. (b) Artificial boundary conditions are required to drive such simulation when there is no in situ observation available for a specific event, which could induce simulation errors. (c) Most research using Fokker-Planck simulations can model only general events since diffusion coefficients are developed based on statistically averaged quantities, yet demonstrates a limitation in reproducing specific events.

Thus, we need a new method to overcome these shortcomings.

We present an alternative approach to radiation belt modeling using a set of neural network models to reproduce the electron fluxes in Chapter 3. The models are trained on data from the instruments onboard Van Allen Probes and are only driven by a time history of geomagnetic indices and solar wind parameters, so they do not require boundary conditions and naturally contain all the physics. It is well known that ML can create useful and representative models from large data. However, correctly applying ML to satellite data presents a challenging problem. We conducted numerous experiments to obtain an accurate model capable of reproducing electron dynamics. We ultimately discovered that the two most crucial details in the training process are: 1. The input time history representing magnetospheric physical activity should be longer than or equal to the electron's decay time for different energy. This is because the input parameters can only encompass such a complete physical process. 2. When training with satellite data, we should pre-divide the data into training and validation sets based on reasonable intervals (several days) rather than using traditional random splitting of individual data samples. Satellite observations are fast and continuous; random splitting would result in almost identical data in both sets, which would not be effective for real independent training and testing sets. The models have been extensively tested and validated, showing high accuracy performance for out-of-sample data. Importantly, the model successfully captures electron dynamics over long- and short timescales for a range of different energies.

The goal is to turn data into information, and information into insight. Despite the exciting performance of our models, the lack of interpretability has been a major concern resulting from the use of such black-box models. The natural question that can be asked is, what insight can we get from our models? To answer such a question, we present a state-of-the-art feature attribution method to explain our electron flux model called SHapley Additive exPlanation (SHAP) in Chapter 4. SHAP assigns each input feature an importance value for a specific output, and the idea of SHAP is based on the Shapley value in game theory.

The Shapley value is a method used to determine the fair contribution of an individual player in a game with a coalition of players. Our model uses the time history of geomagnetic indices and solar wind parameters as the drivers which play the role of the different players in the coalition. By applying the SHAP method, we can quantitatively identify how various geomagnetic perturbations control different dynamics (see Figure 4.2). For a storm time event, the results show that the strong enhancement of solar wind pressure contributed to the rapid dropout seen at higher L-shells, which is consistent with the magnetopause shadowing effect and outward radial diffusion process. The acceleration of electron fluxes at higher L-shell was controlled dominantly by clusters of AL peaks, while at lower L-shells, the acceleration was mainly contributed by the SYM-H index, which is known as the "Dst effect". Regarding a non-storm time event, the acceleration was found to be clearly correlated to the substorm injection process. These findings, which are consistent with current physical understanding, not only demonstrate the reliability of the interpretation method but also its potential to help the discovery of missing physical processes. Our study thus provides the framework and motivation for a new way to model and explain radiation belt dynamics and other similar ML models.

Now that we have a framework for interpreting the radiation belt ML model, we explore some specific topics in Chapter 5. A well-known unsolved issue is that geomagnetic storms can result in either an increase or a decrease in the fluxes of relativistic electrons in response to similar inputs and the exact response is hard to predict. The traditional statistical way to address this problem is to conduct a Superposed Epoch Analysis (SEA) on the series of geomagnetic indices when similar events happen to identify the correlation between physical parameters involved in radiation belt dynamics and infer the causative driving factor. Such a method has a number of limitations. Specifically, the SEA cannot identify the roles of key parameters during rapid radiation belt flux changes, when the different parameters change simultaneously, or their roles in driving flux dynamics change as a function of time and L-shell; therefore, its results are often difficult to verify using physics-based models such as

quasilinear simulations. With our framework, we can perform similar SEA but conduct it together with an insight into how each feature controls the output (see Figure 5.2). The SHAP "enhanced" superposed epoch analysis (SHESEA) results show that the intensity and duration of the substorm sequence following an initial dropout determine the overall enhancement or depletion of electron fluxes. Further statistical results show a significant correlation between the resulting flux levels and the average AL index, indicating that the observed "depletion" event can be more accurately described as a "non-enhancement" event.

In Chapter 6, we discuss how to apply the results obtained from ML to physical simulations. Our main focus is on the ultra-relativistic energy range of electrons. As for this part, we cannot simply achieve good results using the same structure as previous ML models. The previous interpretable ML results show that the auroral indices (we use AL in our studies) are the key parameters in driving the acceleration mechanism. This means we can use AL to provide time-varying conditions for traditional FP simulations, thereby obtaining a general physics-based model for all the acceleration events. Two critical physical parameters are modeled by the AL index: wave amplitude and density. Our findings reveal that the intensity of waves and plasma density are both controlled by substorm activity; the stronger the substorm, the greater the wave intensity and the lower the electron density. This process, continuing over a period of time, creates the necessary conditions for local acceleration drivent by lower band chorus waves to reach MeVs.

Putting this thesis in the bigger context, we did not just create an ML model for radiation belt electrons, but demonstrated how to use ML to study such a physical process occurring in the Earth's magnetosphere. The method of ML is not a mere variant of ordinary regression or simple statistical methods. Its magic lies in its ability to truly 'compress' the representation of physical processes. Such hidden representations within the model are our actual pursuit and focus of attention because these represent universal physical laws that can not be discovered in traditional ways.

7.2 Machine learning models of other magnetospheric quantities

In the course of our work, we showed several models but only focused on the electron flux model in Chapter 3. The ring current ions (10s keV to 100s keV) can also be modeled with a similar method [*Li et al.*, 2023]. The model successfully captures the ring current dynamics at 55 keV and 148 keV using measurements of omnidirectional proton fluxes. It also shows that the most important parameters to model the proton flux are SYMH and ASYH, which is consistent with our general physical understanding that those parameters represent longitudinal symmetric and asymmetric components of the ring current, which is itself composed primarily of energetic protons.

Another important physical quantity is the electron density, which affects many processes, including plasma wave generation and propagation, magnetopause stability, and the loss and acceleration of energetic particles. The density measurement outside the plasmasphere as a function of geomagnetic activity can greatly impact the effectiveness of the wave-particle interaction [*Agapitov et al.*, 2019]. *Huang et al.* [2022] use a recurrent model to model the electron density. The recurrent neural network is an artificial neural network widely used for analyzing time series data. It is specifically designed to handle time dependency by processing data in chronological order and we have developed an encoder-decoder model that is based on recurrent neural network architecture. By designing the architecture effectively, we were able to separate the spacecraft orbital variation from the temporal evolution, which is a significant improvement. We applied this model to global total electron density modeling, which was trained on Van Allen Probes observation. The results demonstrate a stable and evident spatial structure of the plasmasphere and plumes, indicating a fairly good performance of our model.

We can use a similar method to model the wave properties as we know the waves play a key role in particle acceleration. Two important waves controlling radiation belt dynamics are hiss wave and chorus wave. *Huang et al.* [2023] use a neural network module that estimates

the wave probability distribution (modeling both the mean μ and standard deviation σ) at a specific location and time to model the hiss wave intensity. *Chu et al.* [2023] use an imbalanced regression measurement method to develop a neural network model of lower-band (LB) chorus waves. Both *Huang et al.* [2023] and *Chu et al.* [2023] employed some manipulations on the training target. Although the methods differ, their starting point is consistent: to minimize the impact of the big uncertainty in spacecraft observations of plasma waves on the model's performance.

7.3 Future work: What is needed in the future?

In this section, I will briefly outline the potential suggestions for future work, developing further the ideas presented in this thesis.

7.3.1 A unified Electron Flux Model: Integrating Diverse Energy Channels and Orbits

Through the previous studies, we successfully established that geomagnetic indices and solar wind parameters can model the electron flux of different energy channels and capture dynamics like rapid enhancement and dropout events. Combined with the feature attribution method in Chapter 4, we are in a position to study physics from theML model now. However, there are some issues that still need to be resolved. The most significant problem is that previous models are trained on individual energy channels. Although the models have good results in each separate energy channel, from a physical perspective, there is a dependency between different energy levels. For instance, high-energy electrons might be accelerated from low-energy electrons through local acceleration, or they could be a result of electrons in a high L shell undergoing radial diffusion. If we can establish an integrated model that the output can directly provide the electron flux energy spectrum instead of electron flux at individual energy levels, we can then study more specific physical processes

and understand how different geomagnetic activities drive these various processes. Similarly, the model's output should be able to directly provide the results of electron flux of different L shells, rather than treating position as an input like all previous models. Moreover, we hope to incorporate more satellite data from different locations, mainly by combining data from LEO and GEO satellites to train the model, making it more robust. The final model should work as follows: given the initial electron flux at time t_0, plus a certain length of time history of geomagnetic indices and solar wind conditions, we should be able to determine the energy spectrum of electron flux at different locations at time t, completely based on the solar wind conditions from time t_0 to t. This will directly compare with and help refine physical models.

7.3.2 AI-based discovery of the governing equations describing radiation belt dynamics

The Fokker-Planck simulation is a partial differential equation that describes the time evolution of electron flux in radiation belt simulations. Typically, FP simulations are used in the following ways: a certain time interval is chosen, and the electron fluxes of a given energy are plotted as a function of time and L-shell. The FP simulation is then run over that time period adding different effect through a set of parameterized diffusion coefficients (e.g. the effects of chorus, electro-magnetic ion cyclotron (EMIC) waves) or changing the boundary conditions until the simulation is verified by one global metric. However, this traditional model of analysis is fairly heuristic and suffers from a number of shortcomings: 1. Boundary conditions are not well controlled and could introduce bias into the simulation. 2. There could be a whole host of similarly performing solutions (i.e., non uniqueness) or indeed there is no guarantee that the form of the Fokker-Planck equation is sufficient to capture all the various physical mechanisms that affect radiation belt dynamics. Thus, we hope to find new ways to help identify the governing equations. The process of discovering a set of PDEs directly from time-series data collected at a number of spatial locations can be illustrated

in a simple way using the PDE functional identification of nonlinear dynamics (PDE-FIND) algorithm [*Brunton et al.*, 2016]. We will use the ML model to reconstruct the electron flux under different dynamics (e.g., decay, wave-particle interaction), which will provide spatial-temporal differentiable, high-resolution PSD results for PDE-discovery. Finally, the PDE discovery approach will attempt to identify what the "real", fundamental, data-driven PDE equation (which optimally describes the evolution of the observed data) looks like, to see which terms are identified in this AI-discovered equation that are missing from the current FP equation, how these terms vary as a function of space and time, and ultimately what physical processes these additional terms correspond to, pointing the way to discovering insights about which physical processes exist that we currently neglect in our simulations or that we may not even be aware of.

7.3.3 Improving Solar wind and Geomagnetic Indices Predictions through Machine Learning

Based on all the studies discussed in this thesis, for real space weather forecasting, we need predictions of solar wind parameters spanning several days in advance. More precisely, we can ask how we can predict the impact of solar activity on Earth in advance. So far, there have been no accurate models for predicting solar activity, nor a model that translates solar image observations to solar wind data, not to mention the fact that there's a distance of 1.5 million kilometers from the usual solar wind observation location - the L1 point - to Earth which could introduce significant errors in itself. Whether we can make progress on these issues will determine if, and how far ahead, we can provide accurate space weather forecasts. We will start with the prediction of solar flares from an active region. Despite the fact that the exact mechanisms initiating solar flares and the elements influencing their intensity remain unclear, numerous studies have demonstrated that solar flares originate from the abrupt discharge of free energy, which occurs due to magnetic reconnection in the coronal field. As the coronal field is influenced by the photospheric magnetic field, the changing

patterns in the photospheric magnetic field could potentially act as markers for identifying the onset of flares and Coronal Mass Ejections (CMEs). Thus, we can use time series data from the magnetic imager together with other observations to attempt to predict the solar flares' location and intensity using a machine-learning model. The outflow can then be input into the traditional magnetohydrodynamic numerical model that simulates the resulting flow evolution to Earth to finally compare with the L1 observations or the Parker Solar Probe observations, which will help correct the ML model.

Compared to the flourishing fields of image recognition, large language models, and other popular ML areas, the application of ML techniques to space physics and space weather prediction is still in its early stages. However, there is no doubt that humanity will eventually venture into space, which means that a deeper understanding of space physics will be necessary in this process. We will easily get a large amount of new data that can be used to build ML models. Here, we have demonstrated a number of applications and identified promising directions for potential future research in this new and exciting area.

Bibliography

Agapitov, O., D. Mourenas, A. Artemyev, G. Hospodarsky, and J. Bonnell (2019), Time scales for electron quasi-linear diffusion by lower-band chorus waves: The effects of ωpe/ωce dependence on geomagnetic activity, *Geophysical Research Letters*, *46*(12), 6178–6187.

Akasofu, S.-I., J. C. Cain, and S. Chapman (1962), The magnetic field of the quiet-time proton belt, *Journal of Geophysical Research*, *67*(7), 2645–2647.

Akiba, T., S. Sano, T. Yanase, T. Ohta, and M. Koyama (2019), Optuna: A next-generation hyperparameter optimization framework, in *Proceedings of the 25th ACM SIGKDD international conference on knowledge discovery & data mining*, pp. 2623–2631.

Albert, J. M. (1993), Cyclotron resonance in an inhomogeneous magnetic field, *Physics of Fluids B: Plasma Physics*, *5*(8), 2744–2750.

Alfven, H. (1950), Cosmical electrodynamics, *International Series of Monographs on Physics*.

Allison, H. J., R. B. Horne, S. A. Glauert, and G. D. Zanna (2017), The magnetic local time distribution of energetic electrons in the radiation belt region, *Journal of Geophysical Research: Space Physics*, *122*(8), 8108–8123, doi:10.1002/2017ja024084.

Allison, H. J., Y. Y. Shprits, I. S. Zhelavskaya, D. Wang, and A. G. Smirnov (2021), Gyroresonant wave-particle interactions with chorus waves during extreme depletions of plasma density in the van allen radiation belts, *Science Advances*, *7*(5), eabc0380.

Angelopoulos, V. (2009), *The THEMIS mission*, Springer.

Angelopoulos, V., A. Runov, X.-Z. Zhou, D. Turner, S. Kiehas, S.-S. Li, and I. Shinohara (2013), Electromagnetic energy conversion at reconnection fronts, *science*, *341*(6153), 1478–1482.

Aryan, H., J. Bortnik, N. P. Meredith, R. B. Horne, D. G. Sibeck, and M. A. Balikhin (2021), Multi-parameter chorus and plasmaspheric hiss wave models, *Journal of Geophysical Research: Space Physics*, *126*(1), e2020JA028,403.

Ayala Solares, J. R., H.-L. Wei, R. J. Boynton, S. N. Walker, and S. A. Billings (2016), Modeling and prediction of global magnetic disturbance in near-earth space: A case study for kp index using narx models, *Space Weather*, *14*(10), 899–916, doi:https://doi.org/10.1002/2016SW001463.

Baker, D. (1998), What is space weather?, *Advances in Space Research*, *22*(1), 7–16.

Baker, D. N. (2001), Satellite anomalies due to space storms: The effects of space weather on spacecraft systems and subsystems, *Space storms and space weather hazards*, pp. 285–311.

Baker, D. N., and L. J. Lanzerotti (2016), Resource letter sw1: Space weather, *American Journal of Physics*, *84*(3), 166–180.

Baker, D. N., P. R. Higbie, R. D. Belian, and E. W. Hones (1979), Do Jovian electrons influence the terrestrial outer radiation zone?, *Geophysical Research Letters*, *6*(6), 531–534, doi:10.1029/gl006i006p00531.

Baker, D. N., S. Kanekal, V. Hoxie, S. Batiste, M. Bolton, X. Li, S. Elkington, S. Monk, R. Reukauf, S. Steg, et al. (2012), The relativistic electron-proton telescope (rept) instrument on board the radiation belt storm probes (rbsp) spacecraft: Characterization of earth's radiation belt high-energy particle populations, in *The van allen probes mission*, pp. 337–381, Springer.

Baker, D. N., A. N. Jaynes, V. C. Hoxie, R. M. Thorne, J. C. Foster, X. Li, J. F. Fennell, J. R. Wygant, S. G. Kanekal, P. J. Erickson, W. Kurth, W. Li, Q. Ma, Q. Schiller, L. Blum, D. M. Malaspina, A. Gerrard, and L. J. Lanzerotti (2014), An impenetrable barrier to ultrarelativistic electrons in the Van Allen radiation belts, *Nature*, *515*(7528), 531–534, doi:10.1038/nature13956.

Baker, D. N., V. Hoxie, H. Zhao, A. N. Jaynes, S. Kanekal, X. Li, and S. Elkington (2019), Multiyear measurements of radiation belt electrons: Acceleration, transport, and loss, *Journal of Geophysical Research: Space Physics*, *124*(4), 2588–2602.

Balikhin, M. A., R. J. Boynton, S. N. Walker, J. E. Borovsky, S. A. Billings, and H.-L. Wei (2011), Using the narmax approach to model the evolution of energetic electrons fluxes at geostationary orbit, *Geophysical Research Letters*, *38*(18).

Bergstra, J., R. Bardenet, Y. Bengio, and B. Kégl (2011), Algorithms for hyper-parameter optimization, *Advances in neural information processing systems*, *24*.

Bergstra, J., D. Yamins, and D. Cox (2013), Making a science of model search: Hyperparameter optimization in hundreds of dimensions for vision architectures, in *Proceedings of the 30th International Conference on Machine Learning*, *Proceedings of Machine Learning Research*, vol. 28, edited by S. Dasgupta and D. McAllester, pp. 115–123, PMLR, Atlanta, Georgia, USA.

Blake, J., P. Carranza, S. Claudepierre, J. Clemmons, W. Crain, Y. Dotan, J. Fennell, F. Fuentes, R. Galvan, J. George, et al. (2014), The magnetic electron ion spectrometer (mageis) instruments aboard the radiation belt storm probes (rbsp) spacecraft, *The van Allen probes mission*, pp. 383–421.

Bortnik, J., and R. Thorne (2007), The dual role of elf/vlf chorus waves in the acceleration and precipitation of radiation belt electrons, *Journal of Atmospheric and Solar-Terrestrial Physics*, *69*(3), 378–386.

Bortnik, J., R. Thorne, and U. S. Inan (2008), Nonlinear interaction of energetic electrons with large amplitude chorus, *Geophysical Research Letters*, *35*(21).

Bortnik, J., L. Chen, W. Li, R. Thorne, and R. Horne (2011), Modeling the evolution of chorus waves into plasmaspheric hiss, *Journal of Geophysical Research: Space Physics*, *116*(A8).

Bortnik, J., W. Li, R. Thorne, and V. Angelopoulos (2016a), A unified approach to inner magnetospheric state prediction, *Journal of Geophysical Research: Space Physics*, *121*(3), 2423–2430.

Bortnik, J., W. Li, R. M. Thorne, and V. Angelopoulos (2016b), A unified approach to inner magnetospheric state prediction, *Journal of Geophysical Research: Space Physics*, *121*(3), 2423–2430, doi:10.1002/2015ja021733.

Bortnik, J., X. Chu, Q. Ma, W. Li, X. Zhang, R. M. Thorne, V. Angelopoulos, R. E. Denton, C. A. Kletzing, G. B. Hospodarsky, H. E. Spence, G. D. Reeves, S. G. Kanekal, and D. N. Baker (2018), Chapter 11 - artificial neural networks for determining magnetospheric conditions, in *Machine Learning Techniques for Space Weather*, edited by E. Camporeale, S. Wing, and J. R. Johnson, pp. 279–300, Elsevier, doi: https://doi.org/10.1016/B978-0-12-811788-0.00011-1.

Boyd, A., G. Reeves, H. Spence, H. Funsten, B. Larsen, R. Skoug, J. Blake, J. Fennell, S. Claudepierre, D. Baker, et al. (2019), Rbsp-ect combined spin-averaged electron flux data product, *Journal of Geophysical Research: Space Physics*, *124*(11), 9124–9136.

Brautigam, D. H., and J. T. Bell (1995), Crresele documentation, *Rep. PL-TR-95*, *2128*.

Brice, N. M. (1967), Bulk motion of the magnetosphere, *Journal of Geophysical Research*, *72*(21), 5193–5211.

Brizard, A. J. (2013), Beyond linear gyrocenter polarization in gyrokinetic theory, *Physics of Plasmas*, *20*(9).

Brunton, S. L., J. L. Proctor, and J. N. Kutz (2016), Discovering governing equations from data by sparse identification of nonlinear dynamical systems, *Proceedings of the national academy of sciences*, *113*(15), 3932–3937.

Burch, J. (2000), Image mission overview, *Space Science Reviews*, *91*(1-2), 1–14.

Burtis, W., and R. Helliwell (1969), Banded chorus—a new type of vlf radiation observed in the magnetosphere by ogo 1 and ogo 3, *Journal of Geophysical Research*, *74*(11), 3002–3010.

Camporeale, E. (2019), The challenge of machine learning in space weather: Nowcasting and forecasting, *Space Weather*, *17*(8), 1166–1207.

Carpenter, D. L. (1963), Whistler measurements of electron density and magnetic field strength in the remote magnetosphere, *Journal of Geophysical Research*, *68*(12), 3727–3730.

Chappell, C., K. Harris, and G. Sharp (1971), The dayside of the plasmasphere, *Journal of Geophysical Research*, *76*(31), 7632–7647.

Chen, F. F. (2012), *Introduction to plasma physics*, Springer Science & Business Media.

Chen, H., S. Lundberg, and S.-I. Lee (2021), Explaining models by propagating shapley values of local components, in *Explainable AI in Healthcare and Medicine*, pp. 261–270, Springer.

Choi, H.-S., J. Lee, K.-S. Cho, Y.-S. Kwak, I.-H. Cho, Y.-D. Park, Y.-H. Kim, D. N. Baker, G. D. Reeves, and D.-K. Lee (2011), Analysis of geo spacecraft anomalies: Space weather relationships, *Space weather*, *9*(6).

Chu, X., J. Bortnik, W. Li, Q. Ma, R. Denton, C. Yue, V. Angelopoulos, R. M. Thorne, F. Darrouzet, P. Ozhogin, C. A. Kletzing, Y. Wang, and J. Menietti (2017a), A neural network model of three-dimensional dynamic electron density in the inner magnetosphere, *Journal of Geophysical Research: Space Physics*, *122*(9), 9183–9197, doi: 10.1002/2017ja024464.

Chu, X., J. Bortnik, W. Li, Q. Ma, V. Angelopoulos, and R. M. Thorne (2017b), Erosion and refilling of the plasmasphere during a geomagnetic storm modeled by a neu-

ral network, *Journal of Geophysical Research: Space Physics*, *122*(7), 7118–7129, doi: 10.1002/2017ja023948.

Chu, X., D. Ma, J. Bortnik, W. K. Tobiska, A. Cruz, S. D. Bouwer, H. Zhao, Q. Ma, K. Zhang, D. N. Baker, et al. (2021), Relativistic electron model in the outer radiation belt using a neural network approach, *Space Weather*, *19*(12), e2021SW002,808.

Chu, X., J. Bortnik, W. Li, X.-C. Shen, Q. Ma, D. Ma, D. Malaspina, and S. Huang (2023), Distribution and evolution of chorus waves modeled by a neural network: The importance of imbalanced regression, *Space Weather*, *21*(10), e2023SW003,524.

Claudepierre, S. G., and T. P. O'Brien (2020), Specifying high-altitude electrons using low-altitude leo systems: The shells model, *Space Weather*, *18*(3), e2019SW002,402.

Claudepierre, S. G., T. P. O'Brien, J. B. Blake, J. F. Fennell, J. L. Roeder, J. H. Clemmons, M. D. Looper, J. E. Mazur, T. M. Mulligan, H. E. Spence, G. D. Reeves, R. H. W. Friedel, M. G. Henderson, and B. A. Larsen (2015), A background correction algorithm for Van Allen Probes MagEIS electron flux measurements, *Journal of Geophysical Research: Space Physics*, *120*(7), 5703–5727, doi:10.1002/2015ja021171.

Claudepierre, S. G., T. P. O'Brien, M. D. Looper, J. B. Blake, J. F. Fennell, J. L. Roeder, J. H. Clemmons, J. E. Mazur, D. L. Turner, G. D. Reeves, and H. E. Spence (2019), A Revised Look at Relativistic Electrons in the Earth's Inner Radiation Zone and Slot Region, *Journal of Geophysical Research: Space Physics*, *124*(2), 934–951, doi:10.1029/2018ja026349.

Claudepierre, S. G., Q. Ma, J. Bortnik, T. P. O'Brien, J. F. Fennell, and J. B. Blake (2020a), Empirically Estimated Electron Lifetimes in the Earth's Radiation Belts: Van Allen Probe Observations, *Geophysical Research Letters*, *47*(3), e2019GL086,053, doi: 10.1029/2019gl086053.

Claudepierre, S. G., Q. Ma, J. Bortnik, T. P. O'Brien, J. F. Fennell, and J. B. Blake (2020b), Empirically Estimated Electron Lifetimes in the Earth's Radiation Belts: Comparison With Theory, *Geophysical Research Letters*, *47*(3), e2019GL086,056, doi:10.1029/2019gl086056.

Cook, G. (1965), Satellite drag coefficients, *Planetary and Space Science*, *13*(10), 929–946.

Cybenko, G. (1989), Approximation by superpositions of a sigmoidal function, *Mathematics of control, signals and systems*, *2*(4), 303–314.

Dang, T., X. Li, B. Luo, R. Li, B. Zhang, K. Pham, D. Ren, X. Chen, J. Lei, and Y. Wang (2022), Unveiling the space weather during the starlink satellites destruction event on 4 february 2022, *Space weather*, *20*(8), e2022SW003,152.

Dessler, A. J., and E. N. Parker (1959), Hydromagnetic theory of geomagnetic storms, *Journal of Geophysical Research*, *64*(12), 2239–2252.

Drozdov, A., Y. Shprits, K. Orlova, A. C. Kellerman, D. Subbotin, D. N. Baker, H. E. Spence, and G. Reeves (2015), Energetic, relativistic, and ultrarelativistic electrons: Comparison of long-term verb code simulations with van allen probes measurements, *Journal of Geophysical Research: Space Physics*, *120*(5), 3574–3587.

Dungey, J. W. (1961), Interplanetary magnetic field and the auroral zones, *Physical Review Letters*, *6*(2), 47.

Fennell, J. F., H. Koons, J. Roeder, and J. Blake (2001), Spacecraft charging: Observations and relationship to satellite anomalies, *Tech. rep.*, AEROSPACE CORP EL SEGUNDO CA LAB OPERATIONS.

Floridi, L., and M. Chiriatti (2020), Gpt-3: Its nature, scope, limits, and consequences, *Minds and Machines*, *30*, 681–694.

Fokker, A. D. (1914), Die mittlere energie rotierender elektrischer dipole im strahlungsfeld, *Annalen der Physik*, *348*(5), 810–820.

Ginet, G. P., T. P. O'Brien, S. L. Huston, W. R. Johnston, T. B. Guild, R. Friedel, C. D. Lindstrom, C. J. Roth, P. Whelan, R. A. Quinn, D. Madden, S. Morley, and Y.-J. Su (2013), AE9, AP9 and SPM: New Models for Specifying the Trapped Energetic Particle and Space Plasma Environment, *Space Science Reviews*, *179*(1-4), 579–615, doi:10.1007/s11214-013-9964-y.

Glauert, S. A., R. B. Horne, and N. P. Meredith (2014), Three-dimensional electron radiation belt simulations using the bas radiation belt model with new diffusion models for chorus, plasmaspheric hiss, and lightning-generated whistlers, *Journal of Geophysical Research: Space Physics*, *119*(1), 268–289.

Goldstein, J., B. Sandel, M. Thomsen, M. Spasojević, and P. Reiff (2004), Simultaneous remote sensing and in situ observations of plasmaspheric drainage plumes, *Journal of Geophysical Research: Space Physics*, *109*(A3).

Gonzalez, W., J.-A. Joselyn, Y. Kamide, H. W. Kroehl, G. Rostoker, B. T. Tsurutani, and V. Vasyliunas (1994), What is a geomagnetic storm?, *Journal of Geophysical Research: Space Physics*, *99*(A4), 5771–5792.

Gonzalez, W. D., and B. T. Tsurutani (1987), Criteria of interplanetary parameters causing intense magnetic storms (Dst < -100 nT), *Planetary and Space Science*, *35*(9), 1101–1109.

Gringauz, K. (1963), The structure of the ionized gas envelope of earth from direct measurements in the ussr of local charged particle concentrations, *Planetary and Space Science*, *11*(3), 281–296.

Hands, A., K. Ryden, C. Underwood, D. Rodgers, and H. Evans (2015), A New Model of

Outer Belt Electrons for Dielectric Internal Charging (MOBE-DIC), *IEEE Transactions on Nuclear Science*, *62*(6), 2767–2775, doi:10.1109/tns.2015.2475134.

Hargreaves, J. K. (1992), *The solar-terrestrial environment: an introduction to geospace-the science of the terrestrial upper atmosphere, ionosphere, and magnetosphere*, Cambridge university press.

He, K., H. Fan, Y. Wu, S. Xie, and R. Girshick (2020), Momentum contrast for unsupervised visual representation learning, in *Proceedings of the IEEE/CVF conference on computer vision and pattern recognition*, pp. 9729–9738.

Helliwell, R. A. (2014), *Whistlers and related ionospheric phenomena*, Courier Corporation.

Horne, R., and R. Thorne (2003), Relativistic electron acceleration and precipitation during resonant interactions with whistler-mode chorus, *Geophysical research letters*, *30*(10).

Horne, R. B., and R. M. Thorne (1998), Potential waves for relativistic electron scattering and stochastic acceleration during magnetic storms, *Geophysical Research Letters*, *25*(15), 3011–3014.

Horne, R. B., S. A. Glauert, and R. M. Thorne (2003), Resonant diffusion of radiation belt electrons by whistler-mode chorus, *Geophysical Research Letters*, *30*(9), doi:https://doi.org/10.1029/2003GL016963.

Horne, R. B., R. M. Thorne, Y. Y. Shprits, N. P. Meredith, S. A. Glauert, A. J. Smith, S. G. Kanekal, D. N. Baker, M. J. Engebretson, J. L. Posch, et al. (2005), Wave acceleration of electrons in the van allen radiation belts, *Nature*, *437*(7056), 227–230.

Hua, M., J. Bortnik, X. Chu, H. Aryan, and Q. Ma (2022a), Unraveling the critical geomagnetic conditions controlling the upper limit of electron fluxes in the earth's outer radiation belt, *Geophysical Research Letters*, *49*(22), e2022GL101,096.

Hua, M., J. Bortnik, A. C. Kellerman, E. Camporeale, and Q. Ma (2022b), Ensemble modeling of radiation belt electron flux decay following a geomagnetic storm: Dependence on key input parameters, *Space Weather*, *20*(8), e2022SW003,051.

Hua, M., J. Bortnik, and Q. Ma (2022c), Upper limit of outer radiation belt electron acceleration driven by whistler-mode chorus waves, *Geophysical Research Letters*, *49*(15), e2022GL099,618.

Hua, M., J. Bortnik, H. E. Spence, and G. D. Reeves (2023a), Testing the key processes that accelerate outer radiation belt relativistic electrons during geomagnetic storms, *Frontiers in Astronomy and Space Sciences*, *10*, 1168,636.

Hua, M., J. Bortnik, A. C. Kellerman, E. Camporeale, and Q. Ma (2023b), Ensemble modeling of radiation belt electron acceleration by chorus waves: Dependence on key input parameters, *Space Weather*, *21*(3), e2022SW003,234.

Huang, S., W. Li, X.-C. Shen, Q. Ma, X. Chu, D. Ma, J. Bortnik, L. Capannolo, Y. Nishimura, and J. Goldstein (2022), Application of recurrent neural network to modeling earth's global electron density, *Journal of Geophysical Research: Space Physics*, *127*(9), e2022JA030,695.

Huang, S., W. Li, Q. Ma, X.-C. Shen, L. Capannolo, M. Hanzelka, X. Chu, D. Ma, J. Bortnik, and S. Wing (2023), Deep learning model of hiss waves in the plasmasphere and plumes and their effects on radiation belt electrons, *Frontiers in Astronomy and Space Sciences*, *10*.

Inan, U., T. Bell, J. Bortnik, and J. Albert (2003), Controlled precipitation of radiation belt electrons, *Journal of Geophysical Research: Space Physics*, *108*(A5).

Ioffe, S., and C. Szegedy (2015), Batch normalization: Accelerating deep network training by reducing internal covariate shift, in *International conference on machine learning*, pp. 448–456, PMLR.

Iong, D., Y. Chen, G. Toth, S. Zou, T. Pulkkinen, J. Ren, E. Camporeale, and T. Gombosi (2022), New findings from explainable sym-h forecasting using gradient boosting machines, *Space Weather*, *n/a*(n/a), e2021SW002,928, doi:https://doi.org/10.1029/2021SW002928, e2021SW002928 2021SW002928.

Jaynes, A. N., D. N. Baker, H. J. Singer, J. V. Rodriguez, T. Loto'aniu, A. Ali, S. R. Elkington, X. Li, S. G. Kanekal, S. G. Claudepierre, et al. (2015), Source and seed populations for relativistic electrons: Their roles in radiation belt changes, *Journal of Geophysical Research: Space Physics*, *120*(9), 7240–7254.

Jordanova, V. K., R. M. Thorne, W. Li, and Y. Miyoshi (2010), Excitation of whistler mode chorus from global ring current simulations, *Journal of Geophysical Research: Space Physics*, *115*(A5), doi:https://doi.org/10.1029/2009JA014810.

Katsavrias, C., I. A. Daglis, and W. Li (2019), On the statistics of acceleration and loss of relativistic electrons in the outer radiation belt: A superposed epoch analysis, *Journal of Geophysical Research: Space Physics*, *124*(4), 2755–2768.

Kennel, C., and F. Engelmann (1966), Velocity space diffusion from weak plasma turbulence in a magnetic field, *The Physics of Fluids*, *9*(12), 2377–2388.

Kennel, C. F., and H. Petschek (1966), Limit on stably trapped particle fluxes, *Journal of Geophysical Research*, *71*(1), 1–28.

Kim, H.-J., and A. A. Chan (1997), Fully adiabatic changes in storm time relativistic electron fluxes, *Journal of Geophysical Research: Space Physics*, *102*(A10), 22,107–22,116, doi: https://doi.org/10.1029/97JA01814.

Kitamura, N. (2018), Magnetosphere continuously eats solar wind with a huge mouth.

Kivelson, M. G., and C. T. Russell (1995), *Introduction to space physics*, Cambridge university press.

Klobuchar, J. A. (1987), Ionospheric time-delay algorithm for single-frequency gps users, *IEEE Transactions on aerospace and electronic systems*, (3), 325–331.

Kohonen, T. (1988), An introduction to neural computing, *Neural networks*, *1*(1), 3–16.

Koskinen, H. E., E. K. Kilpua, H. E. Koskinen, and E. K. Kilpua (2022a), Radiation belts and their environment, *Physics of Earth's Radiation Belts: Theory and Observations*, pp. 1–25.

Koskinen, H. E., E. K. Kilpua, H. E. Koskinen, and E. K. Kilpua (2022b), Charged particles in near-earth space, *Physics of Earth's Radiation Belts: Theory and Observations*, pp. 27–61.

Kuhn, M., K. Johnson, et al. (2013), *Applied predictive modeling*, vol. 26, Springer.

Landau, L. D., and E. M. Lifshitz (2013), *Course of theoretical physics*, Elsevier.

Lanzerotti, L., C. Breglia, D. Maurer, G. Johnson III, and C. Maclennan (1998), Studies of spacecraft charging on a geosynchronous telecommunications satellite, *Advances in Space Research*, *22*(1), 79–82.

Lanzerotti, L. J. (2001), Space weather effects on technologies, *Washington DC American Geophysical Union Geophysical Monograph Series*, *125*, 11–22.

LeCun, Y., Y. Bengio, and G. Hinton (2015), Deep learning, *nature*, *521*(7553), 436–444.

Lenchek, A., S. Singer, and R. Wentworth (1961), Geomagnetically trapped electrons from cosmic ray albedo neutrons, *Journal of Geophysical Research*, *66*(12), 4027–4046.

Li, J., J. Bortnik, X. An, W. Li, V. Angelopoulos, R. M. Thorne, C. T. Russell, B. Ni, X. Shen, W. S. Kurth, et al. (2019), Origin of two-band chorus in the radiation belt of earth, *Nature communications*, *10*(1), 4672.

Li, J., J. Bortnik, X. Chu, D. Ma, S. Tian, C.-P. Wang, J. W. Manweiler, and L. J. Lanzerotti (2023), Modeling ring current proton fluxes using artificial neural network and van allen probe measurements, *Space Weather*, *21*(5), e2022SW003,257.

Li, W., and M. Hudson (2019), Earth's van allen radiation belts: From discovery to the van allen probes era, *Journal of Geophysical Research: Space Physics*, *124*(11), 8319–8351.

Li, W., R. Thorne, V. Angelopoulos, J. Bortnik, C. M. Cully, B. Ni, O. LeContel, A. Roux, U. Auster, and W. Magnes (2009), Global distribution of whistler-mode chorus waves observed on the themis spacecraft, *Geophysical Research Letters*, *36*(9).

Li, W., R. M. Thorne, Y. Nishimura, J. Bortnik, V. Angelopoulos, J. P. McFadden, D. E. Larson, J. W. Bonnell, O. Le Contel, A. Roux, and U. Auster (2010), Themis analysis of observed equatorial electron distributions responsible for the chorus excitation, *Journal of Geophysical Research: Space Physics*, *115*(A6), doi:https://doi.org/10.1029/2009JA014845.

Li, W., J. Bortnik, R. Thorne, and V. Angelopoulos (2011), Global distribution of wave amplitudes and wave normal angles of chorus waves using themis wave observations, *Journal of Geophysical Research: Space Physics*, *116*(A12).

Li, W., R. M. Thorne, Q. Ma, B. Ni, J. Bortnik, D. N. Baker, H. E. Spence, G. D. Reeves, S. G. Kanekal, J. C. Green, C. A. Kletzing, W. S. Kurth, G. B. Hospodarsky, J. B. Blake, J. F. Fennell, and S. G. Claudepierre (2014), Radiation belt electron acceleration by chorus waves during the 17 March 2013 storm, *Journal of Geophysical Research: Space Physics*, *119*(6), 4681–4693, doi:10.1002/2014ja019945.

Li, W., O. Santolik, J. Bortnik, R. Thorne, C. Kletzing, W. Kurth, and G. Hospodarsky (2016), New chorus wave properties near the equator from van allen probes wave observations, *Geophysical Research Letters*, *43*(10), 4725–4735.

Li, X., D. Baker, S. Kanekal, M. Looper, and M. Temerin (2001), Long term measurements of radiation belts by sampex and their variations, *Geophysical Research Letters*, *28*(20), 3827–3830.

Li, X., D. Baker, T. O'Brien, L. Xie, and Q. Zong (2006), Correlation between the inner edge of outer radiation belt electrons and the innermost plasmapause location, *Geophysical research letters*, *33*(14).

Li, X., K. S. Oh, and M. Temerin (2007a), Prediction of the al index using solar wind parameters, *Journal of Geophysical Research: Space Physics*, *112*(A6), doi:https://doi.org/10.1029/2006JA011918.

Li, X., K. S. Oh, and M. Temerin (2007b), Prediction of the al index using solar wind parameters, *Journal of Geophysical Research: Space Physics*, *112*(A6).

Lima, R. P. d., Y. Chen, and Y. Lin (2020), Forecasting Megaelectron-Volt Electrons Inside Earth's Outer Radiation Belt: PreMevE 2.0 Based on Supervised Machine Learning Algorithms, *Space Weather*, *18*(2), doi:10.1029/2019sw002399.

Lipton, Z. C. (2018), The mythos of model interpretability: In machine learning, the concept of interpretability is both important and slippery., *Queue*, *16*(3), 31–57.

Liu, W., W. Tu, X. Li, T. Sarris, Y. Khotyaintsev, H. Fu, H. Zhang, and Q. Shi (2016), On the calculation of electric diffusion coefficient of radiation belt electrons with in situ electric field measurements by themis, *Geophysical Research Letters*, *43*(3), 1023–1030.

Loto'Aniu, T., H. Singer, C. Waters, V. Angelopoulos, I. Mann, S. Elkington, and J. Bonnell (2010), Relativistic electron loss due to ultralow frequency waves and enhanced outward radial diffusion, *Journal of Geophysical Research: Space Physics*, *115*(A12).

Lundberg, S. M., and S.-I. Lee (2017), A unified approach to interpreting model predictions, *Advances in neural information processing systems*, *30*.

Lundberg, S. M., G. G. Erion, and S.-I. Lee (2018), Consistent individualized feature attribution for tree ensembles, *arXiv preprint arXiv:1802.03888*.

Luo, B., X. Li, M. Temerin, and S. Liu (2013), Prediction of the au, al, and ae indices using solar wind parameters, *Journal of Geophysical Research: Space Physics*, *118*(12), 7683–7694, doi:https://doi.org/10.1002/2013JA019188.

Lyons, L. R., and R. M. Thorne (1973), Equilibrium structure of radiation belt electrons, *Journal of Geophysical Research*, *78*(13), 2142–2149.

Lyons, L. R., and D. J. Williams (2013), *Quantitative aspects of magnetospheric physics*, vol. 23, Springer Science & Business Media.

Ma, D. (2023), Machine learning interpretability of outer radiation belt enhancement & depletion events [dataset], doi:10.5281/zenodo.8347502.

Ma, D., X. Chu, J. Bortnik, S. G. Claudepierre, W. K. Tobiska, A. Cruz, S. D. Bouwer, J. F. Fennell, and J. B. Blake (2022), Modeling the dynamic variability of sub-relativistic outer radiation belt electron fluxes using machine learning, *Space Weather*, *20*(8), e2022SW003,079.

Ma, D., J. Bortnik, X. Chu, S. G. Claudepierre, Q. Ma, and A. Kellerman (2023), Opening the black box of the radiation belt machine learning model, *Space Weather*, *21*(4), e2022SW003,339.

Ma, D., J. Bortnik, Q. Ma, M. Hua, and X. Chu (2024), Machine learning interpretability of outer radiation belt enhancement and depletion events, *Geophysical Research Letters*, *51*(1), e2023GL106,049.

Ma, Q., B. Ni, X. Tao, and R. Thorne (2012), Evolution of the plasma sheet electron pitch angle distribution by whistler-mode chorus waves in non-dipole magnetic fields, in *Annales Geophysicae*, vol. 30, pp. 751–760, Copernicus Publications Göttingen, Germany.

Ma, Q., W. Li, R. Thorne, B. Ni, C. Kletzing, W. Kurth, G. Hospodarsky, G. Reeves, M. Henderson, H. E. Spence, et al. (2015), Modeling inward diffusion and slow decay of energetic electrons in the earth's outer radiation belt, *Geophysical Research Letters*, *42*(4), 987–995.

Ma, Q., D. Mourenas, W. Li, A. Artemyev, and R. M. Thorne (2017), Vlf waves from ground-based transmitters observed by the van allen probes: Statistical model and effects on plasmaspheric electrons, *Geophysical Research Letters*, *44*(13), 6483–6491.

Ma, Q., W. Li, J. Bortnik, R. Thorne, X. Chu, L. Ozeke, G. D. Reeves, C. Kletzing, W. Kurth, G. Hospodarsky, et al. (2018), Quantitative evaluation of radial diffusion and local acceleration processes during gem challenge events, *Journal of Geophysical Research: Space Physics*, *123*(3), 1938–1952.

Malaspina, D. M., A. N. Jaynes, C. Boulé, J. Bortnik, S. A. Thaller, R. E. Ergun, C. A. Kletzing, and J. R. Wygant (2016), The distribution of plasmaspheric hiss wave power with respect to plasmapause location, *Geophysical Research Letters*, *43*(15), 7878–7886.

Malaspina, D. M., A. Ukhorskiy, X. Chu, and J. Wygant (2018), A census of plasma waves and structures associated with an injection front in the inner magnetosphere, *Journal of Geophysical Research: Space Physics*, *123*(4), 2566–2587.

Mauk, B., N. J. Fox, S. Kanekal, R. Kessel, D. Sibeck, and a. A. Ukhorskiy (2014), Science objectives and rationale for the radiation belt storm probes mission, *The van Allen probes mission*, pp. 3–27.

Mauk, B. H., N. J. Fox, S. G. Kanekal, R. L. Kessel, D. G. Sibeck, and A. Ukhorskiy (2013), Science Objectives and Rationale for the Radiation Belt Storm Probes Mission, *Space Science Reviews*, *179*(1-4), 3–27, doi:10.1007/s11214-012-9908-y.

McPherron, R. L., T.-S. Hsu, and X. Chu (2015), An optimum solar wind coupling function for the al index, *Journal of Geophysical Research: Space Physics*, *120*(4), 2494–2515.

Meredith, N. P., M. Cain, R. B. Horne, R. M. Thorne, D. Summers, and R. R. Anderson (2003), Evidence for chorus-driven electron acceleration to relativistic energies from a survey of geomagnetically disturbed periods, *Journal of Geophysical Research: Space Physics*, *108*(A6).

Meredith, N. P., R. B. Horne, R. M. Thorne, D. Summers, and R. R. Anderson (2004), Substorm dependence of plasmaspheric hiss, *Journal of Geophysical Research: Space Physics*, *109*(A6), n/a–n/a, doi:10.1029/2004JA010387, a06209.

Merkin, V. G., E. V. Panov, K. Sorathia, and A. Y. Ukhorskiy (2019), Contribution of bursty bulk flows to the global dipolarization of the magnetotail during an isolated substorm, *Journal of Geophysical Research: Space Physics*, *124*(11), 8647–8668.

Mitchell, D., L. Lanzerotti, C. Kim, M. Stokes, G. Ho, S. Cooper, A. Ukhorskiy, J. Manweiler, S. Jaskulek, D. Haggerty, et al. (2014), Radiation belt storm probes ion composition experiment (rbspice), *The van Allen probes mission*, pp. 263–308.

Miyoshi, Y., K. Sakaguchi, K. Shiokawa, D. Evans, J. Albert, M. Connors, and V. Jordanova (2008), Precipitation of radiation belt electrons by emic waves, observed from ground and space, *Geophysical Research Letters*, *35*(23).

Mourenas, D., A. Artemyev, and X.-J. Zhang (2019), Impact of significant time-integrated geomagnetic activity on 2-mev electron flux, *Journal of Geophysical Research: Space Physics*, *124*(6), 4445–4461.

Nair, V., and G. E. Hinton (2010), Rectified linear units improve restricted boltzmann machines, in *Proceedings of the 27th international conference on machine learning (ICML-10)*, pp. 807–814.

Ni, B., R. M. Thorne, Y. Y. Shprits, and J. Bortnik (2008), Resonant scattering of plasma sheet electrons by whistler-mode chorus: Contribution to diffuse auroral precipitation, *Geophysical Research Letters*, *35*(11).

Øieroset, M., T. Phan, M. Fujimoto, R. Lin, and R. Lepping (2001), In situ detection of collisionless reconnection in the earth's magnetotail, *Nature*, *412*(6845), 414–417.

Ozeke, L., I. Mann, S. Claudepierre, M. Henderson, S. Morley, K. Murphy, L. Olifer, H. Spence, and D. Baker (2019), The march 2015 superstorm revisited: Phase space density profiles and fast ulf wave diffusive transport, *Journal of Geophysical Research: Space Physics*, *124*(2), 1143–1156.

Ozeke, L., I. Mann, L. Olifer, K. Dufresne, S. Morley, S. Claudepierre, K. Murphy, H. Spence, D. Baker, and A. Degeling (2020), Rapid outer radiation belt flux dropouts and fast acceleration during the march 2015 and 2013 storms: The role of ultra-low frequency wave transport from a dynamic outer boundary, *Journal of Geophysical Research: Space Physics*, *125*(2), e2019JA027,179.

Parker, E. (1965), Dynamical theory of the solar wind, *Space Science Reviews*, *4*(5-6), 666–708.

Reeves, G., T. Fritz, T. Cayton, and R. Belian (1990), Multi-satellite measurements of the substorm injection region, *Geophysical Research Letters*, *17*(11), 2015–2018.

Reeves, G., K. McAdams, R. Friedel, and T. O'brien (2003), Acceleration and loss of relativistic electrons during geomagnetic storms, *Geophysical Research Letters*, *30*(10).

Reeves, G., H. E. Spence, M. Henderson, S. Morley, R. Friedel, H. Funsten, D. Baker, S. Kanekal, J. Blake, J. Fennell, et al. (2013), Electron acceleration in the heart of the van allen radiation belts, *Science*, *341*(6149), 991–994.

Reeves, G. D., Y. Chen, G. S. Cunningham, R. W. H. Friedel, M. G. Henderson, V. K. Jordanova, J. Koller, S. K. Morley, M. F. Thomsen, and S. Zaharia (2012), Dynamic radiation environment assimilation model: Dream, *Space Weather*, *10*(3), doi:https://doi.org/10.1029/2011SW000729.

Reeves, G. D., R. H. W. Friedel, B. A. Larsen, R. M. Skoug, H. O. Funsten, S. G. Claudepierre, J. F. Fennell, D. L. Turner, M. H. Denton, H. E. Spence, J. B. Blake, and D. N. Baker (2016), Energy-dependent dynamics of keV to MeV electrons in the inner zone, outer zone, and slot regions, *Journal of Geophysical Research: Space Physics*, *121*(1), 397–412, doi:10.1002/2015ja021569.

Ribeiro, M. T., S. Singh, and C. Guestrin (2016), " why should i trust you?" explaining the predictions of any classifier, in *Proceedings of the 22nd ACM SIGKDD international conference on knowledge discovery and data mining*, pp. 1135–1144.

Roederer, J. G., and H. Zhang (2016), *Dynamics of magnetically trapped particles*, Springer.

Rostoker, G., S.-I. Akasofu, J. Foster, R. Greenwald, Y. Kamide, K. Kawasaki, A. Lui, R. McPherron, and C. Russell (1980), Magnetospheric substorms—definition and signatures, *Journal of Geophysical Research: Space Physics*, *85*(A4), 1663–1668.

Samuel, A. L. (1959), Some studies in machine learning using the game of checkers, *IBM Journal of research and development*, *3*(3), 210–229.

Sawyer, D. M., and J. I. Vette (1976), AP-8 trapped proton environment for solar maximum and solar minimum, *Nasa Sti/Recon Technical Report N*, *77*, 18,983.

Schiller, Q., X. Li, L. Blum, W. Tu, D. L. Turner, and J. Blake (2014), A nonstorm time enhancement of relativistic electrons in the outer radiation belt, *Geophysical Research Letters*, *41*(1), 7–12.

Schwenn, R. (2006), Space weather: The solar perspective, *Living reviews in solar physics*, *3*(1), 1–72.

Shapley, L. S. (1953), A value for n-person games, in *Contributions to the Theory of Games II*, edited by H. W. Kuhn and A. W. Tucker, pp. 307–317, Princeton University Press, Princeton.

Shprits, Y. Y., R. M. Thorne, R. Friedel, G. D. Reeves, J. Fennell, D. N. Baker, and S. G. Kanekal (2006), Outward radial diffusion driven by losses at magnetopause, *Journal of Geophysical Research: Space Physics*, *111*(A11), doi:https://doi.org/10.1029/2006JA011657.

Shprits, Y. Y., D. Subbotin, and B. Ni (2009), Evolution of electron fluxes in the outer radiation belt computed with the verb code, *Journal of Geophysical Research: Space Physics*, *114*(A11).

Sicard-Piet, A., S. Bourdarie, D. Boscher, and R. Friedel (2006), A Model for the Geostationary Electron Environment: POLE, From 30 keV to 5.2 MeV, *IEEE Transactions on Nuclear Science*, *53*(4), 1844–1850, doi:10.1109/tns.2006.877878.

Sicard-Piet, A., S. Bourdarie, D. Boscher, R. H. W. Friedel, M. Thomsen, T. Goka, H. Matsumoto, and H. Koshiishi (2008), A new international geostationary electron model: IGE-2006, from 1 keV to 5.2 MeV, *Space Weather*, *6*(7), n/a–n/a, doi:10.1029/2007sw000368.

Smirnov, A., M. Berrendorf, Y. Shprits, E. A. Kronberg, H. J. Allison, N. A. Aseev, I. S. Zhelavskaya, S. K. Morley, G. D. Reeves, M. R. Carver, et al. (2020), Medium energy electron flux in earth's outer radiation belt (merlin): A machine learning model, *Space Weather*, *18*(11), e2020SW002,532.

Spreiter, J. R., A. L. Summers, and A. Y. Alksne (1966), Hydromagnetic flow around the magnetosphere, *Planetary and Space Science*, *14*(3), 223–253.

Staples, F. A., A. Kellerman, K. R. Murphy, I. J. Rae, J. K. Sandhu, and C. Forsyth (2022), Resolving magnetopause shadowing using multimission measurements of phase space density, *Journal of Geophysical Research: Space Physics*, *127*(2), e2021JA029,298.

Stix, T. H. (1992), *Waves in plasmas*, Springer Science & Business Media.

Su, Z., F. Xiao, H. Zheng, Z. He, H. Zhu, M. Zhang, C. Shen, Y. Wang, S. Wang, C. Kletzing, et al. (2014), Nonstorm time dynamics of electron radiation belts observed by the van allen probes, *Geophysical Research Letters*, *41*(2), 229–235.

Summers, D., R. M. Thorne, and F. Xiao (1998), Relativistic theory of wave-particle resonant diffusion with application to electron acceleration in the magnetosphere, *Journal of Geophysical Research: Space Physics*, *103*(A9), 20,487–20,500.

Sundararajan, M., A. Taly, and Q. Yan (2017), Axiomatic attribution for deep networks, in *International conference on machine learning*, pp. 3319–3328, PMLR.

Tao, X., J. Bortnik, R. Thorne, J. Albert, and W. Li (2012), Effects of amplitude modulation on nonlinear interactions between electrons and chorus waves, *Geophysical Research Letters*, *39*(6).

Teng, S., X. Tao, W. Li, Y. Qi, X. Gao, L. Dai, Q. Lu, and S. Wang (2018), A statistical study of the spatial distribution and source-region size of chorus waves using van allen probes data, in *Annales Geophysicae*, vol. 36, pp. 867–878, Copernicus Publications Göttingen, Germany.

Thorne, R., W. Li, B. Ni, Q. Ma, J. Bortnik, L. Chen, D. Baker, H. E. Spence, G. Reeves, M. Henderson, et al. (2013), Rapid local acceleration of relativistic radiation-belt electrons by magnetospheric chorus, *Nature*, *504*(7480), 411–414.

Thorne, R. M. (2010), Radiation belt dynamics: The importance of wave-particle interactions, *Geophysical Research Letters*, *37*(22).

Thorne, R. M., J. Bortnik, W. Li, and Q. Ma (2021), Wave–particle interactions in the earth's magnetosphere, *Magnetospheres in the solar system*, pp. 93–108.

Tsurutani, B. T., W. D. Gonzalez, A. L. Gonzalez, F. L. Guarnieri, N. Gopalswamy, M. Grande, Y. Kamide, Y. Kasahara, G. Lu, I. Mann, et al. (2006), Corotating solar

wind streams and recurrent geomagnetic activity: A review, *Journal of Geophysical Research: Space Physics*, *111*(A7).

Tu, W., G. Cunningham, Y. Chen, M. Henderson, E. Camporeale, and G. Reeves (2013), Modeling radiation belt electron dynamics during gem challenge intervals with the dream3d diffusion model, *Journal of Geophysical Research: Space Physics*, *118*(10), 6197–6211.

Tu, W., W. Li, J. Albert, and S. Morley (2019), Quantitative assessment of radiation belt modeling, *Journal of Geophysical Research: Space Physics*, *124*(2), 898–904.

Turner, D., V. Angelopoulos, W. Li, M. Hartinger, M. Usanova, I. Mann, J. Bortnik, and Y. Shprits (2013), On the storm-time evolution of relativistic electron phase space density in earth's outer radiation belt, *Journal of Geophysical Research: Space Physics*, *118*(5), 2196–2212.

Ukhorskiy, A., B. Anderson, P. Brandt, and N. Tsyganenko (2006), Storm time evolution of the outer radiation belt: Transport and losses, *Journal of Geophysical Research: Space Physics*, *111*(A11).

Ukhorskiy, A., M. Sitnov, K. Takahashi, and B. Anderson (2009), Radial transport of radiation belt electrons due to stormtime pc5 waves, in *Annales Geophysicae*, vol. 27, pp. 2173–2181, Copernicus Publications Göttingen, Germany.

Van Allen, J. A. (1997), *Energetic Particles in the Earth's External Magnetic Field*, pp. 235–251, American Geophysical Union (AGU), doi:https://doi.org/10.1029/HG007p0235.

Van Allen, J. A., G. H. Ludwig, E. C. Ray, and C. E. McIlwain (1958), Observation of high intensity radiation by satellites 1958 alpha and gamma, *Journal of Jet Propulsion*, *28*(9), 588–592.

Vaswani, A., N. Shazeer, N. Parmar, J. Uszkoreit, L. Jones, A. N. Gomez, Ł. Kaiser, and I. Polosukhin (2017), Attention is all you need, *Advances in neural information processing systems*, *30*.

Walker, A. D. M. (2013), *Plasma waves in the magnetosphere*, vol. 24, Springer Science & Business Media.

Walsh, B. M., T. Bhakyapaibul, and Y. Zou (2019), Quantifying the uncertainty of using solar wind measurements for geospace inputs, *Journal of Geophysical Research: Space Physics*, *124*(5), 3291–3302, doi:https://doi.org/10.1029/2019JA026507.

Wing, S., J. R. Johnson, E. Camporeale, and G. D. Reeves (2016), Information theoretical approach to discovering solar wind drivers of the outer radiation belt, *Journal of Geophysical Research: Space Physics*, *121*(10), 9378–9399, doi:https://doi.org/10.1002/2016JA022711.

Wing, S., J. R. Johnson, D. L. Turner, A. Y. Ukhorskiy, and A. J. Boyd (2022), Untangling the solar wind and magnetospheric drivers of the radiation belt electrons, *Journal of Geophysical Research: Space Physics*, *127*(4), e2021JA030,246, doi:https://doi.org/10.1029/2021JA030246, e2021JA030246 2021JA030246.

Wrenn, G. L., D. J. Rodgers, and P. Buehler (2000), Modeling the outer belt enhancements of penetrating electrons, *Journal of Spacecraft and Rockets*, *37*(3), 408–415, doi:10.2514/2.3575.

Xiang, Z., W. Tu, B. Ni, M. Henderson, and X. Cao (2018), A statistical survey of radiation belt dropouts observed by van allen probes, *Geophysical Research Letters*, *45*(16), 8035–8043.

Zhang, A., Z. C. Lipton, M. Li, and A. J. Smola (2023), *Dive into deep learning*, Cambridge University Press.

Zhang, H., S. Fu, L. Xie, D. Zhao, C. Yue, Z. Pu, Y. Xiong, T. Wu, S. Zhao, Y. Sun, B. Cui, and Z. Luo (2020), Relativistic Electron Flux Prediction at Geosynchronous Orbit Based on the Neural Network and the Quantile Regression Method, *Space Weather*, *18*(9), doi:10.1029/2020sw002445.

Zhang, X.-J., A. Artemyev, V. Angelopoulos, E. Tsai, C. Wilkins, S. Kasahara, D. Mourenas, S. Yokota, K. Keika, T. Hori, et al. (2022), Superfast precipitation of energetic electrons in the radiation belts of the earth, *Nature communications*, *13*(1), 1611.

Zhao, H., D. N. Baker, S. Califf, X. Li, A. N. Jaynes, T. Leonard, S. G. Kanekal, J. B. Blake, J. F. Fennell, S. G. Claudepierre, D. L. Turner, G. D. Reeves, and H. E. Spence (2017a), Van Allen Probes Measurements of Energetic Particle Deep Penetration Into the Low L Region (L ¡ 4) During the Storm on 8 April 2016, *Journal of Geophysical Research: Space Physics*, *122*(12), 12,140–12,152, doi:10.1002/2017ja024558.

Zhao, H., D. Baker, A. Jaynes, X. Li, S. Elkington, S. Kanekal, H. Spence, A. Boyd, C.-L. Huang, and C. Forsyth (2017b), On the relation between radiation belt electrons and solar wind parameters/geomagnetic indices: Dependence on the first adiabatic invariant and l, *Journal of Geophysical Research: Space Physics*, *122*(2), 1624–1642.

Zhao, H., D. Baker, X. Li, A. Jaynes, and S. Kanekal (2019a), The effects of geomagnetic storms and solar wind conditions on the ultrarelativistic electron flux enhancements, *Journal of Geophysical Research: Space Physics*, *124*(3), 1948–1965.

Zhao, H., D. Baker, X. Li, D. Malaspina, A. Jaynes, and S. Kanekal (2019b), On the acceleration mechanism of ultrarelativistic electrons in the center of the outer radiation belt: A statistical study, *Journal of Geophysical Research: Space Physics*, *124*(11), 8590–8599.